



A Very High Energy γ -Ray Survey toward the Cygnus Region of the Galaxy

A. U. Abeysekara¹, A. Archer², T. Aune^{3,4}, W. Benbow⁵, R. Bird³, R. Brose^{6,7}, M. Buchovecky³, V. Bugaev², W. Cui^{8,9}, M. K. Daniel⁵, A. Falcone¹⁰, Q. Feng¹¹, J. P. Finley⁸, H. Fleischhack⁷, A. Flinders¹, L. Fortson¹², A. Furniss¹³, E. V. Gotthelf¹⁴, J. Grube¹⁵, D. Hanna¹¹, O. Hervet¹⁶, J. Holder¹⁷, K. Huang^{3,18}, G. Hughes⁵, T. B. Humensky¹⁹, M. Hütten⁷, C. A. Johnson¹⁶, P. Kaaret²⁰, P. Kar¹, N. Kelley-Hoskins⁷, M. Kertzman²¹, D. Kieda¹, M. Krause⁷, S. Kumar¹⁷, M. J. Lang²², T. T. Y. Lin¹¹, G. Maier⁷, S. McArthur⁸, P. Moriarty²², R. Mukherjee²³, S. O'Brien²⁴, R. A. Ong³, A. N. Otte²⁵, D. Pandel²⁶, N. Park²⁷, A. Petrashyk¹⁹, M. Pohl^{6,7}, A. Popkow^{3,28}, E. Pueschel⁷, J. Quinn²⁴, K. Ragan¹¹, P. T. Reynolds²⁹, G. T. Richards²⁵, E. Roache⁵, J. Rousselle³, C. Rulten¹², I. Sadeh⁷, M. Santander²³, G. H. Sembroski⁸, K. Shahinyan¹², J. Tyler¹¹, V. V. Vassiliev³, S. P. Wakely²⁷, J. E. Ward³⁰, A. Weinstein³¹, R. M. Wells³¹, P. Wilcox²⁰, A. Wilhelm^{6,7}, D. A. Williams¹⁶, and B. Zitzer¹¹

¹ Department of Physics and Astronomy, University of Utah, Salt Lake City, UT 84112, USA

² Department of Physics, Washington University, St. Louis, MO 63130, USA

³ Department of Physics and Astronomy, University of California, Los Angeles, CA 90095, USA; ralphbird@astro.ucla.edu, apopkow@ucla.edu

⁴ The Climate Corporation, San Francisco, CA 94103, USA

⁵ Fred Lawrence Whipple Observatory, Harvard-Smithsonian Center for Astrophysics, Amado, AZ 85645, USA

⁶ Institute of Physics and Astronomy, University of Potsdam, D-14476 Potsdam-Golm, Germany

⁷ DESY, Platanenallee 6, D-15738 Zeuthen, Germany; maria.krause@desy.de

⁸ Department of Physics and Astronomy, Purdue University, West Lafayette, IN 47907, USA

⁹ Department of Physics and Center for Astrophysics, Tsinghua University, Beijing 100084, People's Republic of China

¹⁰ Department of Astronomy and Astrophysics, 525 Davey Lab, Pennsylvania State University, University Park, PA 16802, USA

¹¹ Physics Department, McGill University, Montreal, QC H3A 2T8, Canada

¹² School of Physics and Astronomy, University of Minnesota, Minneapolis, MN 55455, USA

¹³ Department of Physics, California State University—East Bay, Hayward, CA 94542, USA

¹⁴ Columbia Astrophysics Laboratory, Columbia University, New York, NY 10027, USA

¹⁵ Department of Physics, Stevens Institute of Technology, Hoboken, NJ 07030, USA

¹⁶ Santa Cruz Institute for Particle Physics and Department of Physics, University of California, Santa Cruz, CA 95064, USA

¹⁷ Department of Physics and Astronomy and the Bartol Research Institute, University of Delaware, Newark, DE 19716, USA

¹⁸ Van Nuys High School, Van Nuys, CA 91411, USA

¹⁹ Physics Department, Columbia University, New York, NY 10027, USA

²⁰ Department of Physics and Astronomy, University of Iowa, Van Allen Hall, Iowa City, IA 52242, USA

²¹ Department of Physics and Astronomy, DePauw University, Greencastle, IN 46135-0037, USA

²² School of Physics, National University of Ireland Galway, University Road, Galway, Ireland

²³ Department of Physics and Astronomy, Barnard College, Columbia University, NY 10027, USA

²⁴ School of Physics, University College Dublin, Belfield, Dublin 4, Ireland

²⁵ School of Physics and Center for Relativistic Astrophysics, Georgia Institute of Technology, 837 State Street NW, Atlanta, GA 30332-0430, USA

²⁶ Department of Physics, Grand Valley State University, Allendale, MI 49401, USA

²⁷ Enrico Fermi Institute, University of Chicago, Chicago, IL 60637, USA

²⁸ Department of Physics and Astronomy, University of Hawaii at Manoa, Honolulu, HI 96822, USA

²⁹ Department of Physical Sciences, Cork Institute of Technology, Bishopstown, Cork, Ireland

³⁰ Institut de Física d'Altes Energies (IFAE), The Barcelona Institute of Science and Technology, Campus UAB, E-08193 Bellaterra (Barcelona), Spain

³¹ Department of Physics and Astronomy, Iowa State University, Ames, IA 50011, USA

Received 2017 September 21; revised 2018 May 7; accepted 2018 May 11; published 2018 July 12

Abstract

We present results from deep observations toward the Cygnus region using 300 hr of very high energy (VHE) γ -ray data taken with the VERITAS Cerenkov telescope array and over 7 yr of high-energy γ -ray data taken with the *Fermi* satellite at an energy above 1 GeV. As the brightest region of diffuse γ -ray emission in the northern sky, the Cygnus region provides a promising area to probe the origins of cosmic rays. We report the identification of a potential *Fermi*-LAT counterpart to VER J2031+415 (TeV J2032+4130) and resolve the extended VHE source VER J2019+368 into two source candidates (VER J2018+367* and VER J2020+368*) and characterize their energy spectra. The *Fermi*-LAT morphology of 3FGL J2021.0+4031e (the Gamma Cygni supernova remnant) was examined, and a region of enhanced emission coincident with VER J2019+407 was identified and jointly fit with the VERITAS data. By modeling 3FGL J2015.6+3709 as two sources, one located at the location of the pulsar wind nebula CTB 87 and one at the quasar QSO J2015+371, a continuous spectrum from 1 GeV to 10 TeV was extracted for VER J2016+371 (CTB 87). An additional 71 locations coincident with *Fermi*-LAT sources and other potential objects of interest were tested for VHE γ -ray emission, with no emission detected and upper limits on the differential flux placed at an average of 2.3% of the Crab Nebula flux. We interpret these observations in a multiwavelength context and present the most detailed γ -ray view of the region to date.

Key words: acceleration of particles – cosmic rays – gamma rays: general – ISM: supernova remnants

Supporting material: figure set

1. Introduction

Very high energy (VHE; $E > 100 \text{ GeV}$ [10^{11} eV]) γ -rays provide insights into the most extreme environments in our local universe. Produced by the interactions of relativistic particles, this radiation enables the study of the nonthermal astrophysical processes by which these particles are accelerated.

The Cygnus region is the brightest region of diffuse high-energy (HE; 0.1 GeV [10^8 eV] $< E < 100 \text{ GeV}$ [10^{11} eV]) γ -rays in the northern sky. Seen as a small-scale version of a whole galaxy, the Cygnus region harbors a wealth of objects, including over 10 supernova remnants (SNRs; Green 2014), more than 14 pulsars (Manchester et al. 2005), and nine OB associations, as well as numerous pulsar wind nebulae (PWNe), H II regions, Wolf-Rayet binary systems, microquasars, dense molecular clouds, and a superbubble. Cygnus X, a large, diffuse region (roughly $5^\circ \times 5^\circ$ centered at $20^{\text{h}}31^{\text{m}}$, $40^\circ20'$) of bright radio emission, is one of the richest known regions of star formation in the Galaxy, with OB associations that have a total stellar mass as high as $10^6 M_\odot$ (Reipurth & Schneider 2008) and a total mechanical stellar wind energy output of $\geq 10^{39} \text{ erg s}^{-1}$ (Lozinskaya et al. 2002), corresponding to several percent of the energy output by SNRs in the entire Galaxy (Verschuur & Kellermann 1988). This makes the Cygnus region the largest known star-forming region in the Galaxy outside the Galactic center, and this, combined with its proximity, is thought to be the reason for its brightness in HE γ -rays.

The Cygnus region has already been observed by various instruments at different wavelengths, including radio observations by the Canadian Galactic Plane Survey (CGPS; Taylor et al. 2003) and the Giant Metrewave Radio Telescope (Paredes et al. 2007), infrared observations by the *Spitzer Space Telescope* (Benjamin et al. 2003; Rieke et al. 2004; Churchwell et al. 2009), and X-ray observations by *Chandra* (Butt et al. 2003, 2006), *XMM-Newton* (Horns et al. 2007), and *Suzaku* (Murakami et al. 2011; Mizuno et al. 2017). These observations have highlighted the variety of objects and processes within the region and firmly established it as a key region for understanding our Galaxy.

In the HE wave band, 36 γ -ray sources have been detected by the *Fermi*-LAT in the region covered by this analysis (described in Section 2) and published in the *Fermi* Large Area Telescope Third Source Catalog (3FGL; Acero et al. 2015), of which seven are pulsars and one is the large star-forming region, the Cygnus Cocoon. Of these sources, 12 appear in the Third Catalog of Hard *Fermi*-LAT Sources (3FHL; Ajello et al. 2017), a catalog of sources above 10 GeV, of which five are pulsars, and three in the Second *Fermi*-LAT Catalog of High-Energy Sources (2FHL; Ackermann et al. 2016), a catalog above 50 GeV.

The Cygnus region has been observed by several VHE γ -ray instruments, including HEGRA (Aharonian et al. 2005), Milagro (Abdo et al. 2007), ARGO-YBJ (Bartoli et al. 2012), MAGIC (Albert et al. 2007; Aleksić et al. 2010), VERITAS (Aliu et al. 2013, 2014a, 2014b; Archambault et al. 2013), and HAWC (Abeysekara et al. 2017). In the region defined in Section 2, seven VHE sources have already been detected. TeV J2032+4130 is an unidentified VHE emitter that lies within the extended Cygnus Cocoon. VER J2019+407 is also located within the Cygnus Cocoon and is associated with the Gamma Cygni SNR (G78.2+2.1). The large, bright, unidentified Milagro source MGRO

J2019+37 has since been resolved into two sources after observations by VERITAS: VER J2016+371 is associated with the SNR CTB 87, and VER J2019+368 is a spatially extended source whose origin has yet to be identified. HAWC has recently published the 2HWC catalog (Abeysekara et al. 2017), their first catalog with the completed detector. The catalog was produced using 507 days of data and identified three new sources in the survey region: 2HWC J1953+294, which lies at the edge of the survey region, 2HWC J2006+341, and 2HWC J2024+417* (the * signifies that the source is separated from neighboring sources by a $\Delta(\sqrt{\text{Test Statistic}})$ of between 1 and 2).

In this paper we present a survey over a 15° by 5° portion of the Cygnus region centered on Galactic longitude (l) 74.5° and Galactic latitude (b) 1.5° conducted by VERITAS between 2007 April and 2008 December with a total observing time of 135 hr (120 hr live time). We also include targeted and follow-up observations of 174 hr (151 hr live time) made by VERITAS between 2008 November and 2012 June, for a total observing time of 309 hr (271 hr live time) distributed as shown in Figure 1. Initial results from these observations, including the deeper study of three regions, have already been published by the VERITAS Collaboration (Aliu et al. 2013, 2014a, 2014b). Here we report the results from the combined sample of survey and follow-up observations from VERITAS.

After a description of VERITAS, its data set and analysis methods are presented in Section 2. This is followed by a description of the *Fermi*-LAT and its data analysis in Section 3. Descriptions of the VERITAS results for the whole region are given in Section 4, and the *Fermi*-LAT results are given in Section 5. This is followed by the detailed study of the individual VHE sources previously detected by VERITAS in Section 6.

2. VERITAS Observations and Data Analysis

The Very Energetic Radiation Imaging Telescope Array System (VERITAS) is an array of four imaging atmospheric Cerenkov telescopes (IACTs), located at the Fred Lawrence Whipple Observatory in southern Arizona ($31^\circ40' \text{ N}$, $110^\circ57' \text{ W}$, 1.3 km a.s.l.). Each telescope is of Davies-Cotton design, with a 12 m diameter reflector composed of 350 hexagonal mirror facets (Holder et al. 2006). The focal length of each telescope is 12 m, and each telescope is equipped with a camera consisting of 499 photomultiplier tube (PMT) “pixels” at the focus. The angular spacing between PMTs is 0.15° , which yields a total field of view (FOV) of 3.5° . Full array operations began in 2007, and in the summer of 2009 the first telescope was relocated to increase the sensitivity of the array (Otte 2009). The trigger was upgraded in the winter of 2012. In summer 2012 the cameras in each telescope were replaced with new, high quantum efficiency PMTs, which has resulted in a decrease of the array energy threshold to about 85 GeV (Park 2015). All the data presented in this work were taken prior to the 2012 camera upgrade using standard VERITAS operational procedures.

From 2007 April through 2008 December, VERITAS undertook a survey of a 15° by 5° area of the Cygnus region, covering Galactic longitude (l) from 67° to 82° and Galactic latitude (b) from -1° to 4° . With a 1.75° radius FOV, the VERITAS exposure extends out to cover approximately a 19° by 9° area ($65.5^\circ < l < 83.5^\circ$, $-2.5^\circ < b < 5.5^\circ$). The survey

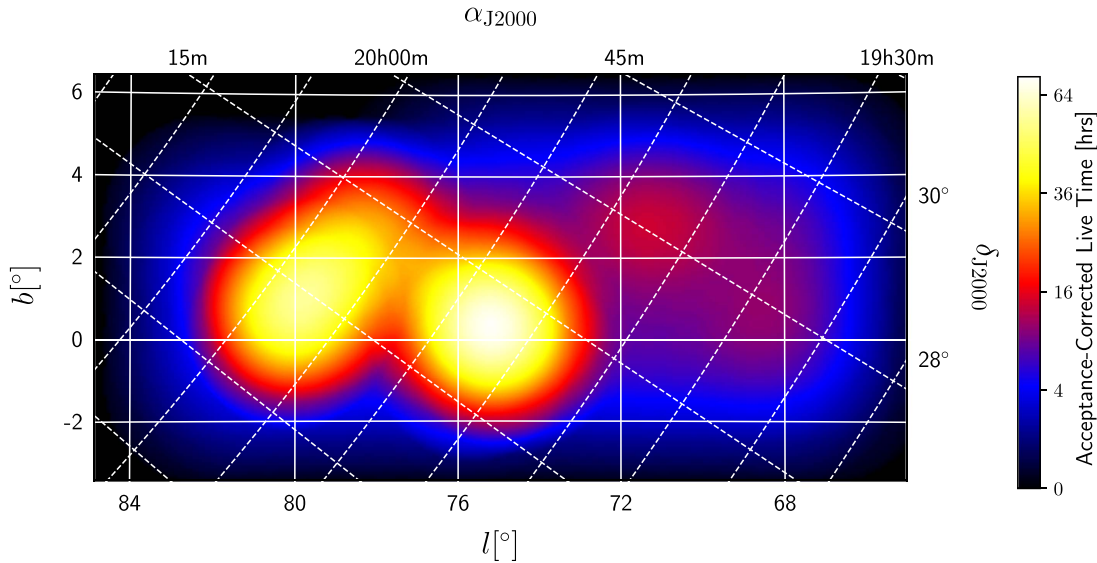


Figure 1. VERITAS exposure map of the observations used in this analysis, in Galactic (longitude, l , and latitude, b) and equatorial (right ascension, α_{J2000} , and declination, δ_{J2000}) coordinates (solid and dashed lines, respectively). The color scale represents the acceptance-corrected live time in hours. The bright regions correspond to the primary targets within the region, MGRO J2019+37, TeV J2032+4130, and the Gamma Cygni SNR.

consisted of nearly 135 hr (120 hr live time) of observations, reaching an average point-source sensitivity of better than 4% of the Crab Nebula flux above 200 GeV. Runs were taken at pointed positions with a spacing of 0.8° in the longitudinal direction and 1° in the latitudinal direction. An exposure time of approximately 1 hr per grid point was taken, with that hour broken into three 20-minute observation runs, giving the survey region a relatively uniform exposure of about 6 hr. Observations were scheduled to keep the average zenith angle close to 20° to avoid the higher energy threshold associated with larger zenith angle observations.

In addition to this survey, additional observations totaling 174 hr (151 hr live time) were conducted in this region, targeting objects of interest and following up on hot spots identified in the initial survey. These observations were typically conducted in wobble mode (Fomin et al. 1991), where the center of the FOV is offset from the target in one of the cardinal directions, allowing for simultaneous background estimation.

After removing periods affected by bad weather or hardware issues, 309 hr of data were taken. Accounting for dead time results in a data set totaling 271 hr of quality-selected live time at an average zenith angle of 20° . The acceptance-corrected exposure is depicted in Figure 1.

The results presented here were generated using one of the standard VERITAS event reconstruction packages as described in Daniel (2007). The air shower images are parameterized using the Hillas moment analysis (Hillas 1985) following calibration and image cleaning. Four analyses were conducted with four sets of selection criteria (“cuts”) used to identify good-quality images, and to discriminate between γ -rays and the cosmic-ray background, these cuts consist of two different image intensity cuts and two different integration region sizes. The two different image intensity cuts that were applied as part of the selection of good-quality images were at a medium threshold (about 70 photoelectrons) and at a high threshold (about 130 photoelectrons), giving minimum energy thresholds for these observations of around 200 and 400 GeV, respectively. The minimum energy threshold depends on the

observing setup used for that point in the sky (energy threshold is defined here as the peak in the differential counting rate, the effective area multiplied by a power-law spectrum of -2). For both image intensity cuts, a reconstructed image was required in a minimum of three telescopes, and a constant image intensity cut was used across the survey region. After selecting good-quality images, selection cuts were applied on the reconstructed images to select γ -ray-like events before two source searches were conducted for each of the image intensity cuts. For a point-source search, we used an integration radius of $\theta_{\text{int}} = 0.1^\circ$ (*Point*), and for an extended source search $\theta_{\text{int}} = 0.23^\circ$ (*Extended*). In addition to selecting these cuts for optimum sensitivity to typical Galactic sources, they were chosen to reduce the impact of the numerous background stars in the region. With the higher energy threshold cuts applied, the point-spread function (PSF; 68% containment radius) at 1 TeV was 0.1° .

To produce a sky map of the region, the survey region was divided into a grid of trial source positions with grid points spaced by 0.025° , a value well below the PSF of the instrument. For each of these points, for both the *Point* and *Extended* integration radii, a ring background model (RBM) analysis (Berge et al. 2007) was conducted, and the significance of the deviation from a background-only model was calculated using Equation (17) of Li & Ma (1983). Spectral analysis was conducted using the reflected region (RR) method (Berge et al. 2007). In both cases regions around known sources and optically bright stars (magnitude brighter than 6) that cause a reduction in the local rate of events (Berge et al. 2007) are excluded from the background regions.

The source extension was determined by fitting a sky map of the excess events with a 2D Gaussian distribution convolved with the VERITAS PSF. The PSF was modeled as a King function and fit to observations of the Crab Nebula, with a correction applied for the difference between the spectral indices of the examined source and the Crab Nebula. To estimate the systematic uncertainty, the source extension was also determined using different models of the PSF. In addition, the models generated using the Crab Nebula models were also

generated using Mrk 421 observations, and the PSF was also modeled as the sum of two symmetric Gaussian functions, giving four different models of the PSF. The standard deviation of these four results is quoted as the systematic error.

For all sources except for VER J2016+371, to conduct a spectral analysis, only data taken with four telescopes in operation and with a pointing offset of less than one degree were used, to reduce systematic errors on the energy reconstruction. In the case of VER J2016+371, due to the larger pointing offset of the majority of the data, the offset requirement was relaxed to observations within two degrees. Due to the nature of the IACT technique, though the FOV is only 1.75° radius, large images can be reconstructed with origins that lie outside of the FOV. This allows for the offset requirement to be larger than the FOV. We found, through observations of the Crab Nebula and through simulations, that increasing the maximum offset up to two degrees increased the energy resolution and introduced a small ($<10\%$) bias in reconstructed energies. To account for these effects, we have increased the systematic error on VER J2016+371 to ± 0.4 on the spectral index and $\pm 40\%$ in the flux normalization from the estimate of the error of ± 0.2 on the spectral index and $\pm 20\%$ for the rest of these observations. All spectral points with a significance of at least 1σ were fit with one of two spectral types, a power law (PL, Equation (1)) or a log parabola (LP, Equation (2)), also known as a curved power law, with an F -test conducted to determine whether there was significant evidence of curvature:

$$F = \frac{dN}{dE} = N_0 \left(\frac{E}{E_0} \right)^{-\gamma} \quad (1)$$

$$F = \frac{dN}{dE} = N_0 \left(\frac{E}{E_b} \right)^{-\gamma - \beta \ln(E/E_b)}. \quad (2)$$

Here F is the differential flux, $-\gamma$ is the spectral index, β is the curvature of the spectral index, N_0 is the normalization, E_0 is the energy normalization, and E_b is the energy of the spectral break. For fits to curved spectra we insist on concavity, that is, for the LP $\beta > 0$. Upper limits were calculated using the method of Rolke (Rolke et al. 2005) at the 95% level (statistical uncertainty only) and with an assumed spectral index of -2.5 .

3. Fermi-LAT Analysis

The *Fermi Gamma-ray Space Telescope* has been operating since its launch in 2008 with two γ -ray instruments: the Large Area Telescope (LAT) and the Gamma-ray Burst Monitor (GBM). The LAT (Atwood et al. 2009), *Fermi*'s primary instrument, is a pair conversion γ -ray detector that is sensitive to γ -rays with energies from 20 MeV to greater than 500 GeV. The effective collecting area is approximately 6500 cm^2 at 1 GeV, and the angular resolution is strongly energy dependent, with a 68% containment radius of about 0.8° at 1 GeV. Tables describing the energy resolution, effective area, and angular resolution are provided with the publicly available analysis tools.³²

We have undertaken an analysis of the Cygnus region with over 7 yr (2008 August–2016 January) of *Fermi*-LAT Pass 8 data (Atwood et al. 2013) using *Fermi*-LAT science tools v10r0p5³³ and the *fermipy* tools v0.13.5 (Wood et al. 2017). In

order to reduce the contribution of the Galactic diffuse emission and for improved angular resolution, “FRONT+BACK” events were selected in the energy range from 1 to 500 GeV. They were selected within a 30° radius region centered at $(l, b) = (74.5, 1.5)$. The region of interest was taken to be $65.5 < l < 83.5$, $-2.5 < b < 5.5$ to match the VERITAS data. “SOURCE” class photons were selected to maximize the effective area, while the corresponding IRF “P8R2_SOURCE_V6” was used with a maximum zenith angle of 90° and only using good time intervals. We used the binned analysis technique (Abdo et al. 2009), implemented in the *fermipy* routine *optimize* to conduct an iterative fit to all of the sources and optimize the model parameters. It was then possible to calculate the significance of the source detection, the flux of the source, and the spectrum for sources in the region of interest. The base model was derived from the third *Fermi*-LAT source catalog (3FGL; Acero et al. 2015) using the provided templates for extended sources.³⁴ It was confirmed that all sources from the earlier *Fermi*-LAT high-energy catalogs (1FHL, Ackermann et al. 2013; 2FHL, Ackermann et al. 2016) in the region are also 3FGL sources (the 3FHL was published after this analysis was conducted, and a comparison with the results is presented in Section 5). For this analysis the Galactic diffuse emission model “gll_iem_v06.fits” and isotropic diffuse model “iso_P8R2_SOURCE_V6_v06.txt” provided by the *Fermi*-LAT Collaboration were used.³⁵ After an initial fit, sources with a Test Statistic (TS) less than 16.0 were removed from the subsequent fits. The *fermipy* tool *find_sources* was used to identify new sources in the region of interest with a TS of at least 20, which were then added to the model. The region was then refit with sources below a minimum TS (which was incrementally increased to 25 over a number of fits) removed.

As observed by the *Fermi*-LAT, up to a few tens of GeV, by far the brightest sources in the region are the pulsars, but they all exhibit a spectral break at around a few GeV (Abdo et al. 2013), with an extrapolated flux that at 1000 GeV exceeds the VERITAS sensitivity by several orders of magnitude. The pulsed emission is therefore not expected to contribute at very high energies. In contrast, PWNe are very common VHE emitters (H.E.S.S. Collaboration et al. 2018b), and nebulae associated with these bright pulsars might be detectable by VERITAS. To search for potential PWN emission associated with the observed VERITAS sources, a technique was employed to remove (or at least significantly reduce) the pulsar emission. To do this, a “gated” analysis was conducted, where a time cut was applied to the pulsar phase to remove the ON-pulse contribution. We used *tempo2* with the *Fermi*-LAT plugin (Hobbs et al. 2006; Ray et al. 2011) to assign pulsar phases to the photons in the region for the pulsars using the timing models from Kerr et al. (2015) for two pulsars that lie close to detected VERITAS sources (3FGL J2021.1+3651 and 3FGL J2032.2+4126), and the resulting phaseograms were checked against the published results. The ON-pulse region was defined using these phaseograms to cover any ON-pulse and bridge emission, with the region defined conservatively to minimize the contamination of the pulsar flux into the OFF-pulse region. Then, using only data from the time periods covered by the pulsar ephemeris, we looked for steady

³² https://www.slac.stanford.edu/exp/glast/groups/canda/lat_Performance.htm

³³ <http://fermi.gsfc.nasa.gov/ssc/data/analysis/>

³⁴ http://fermi.gsfc.nasa.gov/ssc/data/access/lat/4yr_catalog/LAT_extended_sources_v15.tgz

³⁵ <http://fermi.gsfc.nasa.gov/ssc/data/access/lat/BackgroundModels.html>

emission from a putative PWN in the OFF-pulse intervals. In addition to this standard gated analysis, which suffers from reduced sensitivity due to the reduced exposure time after phase cuts and the limited time range of the publicly available ephemerides, we performed an additional analysis. The aim of this analysis was to increase the exposure available, increasing the sensitivity and reducing the statistical errors. This was performed by conducting an ON-pulse analysis on the data covered by the available ephemerides to determine the spectral parameters of the pulsar emission. The parameters of the pulsar in the full model were then fixed to these parameters, and the whole data set (covering the full time range) was refit. Nebula emission should then be apparent as a positive residual. For this method to work, the ON-pulse flux needs to be steady over time; thus, we checked the catalog light curves and also produced new light curves of each of these objects to check for flux variability. The analysis method was not applied to 3FGL J2021.5+4026 (the Gamma Cygni pulsar) owing to its large flux variability over time and the lack of a clearly definable OFF-pulse (Allafort et al. 2013). This did not unduly impact the analysis of the region since the Gamma Cygni SNR was already detected as an extended object in the *Fermi*-LAT data (Lande et al. 2012) and is clearly distinguishable from the pulsar emission. Any sources found in this way were added to the model, the pulsar spectral parameters freed, and a new fit was conducted. Provided that the new source has a TS of at least 25 after being refit with the pulsar parameters free, it was kept in the model.

The *Fermi*-LAT sources were fit with one of three spectral types: a power law (PL, Equation (1)), a log parabola (LP, Equation (2)), or (in the case of identified pulsars as in the 3FGL) a power law with exponential cutoff (PLEC, Equation (3)):

$$F = \frac{dN}{dE} = N_0 \left(\frac{E}{E_0} \right)^{-\gamma} \exp \left(\frac{-E}{E_c} \right), \quad (3)$$

where E_c is the energy of the spectral cutoff.

A number of sources that were fit with an LP in the 3FGL were fit with a PL in this analysis because β was either negative or consistent with zero within errors, which is likely due to the higher energy threshold in this analysis. The decorrelation energy of each source with a power-law spectrum was then calculated and the spectrum refit with the pivot energy set to the decorrelation energy. This produced the base model from which all analyses were conducted.

For *Fermi*-LAT sources associated with VERITAS sources, a χ^2 fit was conducted for the spectral points for both the VERITAS and *Fermi*-LAT data, considering statistical errors only. Three different spectral models were tested: PL (Equation (1)), LP (Equation (2)), and broken power law (BPL, Equation (4)):

$$F = \frac{dN}{dE} = \begin{cases} N_0 \left(\frac{E}{E_b} \right)^{-\gamma_1} & \text{if } E \leq E_b \\ N_0 \left(\frac{E}{E_b} \right)^{-\gamma_2} & \text{if } E > E_b. \end{cases} \quad (4)$$

As mentioned previously, for fits to curved spectra we insist on concavity, that is, for the LP $\beta > 0$ and for the BPL $-\gamma_1 > -\gamma_2$.

4. VERITAS Results

We used the ring background method (Section 2) over a grid of points at a spacing of $0^\circ.025$ and the higher-energy image intensity cut to produce a sky map of the significances for the observed region. This resulted in an average energy threshold of about 400 GeV, which is roughly uniform across the survey region. Examination of these significance sky maps (Figure 2) produced with both integration region radii show the four known VHE sources as regions of high significance (shown in detail in Figures 3–5). The extended sources VER J2031+415, VER J2019+407, and VER J2019+368 were detected at 10.1σ , 7.6σ , and 10.3σ , respectively, using the *Extended* integration region, and are described in more detail in Sections 6.1–6.3. The point source VER J2016+371 was detected at 6.2σ using the *Point* integration region and is described in Section 6.4. For this analysis, the statistical significance is quoted at the predefined locations of these sources without accounting for statistical trials. Full descriptions of the analyses leading to the detection of each of these objects, as well as the statistical trials involved, are given in the relevant discovery papers.

The presence of γ -ray sources in these sky maps can be determined by examining a histogram of all of the bins in the significance sky map. If the null hypothesis is true (that there is a uniform background and that the camera acceptance is well modeled), then the only variation in the significances of the bins should be statistical, and they should be normally distributed. In this case, we know that there are both γ -ray sources and bright stars that invalidate the null hypothesis; thus, we only expect the significances to be normally distributed in the bins that lie away from these regions. We have produced two histograms: one with all of the bins in the sky map included, which should show significant variation from a normal distribution owing to the stars and the γ -ray sources, and one with γ -ray sources and bright stars excluded, which should be normally distributed. Examining these histograms (Figure 6) shows the presence of the known sources prior to their exclusion (blue line), but no additional sources after the known sources have been excluded (orange line). The distribution with both the sources and bright stars excluded is close to a normal distribution (black line) with the mean approximately equal to zero and standard deviation approximately equal to one. The wider distribution for the *Extended* analysis reflects the greater correlation between the bins and is common in such analyses. With no clear positive excess there is no evidence for additional sources, and the good fit to a normal distribution shows that the background and acceptance functions are well modeled and understood.

To check for weak sources whose presence could be masked by the number of bins in the distribution, the survey region was broken up into smaller, overlapping $6^\circ \times 6^\circ$ tiles, and the significance distributions from those regions were also examined. Again, no evidence for any sources beyond the four previously detected sources was found, and the background was found to be well modeled for all of the regions.

4.1. Upper Limits of Undetected Sources

In addition to the four VHE sources previously detected, there are a number of other objects within the Cygnus region that are potential VHE γ -ray emitters. These are objects that show significant, nonthermal emission in other wave bands, or belong to source classes that are either known to be or thought

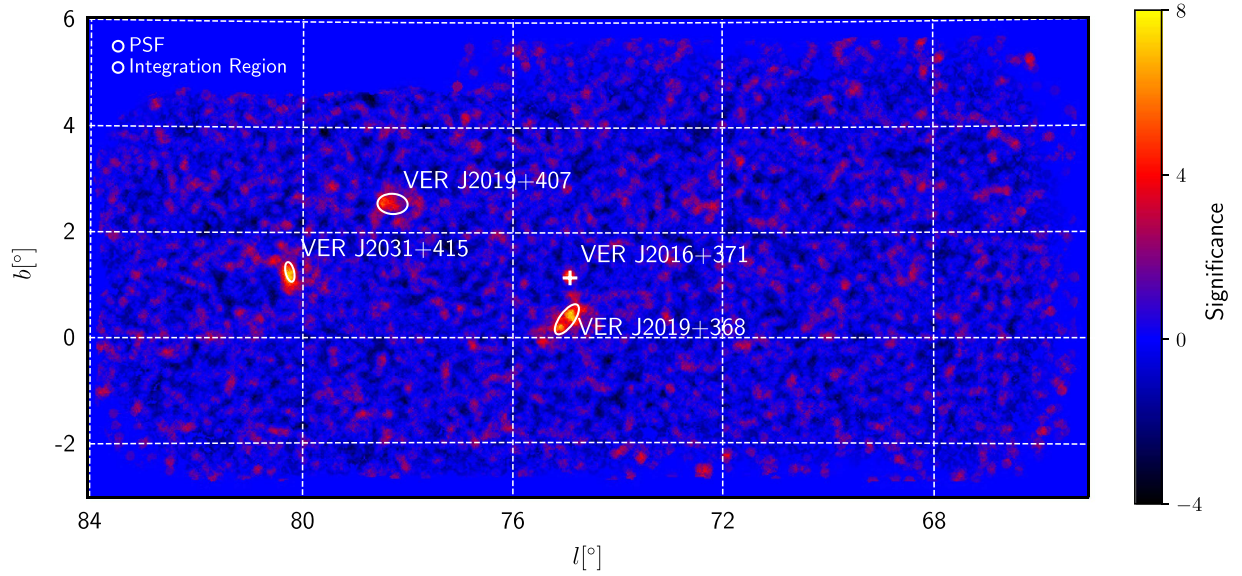
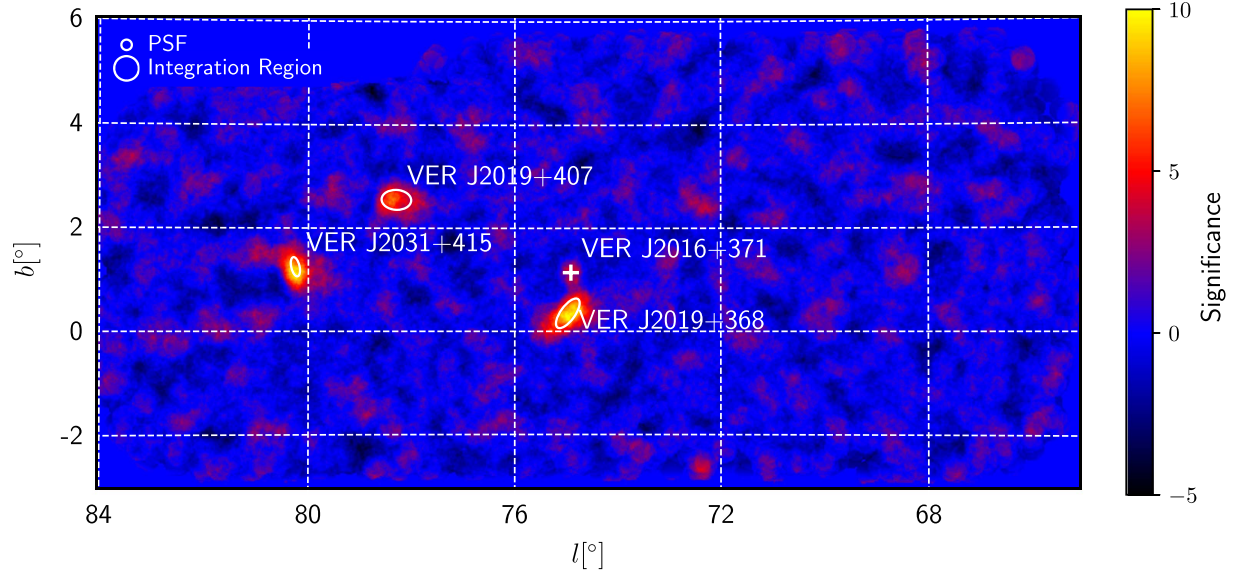
(a) *Point* integration region (radius = 0.1°)(b) *Extended* integration region (radius = 0.23°)

Figure 2. Significance sky maps above 400 GeV of the entire region using the *Point* (0.1°) and *Extended* (0.23°) integration radii. Significances were calculated using Equation (17) of Li & Ma (1983) and the ring background method. Areas around known sources and bright stars were excluded from background regions. Overlaid are the 1σ ellipses for the source extension fits with an asymmetric Gaussian function for the three extended sources (VER J2019+407, VER J2031+415, VER J2019+368) and the position for VER J2016+371 (plus sign).

to be VHE γ -ray emitters. Foremost among these objects are the two bright X-ray sources, Cygnus X-1 and X-3.

Cygnus X-1 is a high-mass X-ray binary (HMXB) that consists of a $14.8 \pm 1.0 M_\odot$ black hole orbiting around a O9.7Iab companion of $19.2 \pm 1.9 M_\odot$. The binary system is located at a distance of $1.86^{+0.12}_{-0.11}$ kpc (Reid et al. 2011; Xiang et al. 2011) in a circular orbit of 5.6 days and at an inclination of $27^\circ 1 \pm 0^\circ 8$.

There has been no detection of steady VHE emission from Cygnus X-1, although MAGIC observations showed evidence of variable emission at the 4.9σ level (4.1σ after accounting for the number of statistical trials) for emission during 79 minutes

effective on time between 2006 September 24 $22^{\text{h}}17$ and $23^{\text{h}}41$ UTC (Albert et al. 2007). Further observations by MAGIC are reported in Ahnen et al. (2017), where they set integral upper limits at 95% confidence level for energies above 200 GeV at 2.6×10^{-12} and 1.0×10^{-11} photons $\text{cm}^{-2} \text{s}^{-1}$ for the hard and soft states, respectively. VERITAS observations were presented in Guenette (2009), giving a 99% upper limit on the flux above 400 GeV of $1.05 \times 10^{-12} \text{cm}^{-2} \text{s}^{-1}$. Evidence for HE emission was first found by Malyshev et al. (2013) at the 4σ level using Pass 7 *Fermi*-LAT data. This was for emission in the hard spectral state when the lower-energy thermal component is weak and the emission is dominated by high-energy X-rays. Using Pass

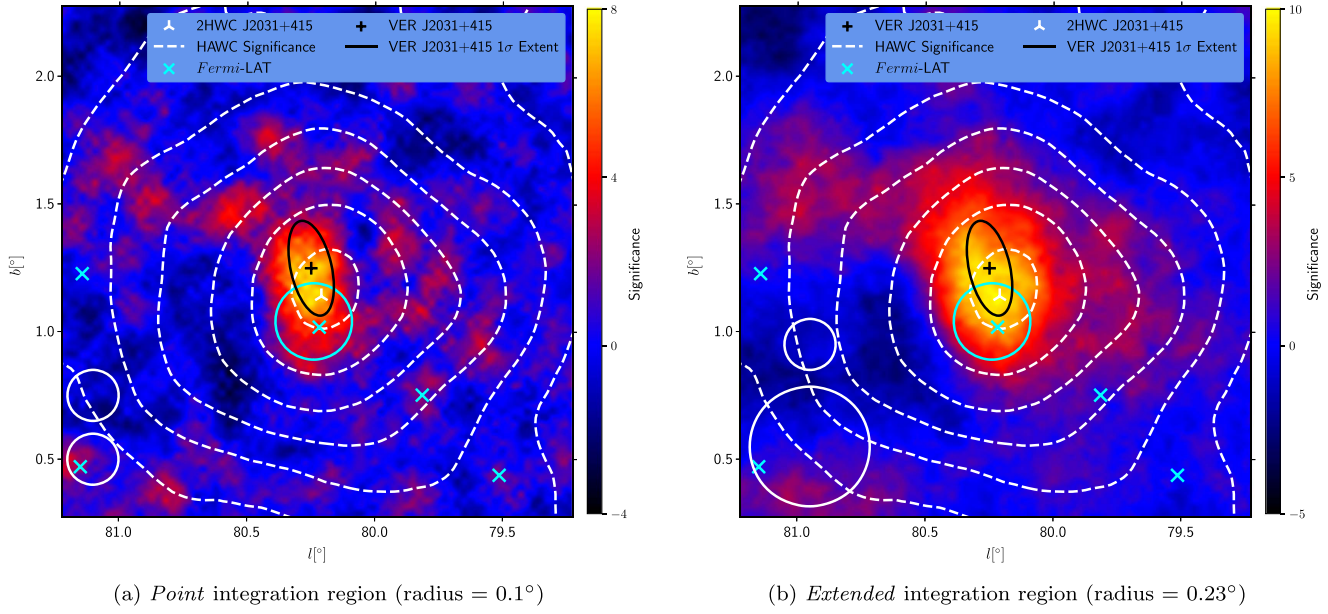


Figure 3. Significance maps of the region around VER J2031+415. Overlaid are the 1σ ellipses for the source extension and its centroid (black), along with the location of 2HWC J2031+415 (white three-pointed stars), the positions of the *Fermi*-LAT sources (cyan), and HAWC significance contours (at 2σ levels starting at 4σ ; white dashed). The upper white circle in the lower left is the PSF, while the lower circle is the integration region.

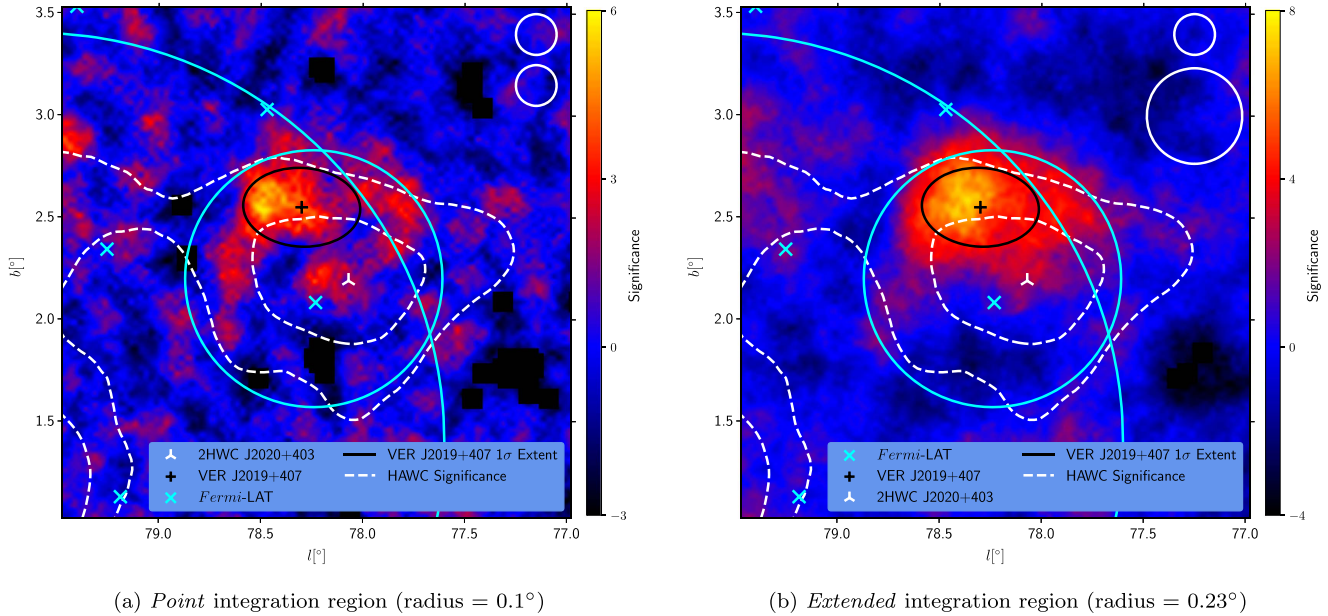


Figure 4. Significance maps of the region around VER J2019+407. Overlaid are the 1σ ellipses for the source extension and its centroid (black), along with the location of 2HWC J2019+407 (white three-pointed stars), the positions of the *Fermi*-LAT sources (cyan), and HAWC significance contours (at 2σ levels starting at 4σ ; white dashed). The smaller cyan circle shows the extent of 3FGL J2021.0+4031e (G78.2+2.1) and the arc of a larger cyan circle the extent of 3FGL J2028.6-4110e (the Cygnus Cocoon). The upper white circle in the upper right is the PSF, while the lower circle is the integration region.

8 data, Zanin et al. (2016) found emission correlated with the hard spectral state later on confirmed by Zdziarski et al. (2017).

Cygnus X-3 was the first microquasar seen emitting in HE γ -rays by AGILE (Tavani et al. 2009) and *Fermi*-LAT (Abdo et al. 2009) (although it does not appear in the 3FGL catalog owing to flux variability, it is associated with 1FGL J2032.4+4057 and 2FGL J2032.1+4049). Unlike Cygnus X-1, where HE emission is associated with the hard spectral state and the presence of jets, in Cygnus X-3 HE emission is strongly anticorrelated with the hard X-ray emission, is emitted prior to major radio flares, and

is associated with discrete-blob jets (Corbel et al. 2012; Piano et al. 2012). Cygnus X-3 is an HMXB where the compact object powering the system is either a neutron star in an unusual state of accretion or a black hole of $10\text{--}20 M_\odot$ orbiting around a Wolf-Rayet companion (van Kerkwijk et al. 1992). Study of this system could shed light on the nonthermal processes associated with the formation of relativistic jets from accretion processes. Currently, the source is undetected at very high energies, and flux upper limits have been set by VERITAS and MAGIC, with the former reporting a limit of 0.7×10^{-12} photons $\text{cm}^{-2} \text{s}^{-1}$ above

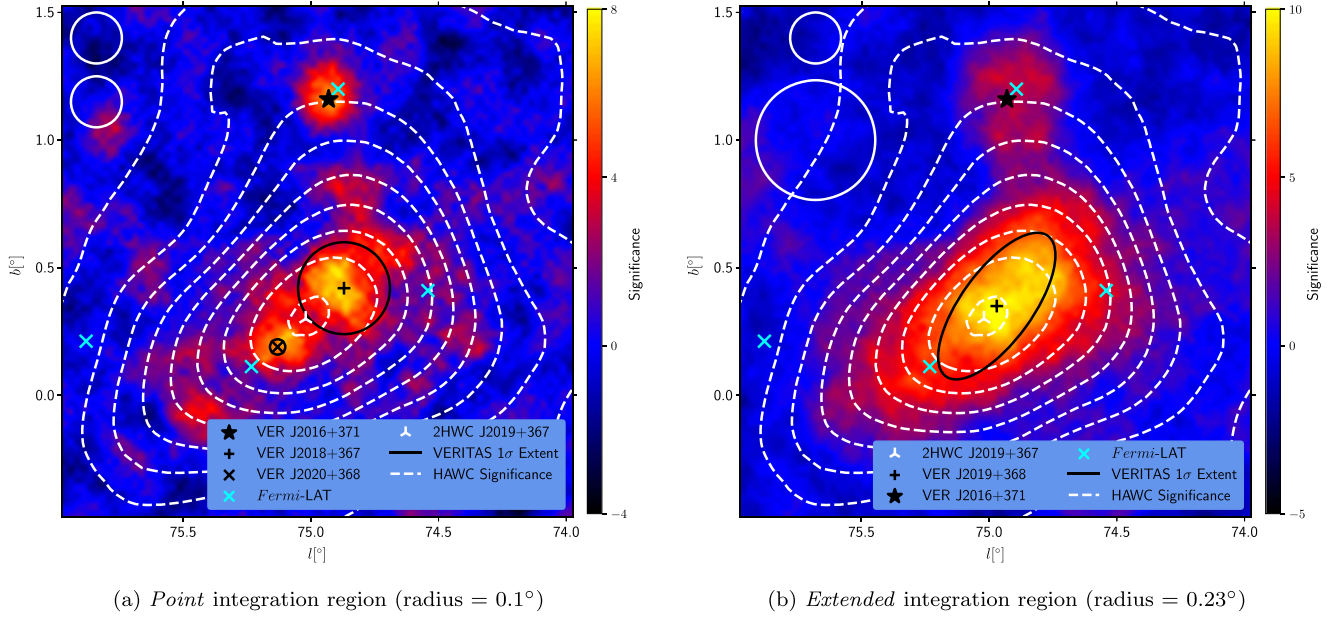


Figure 5. Significance maps of the region around VER J2018+367*, VER J2020+368*, and VER J2016+371. Overlaid are the 1σ ellipses for the source extension and their centroids (black), along with the location of 2HWC J2019+367 (white three-pointed stars), the positions of the *Fermi*-LAT sources (cyan), and HAWC significance contours (at 2σ levels starting at 4σ ; white dashed). The upper white circle in the upper left is the PSF, while the lower circle is the integration region.

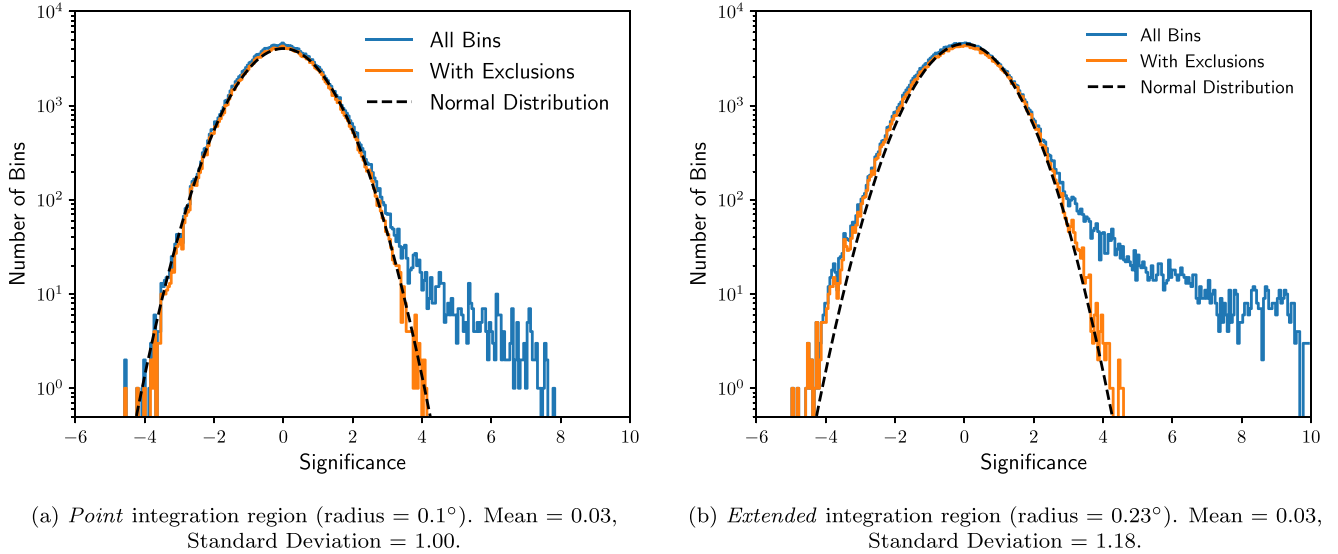


Figure 6. Histograms of the significances of the bins in VERITAS sky maps (Figure 2). Blue includes all the bins, orange includes all the bins that are not excluded owing to their proximity to a source or a bright star, and black is a normal distribution (with mean = 0 and standard deviation = 1.0). The mean and standard deviation indicated for each figure correspond to the orange histogram.

263 GeV (Archambault et al. 2013) and the latter reporting an upper limit of 2.2×10^{-12} photons $\text{cm}^{-2} \text{s}^{-1}$ above 250 GeV (Aleksić et al. 2010). VERITAS has also conducted observations during radio and γ -ray flaring episodes, placing a preliminary upper limit on the flux at $3.11 \times 10^{-12} \text{cm}^{-2} \text{s}^{-1}$ above 500 GeV. The results presented here for both Cygnus X-1 and X-3 are the average over all the observations, irrespective of the spectral state. Breakdowns by spectral state are beyond the scope of this work.

In addition to these two well-known HMXBs, there are other high- and low-mass X-ray binaries in the region, along with a number of other potential sources of VHE emission, including PWNe, SNRs, and colliding-wind binaries (CWBs).

In this paper we have generated a list of PWNe/SNRs using Green’s catalog (Green 2014) and cross-checked it with “a census of high-energy observations of Galactic supernova remnants”³⁶ (Ferrand & Safi-Harb 2012). We developed lists of binaries from the catalogs produced by Liu et al. (2006, 2007) and De Becker & Raucq (2013). The list of sources presented here is not intended to be exhaustive; rather, the sources have been selected by the authors of this paper as potential VHE emitters. All of the sources from the *Fermi*-LAT analysis in this work (Section 5) are also included. In addition,

³⁶ <http://www.physics.umanitoba.ca/snr/SNRcat>

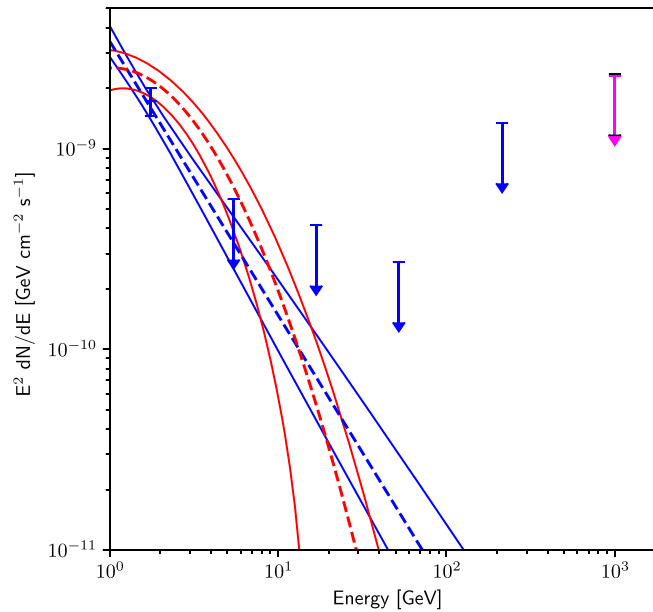


Figure 7. SED for 3FGL J1951.6+2926 (blue). For sources that lie outside of the VERITAS source exclusion regions, VERITAS 95% confidence level differential upper limits are presented for the point and extended analyses in black and magenta, respectively (see Section 4.1 for details). The red butterfly is the 3FGL catalog spectrum (Acero et al. 2015), and purple is from the 3FHL catalog (Ajello et al. 2017).

(The complete figure set (52 images) is available.)

two sources from the 3FHL (3FHL J1950.5+3457 and 3FHL J2026.7+3449) that are not associated with sources in the 3FGL are included (3FHL J2015.9+3712, which lies within the VER J2016+371 region, is discussed in Section 6.4), along with the three undetected HAWC sources. If two upper limit locations lie within $0^\circ 05$ (typically because the source is also detected by the *Fermi*-LAT), then the more accurate radio/X-ray position is taken as the nominal position.

In total, 71 locations were tested; the upper limits are presented in Table 1, and for all of the *Fermi*-LAT sources, they are also plotted on the relevant *Fermi*-LAT spectral energy distributions (SEDs) in Figure 7. In the majority of cases, the upper limits do not constrain an extrapolation of the *Fermi*-LAT flux, with the remaining sources having upper limits that lie within approximately 1σ of the extrapolated flux. The mean upper limit was 2.3% (2.9%) of the Crab Nebula flux³⁷ for the *Point* (*Extended*) integration regions above 600 GeV. The most significant location tested is G69.7+1.0, which has σ_{local} of 3 for the *Point* integration region and 2.3 for the *Extended* integration region. Since we have tested 71 locations for upper limits, a corresponding trials factor (calculated using Equation (12)) needs to be imposed; after applying this correction, we determined σ_{global} values of 1.3 and 0.6, respectively.

2HWC J1953+294 lies at the edge of the survey region, only covered by a few runs at a large offset in this analysis, with 109 minutes of live time. At its location, the RBM significance is 0.75σ (-0.12σ) for the *Point* (*Extended*) analysis. Holder & the VERITAS Collaboration (2016) presented an analysis of 37 hr of VERITAS data that cover this source (most of which is not included in this paper) and found a statistically significant γ -ray source located within the HAWC source contours. This

emission is coincident with the PWN DA 495 (G65.7+1.2) and its central object, WGA J1952.2+2925. Further work on this region will form part of a forthcoming publication.

2HWC J2006+341 was not detected in this analysis with the RBM analysis (0.93σ and 1.61σ for the *Point* and *Extended* analyses, respectively) in 513 minutes of live time. Locally the significance reached 2.73σ (2.78σ) for the *Point* (*Extended*) analysis at $(l, b) = (71^\circ 07, 1^\circ 04)$ ($(71^\circ 51, 1^\circ 24)$) lying at a distance of $0^\circ 29$ ($0^\circ 20$) from the source. At the location of 2HWC J2024+417* an RBM analysis showed significances of 0.93σ (1.61σ) for the *Point* (*Extended*) analysis with 2428 minutes of live time.

Upper limits on the fluxes from WR 146 and WR 147 were reported in Aliu et al. (2008) at $5.6 \times 10^{-13} \text{ cm}^{-2} \text{ s}^{-1}$ and $7.3 \times 10^{-13} \text{ cm}^{-2} \text{ s}^{-1}$ above 600 GeV. The results presented here represent an improvement by approximately a factor of two over both of these results.

It is interesting to examine whether there is any evidence of emission that is not detectable for any of the locations individually. If so, this would show up as a positive mean significance across all 71 results. The mean significances for all of the upper limit positions are 0.33 and 0.18 for the *Point* and *Extended* integration regions, respectively. To test whether these positive mean significances are significant, deviations from the expected mean significances of zero comparisons are made with the same number of significances drawn at random from the significance sky maps shown in Section 4 but with the VHE sources masked out. This was repeated 500,000 times using both the *Point* and *Extended* sky maps (Figure 8). From the *Point* sky map a mean significance of at least 0.33σ occurred 1029 times, giving a probability of occurrence of 2.1×10^{-3} (a 2.9σ fluctuation), whereas for the *Extended* sky map a deflection of at least 0.18σ occurred 21,091 times with probability 4.22×10^{-2} (a 1.7σ fluctuation). There is no

³⁷ Throughout this paper, the Crab Nebula flux is taken from Aharonian et al. (2004).

Table 1
VERITAS Upper Limits of the Integral and Differential Flux for a Variety of Locations that Could Emit VHE γ -rays

Source	l (deg)	b (deg)	Class	Live Time (minutes)	Point							Extended						
					ON	OFF	α	Sig. σ	Energy Thresh.	Int. UL	Diff. UL	ON	OFF	α	Sig.	Energy Thresh.	Int. UL	Diff. UL
2HWC J1953+294	65.85	1.07	U	109	4	50	0.027	1.8	790	3.16E-12	3.37E-15	10	98	0.073	0.8	790	2.6E-12	2.78E-15
2HWC J2006+341	71.32	1.16	U	513	12	214	0.038	0.9	500	9.7E-13	5.16E-16	67	392	0.117	1.6	500	1.98E-12	1.06E-15
2HWC J2024+417*	79.75	2.21	U	2428	69	1503	0.042	0.8	600	3.65E-13	2.57E-16	280	1945	0.137	1.9	600	6.66E-13	4.68E-16
3A 1954+319	68.39	1.93	LMXB	702	22	372	0.037	1.6	660	9.35E-13	7.58E-16	57	648	0.096	-0.8	550	6.57E-13	4.02E-16
3FGL J1951.6+2926	65.67	1.32	SPP	109	2	53	0.025	0.5	790	2.2E-12	2.35E-15	8	109	0.068	0.2	870	1.89E-12	2.31E-15
3FGL J1958.6+2845	65.88	-0.35	PSR	89	2	66	0.029	0.1	660	2.28E-12	1.84E-15	7	131	0.091	-1.4	660	1.48E-12	1.19E-15
3FGL J2004.4+3338	70.67	1.19	U	504	7	215	0.037	-0.6	550	4.39E-13	2.69E-16	60	387	0.109	1.6	500	1.98E-12	1.06E-15
3FGL J2018.5+3851	76.59	1.66	BCU	2336	43	995	0.042	0.2	600	2.98E-13	2.1E-16	238	1784	0.125	0.3	600	4.63E-13	3.26E-16
3FGL J2018.6+4213	79.4	3.53	U	1034	32	614	0.046	0.4	660	5.3E-13	4.28E-16	170	951	0.16	0.3	660	8.65E-13	7.02E-16
3FGL J2021.5+4026	78.23	2.08	PSR	2129	69	1029	0.063	0.5	660	3.54E-13	2.85E-16	338	1896	0.18	-0.2	660	3.9E-13	3.15E-16
3FGL J2023.5+4126	79.25	2.34	U	3305	89	1952	0.039	0.9	600	3.9E-13	2.75E-16	484	3486	0.112	2.6	600	8.38E-13	5.9E-16
3FGL J2025.2+3340	73.1	-2.41	BCU	101	0	35	0.025	0	550	1.34E-12	8.24E-16	3	74	0.069	-0.8	550	1.78E-12	1.09E-15
3FGL J2028.5+4040c	79.19	1.13	U	3785	89	1867	0.049	0.5	550	1.72E-13	1.05E-16	471	3023	0.151	1.2	550	2.35E-13	1.44E-16
3FGL J2030.0+3642	76.13	-1.43	PSR	974	26	439	0.045	1.4	600	6.93E-13	4.87E-16	105	777	0.149	-0.1	600	4.23E-13	2.97E-16
3FGL J2030.8+4416	82.35	2.89	PSR	251	8	201	0.047	-1	660	6.7E-13	5.41E-16	39	355	0.1	0.5	550	3.06E-12	1.87E-15
3FGL J2032.5+3921	78.57	-0.27	U	652	18	550	0.039	-0.8	550	5.14E-13	3.14E-16	104	938	0.12	-1	550	6.47E-13	3.97E-16
3FGL J2032.5+4032	79.51	0.44	U	3239	100	1466	0.057	1.9	550	4.75E-13	2.91E-16	415	2294	0.183	0.6	550	4.07E-13	2.49E-16
3FGL J2034.4+3833c	78.16	-1.04	U	270	7	285	0.037	-1.2	550	7.09E-13	4.34E-16	51	500	0.107	-0.5	550	1.48E-12	9.02E-16
3FGL J2034.6+4302	81.77	1.6	U	760	29	655	0.037	1.1	600	9.44E-13	6.68E-16	146	1339	0.107	0.7	600	1E-12	7.03E-16
3FGL J2035.0+3634	76.63	-2.32	U	54	0	49	0.032	0	720	1.1E-12	1.02E-15	6	90	0.111	-1	720	2.24E-12	2.08E-15
3FGL J2038.4+4212	81.53	0.54	U	1880	46	1139	0.04	0.7	600	2.94E-13	2.07E-16	190	2079	0.123	-2.5	600	1.05E-13	7.41E-17
3FGL J2039.4+4111	80.83	-0.21	U	2015	40	1107	0.045	-0.8	550	2.02E-13	1.24E-16	260	2090	0.14	0	550	2.76E-13	1.69E-16
3FGL J2042.4+4209	81.93	-0.07	U	462	17	383	0.039	0.1	660	8.21E-13	6.64E-16	77	774	0.11	-0.6	660	6.17E-13	4.98E-16
3FHL J1950.5+3457	70.3	4.3	U	282	3	102	0.041	-0.7	790	4.33E-13	4.62E-16	27	182	0.124	-0.3	790	7.82E-13	8.35E-16
3FHL J2026.7+3449	74.21	-1.99	U	152	0	85	0.038	0	660	4.11E-13	3.31E-16	17	143	0.128	0.3	600	1.35E-12	9.49E-16
Cygnus X-1	71.33	3.07	HMXB	871	13	254	0.061	-1.1	600	1.86E-13	1.3E-16	107	416	0.2	1	600	8.85E-13	6.21E-16
Cygnus X-3	79.85	0.7	HMXB	1269	52	268	0.136	2.3	500	7.47E-13	3.98E-16	475	1551	0.301	1.4	550	6.69E-13	4.1E-16
EXO 2030+375	77.15	-1.24	HMXB	359	12	263	0.042	0.2	600	1.06E-12	7.45E-16	70	468	0.137	0.2	660	1.44E-12	1.17E-15
G65.7+1.2	65.7	1.2	SNR	37	1	25	0.026	0.4	790	3.73E-12	3.98E-15	6	43	0.074	1.3	790	6.33E-12	6.75E-15
G65.8-0.5	65.8	-0.5	SNR	89	1	75	0.028	-0.8	660	1.52E-12	1.23E-15	7	152	0.078	-1.5	660	1.55E-12	1.25E-15
G66.0-0.0	66	-0	SNR	126	2	94	0.031	-0.6	660	1.36E-12	1.1E-15	11	175	0.092	-1.3	720	1.16E-12	1.08E-15
G67.6+0.9	67.6	0.9	SNR	624	14	326	0.038	-0.4	660	4.37E-13	3.54E-16	61	638	0.095	-0.6	660	6.1E-13	4.93E-16
G67.7+1.8	67.7	1.8	SNR	609	13	314	0.038	0.2	660	5.15E-13	4.17E-16	68	635	0.099	0.1	660	8.38E-13	6.75E-16
G67.8+0.5	67.8	0.5	SNR	537	18	238	0.05	1.3	600	8.93E-13	6.28E-16	95	443	0.152	2	600	1.8E-12	1.27E-15
G68.6-1.2	68.6	-1.2	SNR	424	5	229	0.037	-1.5	600	3.99E-13	2.8E-16	29	383	0.1	-2	550	5.97E-13	3.66E-16
G69.0+2.7	69	2.7	SNR	582	11	279	0.036	-0.1	550	5.88E-13	3.6E-16	59	496	0.099	0.6	550	1.26E-12	7.68E-16
G69.7+1.0	69.68	1.01	SNR	655	23	278	0.036	3	550	1.65E-12	1.02E-15	80	549	0.099	2.3	550	2.05E-12	1.26E-15
G73.9+0.9	73.9	0.9	SNR	2633	52	727	0.059	0.6	600	3.16E-13	2.23E-16	229	949	0.205	0.9	550	7.05E-13	4.34E-16
G76.9+1.0	76.89	0.97	SNR	2028	42	811	0.049	0.4	550	4.04E-13	2.48E-16	198	1136	0.191	-0.2	600	3.07E-13	2.16E-16
G83.0-0.3	83	-0.3	SNR	108	4	91	0.042	0	660	1.7E-12	1.38E-15	30	192	0.125	1	660	3.85E-12	3.11E-15
GS 2023+338	73.12	-2.09	LMXB	101	1	38	0.032	-0.2	550	1.64E-12	1.01E-15	10	82	0.09	0.8	550	3.39E-12	2.07E-15
HD 190603	69.49	0.39	CWB	471	14	209	0.044	1.2	550	1.09E-12	6.66E-16	44	436	0.118	-1.7	550	4.39E-13	2.69E-16
KS 1947+300	66.01	2.08	HMXB	165	1	83	0.03	-1	790	6.26E-13	6.67E-16	17	163	0.082	0.8	790	1.88E-12	2.01E-15
FGL J1949.0+3412	69.49	4.21	U	338	7	144	0.036	0.6	660	9.5E-13	7.67E-16	29	241	0.091	0.9	660	1.74E-12	1.4E-15
FGL J1955.0+3319	69.36	2.68	U	417	10	183	0.043	0.3	550	7.84E-13	4.8E-16	50	294	0.13	0.8	550	1.49E-12	9.11E-16
FGL J2005.7+3417	71.36	1.3	U	644	14	272	0.036	0.9	500	8.73E-13	4.66E-16	78	519	0.11	1.4	500	1.76E-12	9.38E-16

Table 1
(Continued)

Source	l (deg)	b (deg)	Class	Live Time (minutes)	Point							Extended						
					ON	OFF	α	Sig. σ	Energy Thresh.	Int. UL	Diff. UL	ON	OFF	α	Sig.	Energy Thresh.	Int. UL	Diff. UL
FGL J2009.9+3544	73.04	1.36	U	537	8	218	0.04	−0.6	500	4.58E−13	2.44E−16	62	345	0.126	1.4	500	1.81E−12	9.65E−16
FGL J2017.3+3526	73.62	−0.07	U	2501	38	1004	0.044	−0.8	600	1.41E−13	9.9E−17	211	1548	0.144	−1.1	550	2.44E−13	1.49E−16
FGL J2018.1+4111	78.47	3.03	U	2077	73	883	0.071	1.3	720	3.8E−13	3.52E−16	316	1305	0.245	0.3	660	4.2E−13	3.4E−16
FGL J2022.6+3727	75.88	0.21	U	4606	91	1455	0.059	−0.3	550	1.36E−13	8.34E−17	402	2182	0.171	0.7	550	3.27E−13	2E−16
FGL J2024.4+3957	78.13	1.35	U	1443	36	597	0.057	−0	600	2.91E−13	2.05E−16	183	804	0.208	0.9	550	7.69E−13	4.71E−16
FGL J2025.9+3904	77.58	0.61	U	818	25	359	0.057	1.2	550	8.74E−13	5.35E−16	108	527	0.207	0.7	550	1.05E−12	6.43E−16
FGL J2029.4+3940	78.46	0.41	U	1088	26	681	0.036	0.3	550	6.15E−13	3.77E−16	161	1248	0.111	1.8	550	1.67E−12	1.02E−15
FGL J2031.3+3857	78.1	−0.32	U	490	17	391	0.044	−0.1	550	7.53E−13	4.62E−16	98	658	0.143	0.9	550	1.55E−12	9.47E−16
FGL J2032.7+4333	81.96	2.19	U	540	14	498	0.039	−1.2	600	4.59E−13	3.23E−16	83	941	0.115	−1.9	600	4.53E−13	3.19E−16
FGL J2032.9+3956	79.08	0.03	U	2788	49	1578	0.032	−0.3	550	2.75E−13	1.68E−16	265	2710	0.096	−0.2	550	4.37E−13	2.68E−16
FGL J2034.3+4219	81.14	1.23	U	3284	74	1821	0.038	0.6	550	2.73E−13	1.67E−16	376	3214	0.108	0.8	550	4.32E−13	2.65E−16
FGL J2036.9+4314	82.16	1.39	U	393	17	294	0.039	1.1	660	1.21E−12	9.77E−16	78	537	0.116	0.8	660	1.26E−12	1.02E−15
FGL J2037.0+4005	79.67	−0.53	U	1750	26	890	0.037	−1.6	550	1.81E−13	1.11E−16	168	1509	0.124	−1.9	550	2.52E−13	1.55E−16
FGL J2037.6+4152	81.15	0.47	U	2253	79	1216	0.048	2.8	550	6.57E−13	4.02E−16	323	2159	0.16	1.1	550	2.37E−13	1.46E−16
FGL J2038.8+4235	81.85	0.72	U	809	18	648	0.034	−1	600	3.53E−13	2.48E−16	123	1301	0.1	−0.2	600	4.97E−13	3.5E−16
FGL J2040.1+4152	81.43	0.1	U	1898	46	1201	0.035	1.1	600	4.37E−13	3.08E−16	230	2391	0.103	0.8	550	3.62E−13	2.21E−16
FGL J2054.6+4130	82.85	−2.23	U	55	2	59	0.024	0.4	720	4.47E−12	4.15E−15	5	109	0.071	−1	720	2.54E−12	2.36E−15
PSR J1952+3252	68.76	2.82	PSR	526	16	245	0.037	1.7	550	1.31E−12	8.03E−16	37	450	0.091	−1.1	550	6.04E−13	3.7E−16
PSR J2006+3102	68.67	−0.53	PSR	424	10	234	0.048	−0.4	550	5.53E−13	3.38E−16	54	355	0.156	−0.6	550	8.02E−13	4.92E−16
WR 133	72.65	2.07	CWB	535	9	237	0.04	−0.2	500	6.46E−13	3.45E−16	48	414	0.124	−0.8	500	7.18E−13	3.83E−16
WR 137	74.33	1.09	CWB	3119	64	882	0.055	1.8	600	4.37E−13	3.07E−16	231	1547	0.143	−0.1	600	4.02E−13	2.83E−16
WR 140	80.93	4.18	CWB	110	5	99	0.03	1	600	3.77E−12	2.66E−15	17	210	0.087	−0.3	550	3.13E−12	1.91E−15
WR 146	80.56	0.44	CWB	3273	92	1194	0.07	1.9	550	3.01E−13	1.84E−16	273	1839	0.145	1.7	550	4.4E−13	2.69E−16
WR 147	79.85	−0.31	CWB	2135	48	1049	0.043	0.2	550	3.61E−13	2.21E−16	272	1780	0.145	0.4	550	5.81E−13	3.56E−16
XTE J2012+381	75.39	2.25	LMXB	1342	38	597	0.047	0.8	660	5.15E−13	4.16E−16	153	807	0.193	−1.7	600	2.73E−13	1.92E−16

Note. The upper limits were calculated using the method of Rolke (Rolke et al. 2005) at the 95% level and with an assumed spectral index of -2.5 . They have a mean decorrelation energy of 980 GeV and a standard deviation on the decorrelation energy of 100 GeV. Sources identified as simply FGL are found in the analysis of *Fermi*-LAT data performed for this work and are reported here (and in Table 3) for the first time. ON are the counts from within the integration region, OFF are the counts from the background regions, and α is the ratio of the number of signal to background regions. Sig. is the significance calculated using the RR method (Section 2, in σ), *Energy Thresh.* is the energy threshold (in GeV), *Int. UL* is the integral upper limit in units of $\text{cm}^{-2} \text{s}^{-1}$ between the energy threshold and 3×10^4 GeV, and *Diff. UL* is the differential upper limits in units of $\text{cm}^{-2} \text{s}^{-1} \text{GeV}^{-1}$ and at an energy of 1000 GeV. SNR = supernova remnant; HMXB = high mass X-ray binary; LMXB = low mass X-ray binary; CWB = particle-accelerating colliding-wind binary; BCU = active galaxy of uncertain type; U = unknown.

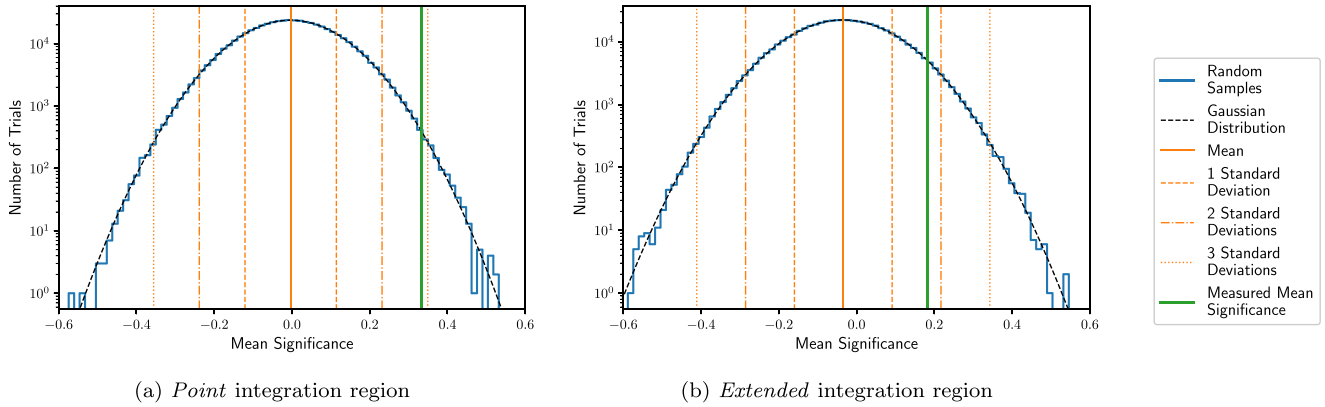


Figure 8. Histograms of mean significances calculated from 71 random locations outside the source exclusion regions in the significance sky map repeated 50,000 times for both the (a) *Point* and (b) *Extended* integration regions. The blue line shows the results of the test; the black dashed line is the best-fit Gaussian distribution. The mean and the one, two, and three standard deviations of the distribution are shown in orange. Note that the mean significance is slightly less than zero in both instances, reflecting the fact that the locations of bright stars have not been excluded from the possible locations of the randomly drawn locations. The mean of the significance of the upper limit locations is marked by the green line and in both cases is clearly offset from the mean, corresponding to 2.9σ and 1.7σ fluctuations for the *Point* and *Extended* integration regions, respectively.

significant evidence for additional sources with fluxes that are just below the sensitivity of this work.

In addition to calculating upper limits at specific locations for the chosen sources, we calculated an upper limit map for each of the integration regions. Upper limits were calculated using the method of Rolke (Rolke et al. 2005) at the 95% level (statistical uncertainty only) and with an assumed spectral index of -2.5 and using the ring background method and are presented in Figure 9.

5. *Fermi*-LAT Results

The *Fermi*-LAT counts map of the survey region is shown in Figure 10, together with the locations (and extensions for extended sources) of the 3FGL sources and the new sources identified in this analysis. In the survey region 27 3FGL catalog sources were identified, which overlap with eight 1FHL sources and four 2FHL sources. The 3FGL sources in this region that were removed from the model owing to their low TS (<25) are listed in Table 7. In addition, 25 new point sources were identified within the survey region. This number of new sources is not unexpected as a result of two main factors: the increase in the exposure time (7.5 yr rather than 4 yr) and the increased sensitivity of Pass 8 in comparison to Pass 7 (the increase in the differential sensitivity is about a factor of 1.25 above 1 GeV). Furthermore, nine of the new sources lie within the Cygnus Cocoon. It is noted that in the residual map of this analysis a deficit was located in the region around $(l, b) = (81^\circ, 2^\circ.5)$. The low-TS sources around the edge of the Cygnus Cocoon, along with this deficit, suggest that the symmetrical Gaussian model of the cocoon is overly simplistic. However, producing a more detailed analysis of the region with an improved model of the Cygnus Cocoon is beyond the scope of this work. The results for individual *Fermi* catalog sources are presented in Table 2, with their SEDs shown in Figure 7. The results for the new sources identified in this analysis are presented in Table 3 and Figure 7.

There are two 3FHL catalog sources that were not detected in this analysis, 3FHL J1950.5+3457 and 3FHL J2026.7+3449. Both of these sources are close to the 3FHL detection threshold (5.5σ and 4.2σ , respectively) and are hard (spectral indices of -1.8 and -1.9 , respectively). Combined with the

higher energy threshold of the 3FHL (10 GeV versus 1 GeV), this could explain why neither of these sources is detected in this analysis.

6. Results for Known VHE Sources and Other Objects of Interest

6.1. VER J2031+415

6.1.1. Background

In the vicinity of Cygnus OB2, the γ -ray source TeV J2032+4130 was the first unidentified VHE γ -ray source. It was discovered with the HEGRA IACTs (Aharonian et al. 2005) and has been further studied by the Whipple (Konopelko et al. 2007), MAGIC (Albert et al. 2008), and VERITAS (Aliu et al. 2014a) IACTs. As the position of the source is coincident with the Cygnus OB2 star association and located north of the microquasar Cygnus X-3, it was suggested that these two sources could be the origin of the VHE γ -rays (Aharonian et al. 2002). More recently, it has been argued that the VHE source could be the PWN of the GeV pulsar PSR J2032+4127 (Aliu et al. 2014a; Camilo et al. 2009). Lyne et al. (2015) suggested that PSR J2032+4127 is part of a binary system with a $15 M_\odot$ Be star, though the authors argue that this binary might not be able to fully power the VHE emission. Observations of the region during the 2017 November periastron found correlated X-ray and γ -ray emission from the direction of the pulsar, confirming the binary nature of the system (Veritas & MAGIC Collaborations 2017); a paper is in preparation to present these results.

VER J2031+415 is located in the Cygnus Cocoon, a large excess of hard spectrum emission detected by *Fermi*-LAT that is associated with the star-forming region Cygnus X and has the potential to be detected at VHE energies (Ackermann et al. 2011). The extensive air shower arrays Milagro and ARGO-YBJ have detected extended emission coming from the same region (MGRO J2031+41, Abdo et al. 2007; ARGO J2031+4157, Bartoli et al. 2012) at energies above 20 and 1 TeV, respectively, and these sources have been associated with the Cygnus Cocoon. The Cygnus Cocoon overlaps with, but extends beyond, TeV J2032+4130, and the extent of this emission makes it unlikely to be detectable by VERITAS using conventional techniques. Localized sources of emission

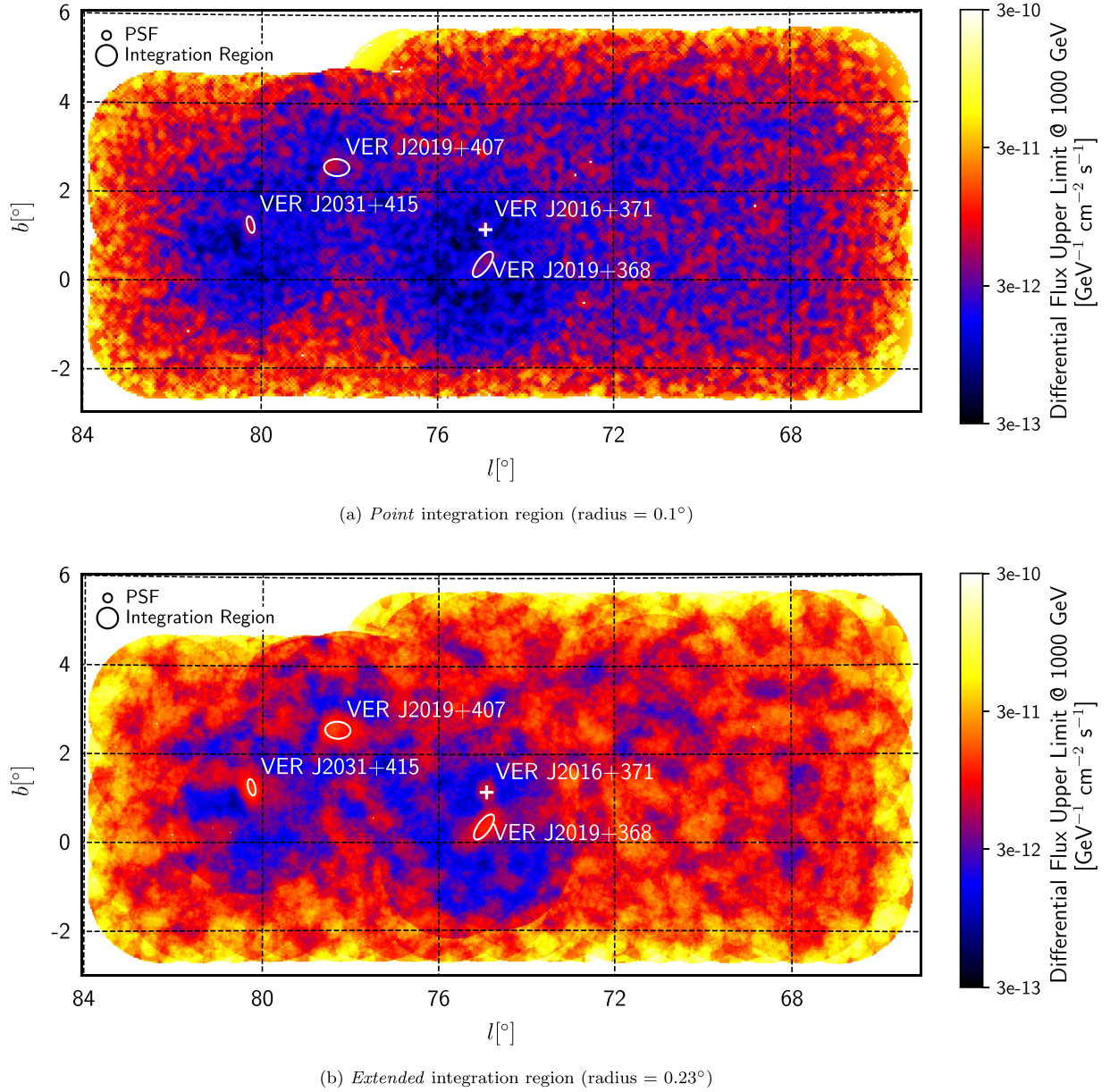


Figure 9. Map of the 95% upper limits on the differential flux at 1000 GeV using the *Point* (0.1°) and *Extended* (0.23°) integration radii. Upper limits were calculated using the method of Rolke (Rolke et al. 2005) at the 95% level and with an assumed spectral index of -2.5 and using the ring background method. Areas around known sources and bright stars were excluded from background regions. Overlaid are the 1σ ellipses for the source extension fits with an asymmetric Gaussian function for the three extended sources (VER J2019+407, VER J2031+415, VER J2019+368) and the position for VER J2016+371 (plus sign).

(of which TeV J2032+4130 could be an example) within the Cygnus Cocoon may be detectable, and IACT observations may be able to identify the sources that are powering this emission. Identification of the origin of the VHE emission from TeV J2032+4130 could help clarify the origin of the emission from this complex region.

6.1.2. Results

In this analysis, VER J2031+415 was observed by VERITAS at a peak (local) significance of 10.1σ using the *Extended* integration radius. As in Aliu et al. (2014a), the source was found to be extended and asymmetrical. The extension was fit with an asymmetrical Gaussian function and is given in Table 4.

The *Fermi*-LAT emission in the region is dominated by the pulsar PSR J2032+4127 (3FGL J2032.2+4126), which cuts off sharply at a few GeV. To investigate the possibility of an additional source (e.g., a PWN) that is masked by the emission from PSR J2032+4127, a gated analysis was performed to remove the pulsed component using the method outlined in Section 3, with the OFF-pulse selected using phases 0.1 to 0.4 and 0.5 to 0.9. This analysis showed an extended residual, as depicted in Figure 11, with a centroid of $(l, b) = (80^\circ 24 \pm 0^\circ 03_{\text{stat}}, 1^\circ 04 \pm 0^\circ 03_{\text{stat}})$ ($(\alpha_{J2000}, \delta_{J2000}) = 20^{\text{h}} 32^{\text{m}} 13^{\text{s}}, 41^\circ 28' 39''$). This residual is fit by an extended symmetric Gaussian source of 68% containment radius of $0^\circ 15^{+0.02}_{-0.03}$ centered on this location. Thus, we name the source FGL J2032.2+4128e. This source has a TS of 321.1, and the TS of extension is 28.6. A uniform disk source was also tested; the

Table 2
 >1 GeV *Fermi*-LAT Analysis Results for 3FGL Sources that Lie within the Survey Region

Source Name	l (deg)	b (deg)	Associations	Class	TS	Spectral Type	N_0 (GeV $^{-1}$ cm $^{-2}$ s $^{-1}$)	E_0/E_b (GeV)	γ	β/E_c (GeV)
3FGL J1951.6+2926	65.67	1.32	None	SPP	60.7	PL	$(6.29 \pm 0.88)\text{E-}10$	1.66	3.37 ± 0.27	N/A
3FGL J1952.9+3253	68.78	2.83	PSR J1952+3252 1FHL J1953.3+3251	PSR	10581.3	PLEC	$(7.52 \pm 0.34)\text{E-}8$	0.67	2.02 ± 0.08	5.56 ± 0.72
3FGL J1958.6+2845	65.88	-0.35	LAT PSR J1958+2846 1FHL J1958.6+2845 3EG J1958+2909	PSR	4959.8	PLEC	$(2.71 \pm 0.10)\text{E-}8$	1.02	2.17 ± 0.11	5.60 ± 1.03
3FGL J2004.4+3338	70.67	1.19	1FHL J2004.4+3339	U	582.2	PL	$(5.21 \pm 0.29)\text{E-}10$	2.67	2.47 ± 0.07	N/A
3FGL J2015.6+3709	74.89	1.2	MG2 J201534+3710 VER J2016+371 1FHL J2015.8+3710 3EG J2016+3657	FSRQ	1999.2	LP	$(5.46 \pm 0.19)\text{E-}9$	1.52	2.63 ± 0.07	0.02 ± 0.04
3FGL J2017.9+3627	74.54	0.41	MGRO J2019+37 PSR J2017+3625	PSR	1529.8	LP	$(5.38 \pm 0.21)\text{E-}9$	1.65	2.47 ± 0.11	0.69 ± 0.12
3FGL J2018.5+3851	76.59	1.66	TXS 2016+386 1FHL J2018.3+3851	BCU	149.6	PL	$(8.29 \pm 0.88)\text{E-}11$	4.18	2.26 ± 0.10	N/A
3FGL J2018.6+4213*	79.4	3.53	None	U	34.8	PL	$(5.62 \pm 1.12)\text{E-}11$	3.66	2.31 ± 0.20	N/A
3FGL J2021.0+4031e	78.24	2.2	Gamma Cygni VER J2019+407 1FHL J2021.0+4031e 1AGL J2022+4032	SNR	971.8	PL	$(3.04 \pm 0.12)\text{E-}10$	6.78	2.05 ± 0.03	N/A
3FGL J2021.1+3651	75.23	0.11	PSR J2021+3651 MGRO J2019+37 1FHL J2021.0+3651 1AGL J2021+3652	PSR	42295	PLEC	$(1.80 \pm 0.03)\text{E-}7$	0.84	2.03 ± 0.05	5.00 ± 0.35
3FGL J2021.5+4026	78.23	2.08	LAT PSR J2021+4026 1AGL J2022+4032	PSR	57923.9	PLEC	$(5.09 \pm 0.10)\text{E-}7$	0.66	1.98 ± 0.05	3.32 ± 0.19
3FGL J2022.2+3840*	76.85	0.96	None	SPP	100.1	PL	$(1.66 \pm 0.18)\text{E-}9$	1.45	3.74 ± 0.27	N/A
3FGL J2023.5+4126*	79.25	2.34	None	U	60.4	PL	$(1.76 \pm 0.26)\text{E-}10$	2.84	2.55 ± 0.16	N/A
3FGL J2025.2+3340	73.1	-2.41	B2 2023+33	BCU	206.3	PL	$(5.85 \pm 0.49)\text{E-}10$	2.03	2.86 ± 0.12	N/A
3FGL J2028.5 +4040c*	79.19	1.13	None	U	52	PL	$(8.46 \pm 1.25)\text{E-}10$	1.68	3.34 ± 0.28	N/A
3FGL J2028.6+4110e	79.6	1.4	Cygnus Cocoon MGRO J2031+41 1FHL J2028.6+4110e	SFR	3698.6	PL	$(6.70 \pm 0.12)\text{E-}9$	3.63	2.19 ± 0.02	N/A
3FGL J2030.0+3642	76.13	-1.43	PSR J2030+3641	PSR	1642.2	PLEC	$(9.87 \pm 1.51)\text{E-}9$	1.54	0.93 ± 0.28	1.82 ± 0.32
3FGL J2030.8+4416	82.35	2.89	LAT PSR J2030+4415	PSR	1237.8	PLEC	$(9.43 \pm 2.61)\text{E-}9$	1.6	1.73 ± 0.38	1.90 ± 0.58
3FGL J2032.2+4126	80.22	1.02	LAT PSR J2032+4127 TeV J2032+4130 1FHL J2032.1+4125 1AGL J2032+4102	PSR	3245	PLEC	$(1.08 \pm 0.05)\text{E-}8$	1.56	1.03 ± 0.12	3.65 ± 0.38
3FGL J2032.5+3921*	78.57	-0.27	None	U	38.6	PL	$(1.09 \pm 0.20)\text{E-}10$	3.13	2.57 ± 0.19	N/A
3FGL J2032.5+4032*	79.51	0.44	1AGL J2032+4102	U	28.2	PL	$(9.08 \pm 1.80)\text{E-}10$	1.5	3.60 ± 0.39	N/A
3FGL J2034.4 +3833c*	78.16	-1.04	None	U	57.5	LP	$(2.28 \pm 2.19)\text{E-}9$	0.53	1.34 ± 1.49	1.78 ± 0.59
3FGL J2034.6+4302*	81.77	1.6	None	U	32.9	PL	$(4.20 \pm 0.78)\text{E-}10$	1.85	3.14 ± 0.30	N/A
3FGL J2035.0+3634	76.63	-2.32	None	U	432.3	LP	$(7.72 \pm 0.63)\text{E-}10$	2.13	1.43 ± 0.19	0.88 ± 0.16
3FGL J2038.4+4212*	81.53	0.54	None	U	49	LP	$(6.70 \pm 1.63)\text{E-}10$	1.65	0.73 ± 0.53	1.66 ± 0.48
3FGL J2039.4+4111*	80.83	-0.21	None	U	89.5	PL	$(6.84 \pm 0.80)\text{E-}10$	1.87	2.96 ± 0.20	N/A
3FGL J2042.4+4209*	81.93	-0.07	None	U	92.1	PL	$(8.47 \pm 0.97)\text{E-}10$	1.75	3.14 ± 0.20	N/A

Note. For each source, the galactic coordinates for the source are listed together with the corresponding TS value at this location. Associations as listed are from the 3FGL. Source class definitions: PSR = pulsar; FSRQ = flat-spectrum radio quasar type of blazar; BCU = active galaxy of uncertain type; SNR = supernova remnant; SFR = star-forming region; SPP = special case, either SNR or PWN; U = unknown. Sources marked with a * next to their name lie in the field of the Cygnus Cocoon. The spectra were fit with a PL (Equation (1)), an LP (Equation (2)), or a PLEC (Equation (3)). The values for 3FGL J2015.6+3709 quoted in this table are from the best-fit location of $(l, b) = (74^\circ 89', 1^\circ 2') ((\alpha_{J2000}, \delta_{J2000}) = (20^{\text{h}}15^{\text{m}}39.2^{\text{s}}, 37^\circ 11' 31.1''))$; for details of this analysis see Section 6.4.

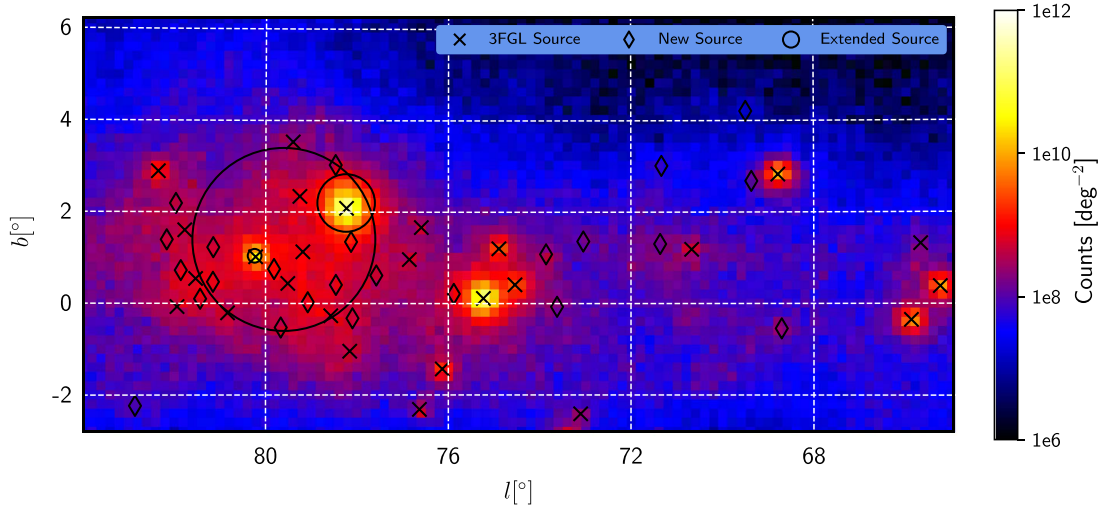


Figure 10. >1 GeV counts map of the entire region obtained with *Fermi*-LAT. Point sources of the 3FGL catalog that are significant in this analysis are shown with small black crosses; the extended sources are shown with larger circles showing their characteristic extension. New sources identified in this analysis are shown with black diamonds.

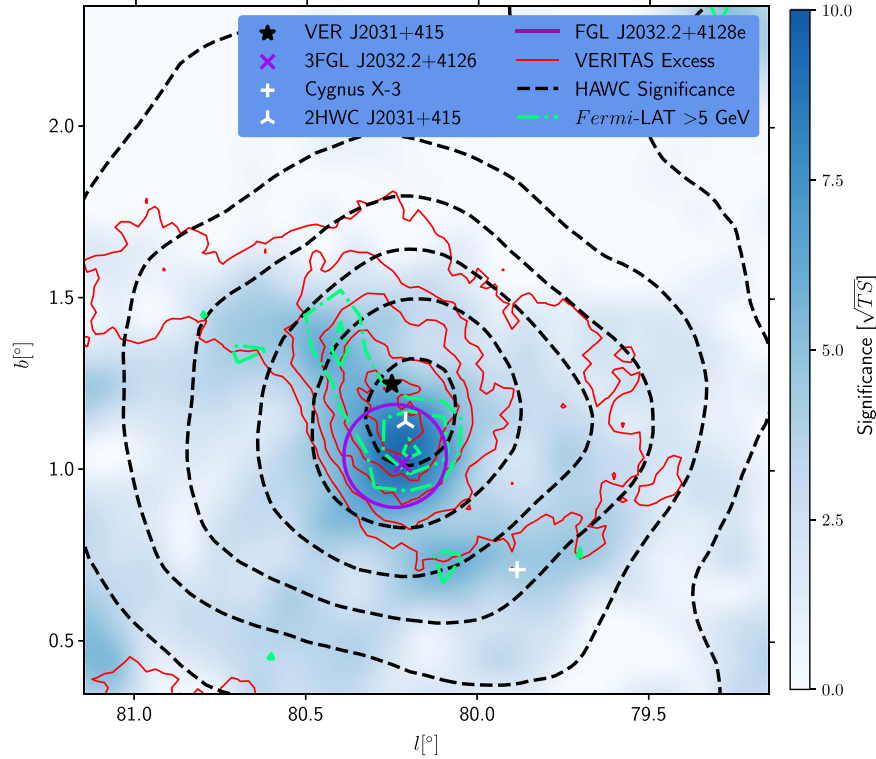


Figure 11. Significance (\sqrt{TS}) map of the *Fermi*-LAT observations in the region of VER J2031+415 with the pulsar PSR J2032+4127 (3FGL J2032.2+4126) fixed to the ON-pulse spectral parameters. The best-fit extension of FGL J2032.2+4128e, the source fit to this excess, is shown in purple. Overlaid with green dot-dashed contours are the (3, 4, 5) \sqrt{TS} contours from the analysis above 5 GeV. Also shown are VERITAS excess contours using the *Extended* integration region at levels of 50, 100, 150, 200, and 250 counts (red solid) and HAWC significance contours at 3σ , 4σ , 5σ , 6σ , and 7σ (black dashed). The locations of VER J2031+415 (black star), 3FGL J2032.3+4126 (purple cross), 2HWC J2031+415 (white three-pointed star), and Cygnus X-3 (white plus sign) are also indicated in the figure.

best fit had a 68% containment radius of $0^\circ.15^{+0.02}_{-0.02}$ and a TS of extension of 24.7. The Gaussian source morphology was preferred and used for the rest of this work.

A cross-check using an OFF-pulse analysis identified a similar residual with a comparable morphology, although, with the smaller statistics due to the combined effect of the phase cut and limited time period of the ephemeris (about a factor of 2 reduction in live time), the signal is weaker. The similarity in the morphology between these two methods of removing the

pulsar and the offset and extension in the residual is supportive of this residual being due to a new source rather than an artifact due to errors in fitting to PSR J2032+4127.

An additional analysis was conducted above 5 GeV; this has the advantage that the PSF is reduced at these energies (to around $0^\circ.3$ at 5 GeV), which will improve the ability to separate the two sources. This also found moderately extended emission potentially associated with VER J2031+415 with a TS of 31.7 as shown in Figure 11. A fit to this emission was conducted, and it

Table 3
 >1 GeV *Fermi*-LAT Analysis Results of Newly Identified Sources

Source Name	l (deg)	b (deg)	Association	Class	TS	N_0 ($\text{GeV}^{-1}\text{cm}^{-2}\text{s}^{-1}$)	E_0 (GeV)	γ	Notes
FGL J1949.0+3412	69.49	4.21	None	U	32.7	$(6.87 \pm 1.40)\text{E-11}$	2.62	2.54 ± 0.21	
FGL J1955.0+3319	69.36	2.68	None	U	49.5	$(1.94 \pm 0.31)\text{E-10}$	2.3	2.78 ± 0.20	
FGL J1958.6+3510	71.33	3.01	Cygnus X-1	HMXB	39.4	$(2.10 \pm 0.45)\text{E-11}$	4.78	2.18 ± 0.19	a
FGL J2005.7+3417	71.36	1.3	2HWC J2006+341	U	32.7	$(5.45 \pm 1.02)\text{E-10}$	1.61	3.22 ± 0.32	b
FGL J2006.3+3103	68.7	-0.55	PSR J2006+3102	PSR	111	$(3.62 \pm 0.40)\text{E-10}$	2.16	2.80 ± 0.14	c
FGL J2009.9+3544	73.04	1.36	HD 191612	HMXB	44.8	$(1.18 \pm 0.24)\text{E-11}$	6.75	2.03 ± 0.16	d
FGL J2013.3+3616	73.86	1.08	G73.9+0.9	SNR	147	$(5.42 \pm 0.52)\text{E-10}$	2.06	2.94 ± 0.14	e
FGL J2017.3+3526	73.62	-0.07	None	U	37	$(5.85 \pm 1.16)\text{E-11}$	3.47	2.39 ± 0.20	
FGL J2018.1+4111*	78.47	3.03	None	U	26.3	$(5.79 \pm 1.19)\text{E-10}$	1.62	3.48 ± 0.43	
FGL J2022.6+3727	75.88	0.21	None	U	55	$(7.81 \pm 1.12)\text{E-10}$	1.74	3.31 ± 0.24	
FGL J2024.4+3957*	78.13	1.35	None	U	56.6	$(6.73 \pm 0.96)\text{E-10}$	1.89	3.24 ± 0.24	
FGL J2025.9+3904	77.58	0.61	None	U	27.6	$(1.53 \pm 0.34)\text{E-9}$	1.26	3.63 ± 0.56	
FGL J2029.4+3940*	78.46	0.41	None	U	37.1	$(1.54 \pm 0.27)\text{E-9}$	1.34	4.10 ± 0.51	
FGL J2031.3+3857	78.1	-0.32	None	U	43.2	$(5.72 \pm 0.93)\text{E-10}$	1.78	3.06 ± 0.27	
FGL J2032.1+4058*	79.81	0.75	Cygnus X-3	HMXB	34.9	$(3.31 \pm 0.60)\text{E-10}$	2.15	2.87 ± 0.23	f
FGL J2032.2+4128e*	80.24	1.04	None	U	321	$(1.44 \pm 0.09)\text{E-9}$	2.27	2.52 ± 0.07	
FGL J2032.7+4333	81.96	2.19	None	U	45.7	$(7.81 \pm 1.24)\text{E-10}$	1.59	3.34 ± 0.36	
FGL J2032.9+3956*	79.08	0.03	None	U	80.2	$(8.82 \pm 1.06)\text{E-10}$	1.77	3.24 ± 0.19	
FGL J2034.3+4219*	81.14	1.23	None	U	49.2	$(4.91 \pm 0.76)\text{E-10}$	1.9	3.11 ± 0.30	
FGL J2036.9+4314	82.16	1.39	None	U	40.8	$(9.24 \pm 1.54)\text{E-10}$	1.51	3.56 ± 0.41	
FGL J2037.0+4005*	79.67	-0.53	None	U	60	$(1.19 \pm 0.17)\text{E-9}$	1.49	3.69 ± 0.35	
FGL J2037.6+4152*	81.15	0.47	None	U	87	$(4.81 \pm 0.57)\text{E-10}$	2.16	2.87 ± 0.18	
FGL J2038.8+4235	81.85	0.72	None	U	87	$(2.65 \pm 0.33)\text{E-10}$	2.61	2.88 ± 0.18	
FGL J2040.1+4152	81.43	0.1	None	U	110	$(2.62 \pm 0.29)\text{E-10}$	2.72	2.62 ± 0.13	
FGL J2054.6+4130	82.85	-2.23	None	U	31	$(4.89 \pm 0.95)\text{E-10}$	1.58	3.36 ± 0.43	

Notes. All sources were fit with a power law (Equation (1)) and showed no significant evidence of curvature. Source class definitions are as in Table 2; sources marked with a * next to their name lie in the field of the Cygnus Cocoon.

^a FGL J1958.6+3510 is located close to Cygnus X-1 (separation = $3'6''$). Cygnus X-1 has previously been identified in Zanin et al. (2016) at $(\alpha_{J2000}, \delta_{J2000}) = (19^{\text{h}}58^{\text{m}}56^{\text{s}}.8, +35^{\circ}11'4''4)$, as well as being identified in Zdziarski et al. (2017).

^b FGL J2005.7+3417 lies $0^{\circ}15'$ away from 2HWC J2006+341, which has a 1σ positional uncertainty of $0^{\circ}13'$.

^c FGL J2006.3+3103 lies coincident with PSR J2006+3102 and was identified in Zanin et al. (2016) as being the most likely counterpart owing to the location and spectral shape. No search for pulsations has been conducted, and no evidence of spectral curvature was detected.

^d FGL J2009.9+3544 lies $0^{\circ}075'$ away from the source identified as n1 in Zdziarski et al. (2017), which they associated with HD 191612 ($0^{\circ}092'$ from FGL J2009.9+3544), an O8 high-mass binary detected by both *XMM-Newton* and *ROSAT*.

^e The addition of the new point source FGL J2013.3+3616 resulted in the removal of the 3FGL source 3FGL J2014.4+3606 (TS < 25). This source lies $12'$ away from the center of SNR G73.9+0.9 (which has an extension of $27'$; Green 2014). This association has previously been reported in Zdziarski et al. (2016) and in Zanin et al. (2016). It is included in the ISC (Acero et al. 2016) as a marginally classified candidate with a TS of 30 at a position of $(l, b) = (73^{\circ}86', 0^{\circ}92')$ ($(\alpha_{J2000}, \delta_{J2000}) = (20^{\text{h}}13^{\text{m}}58^{\text{s}} \pm 10^{\text{s}}_{\text{stat}} \pm 26^{\text{s}}_{\text{sys}}, 36^{\circ}10'48'' \pm 10''_{\text{stat}} \pm 22''_{\text{sys}})$).

^f FGL J2032.1+4058 lies $4'$ away from Cygnus X-3 and close to the previously reported 1FGL and 2FGL catalog sources 1FGL J2032.4+4057 and 2FGL J2032.1+4049, which were both associated with Cygnus X-3. It was not reported in the 3FGL owing to flux variability (Acero et al. 2015).

was found to peak at $(l, b) = (80^{\circ}21' \pm 0^{\circ}04'_{\text{stat}}, 1^{\circ}10' \pm 0^{\circ}04'_{\text{stat}})$ ($(\alpha_{J2000}, \delta_{J2000}) = (20^{\text{h}}31^{\text{m}}54^{\text{s}}, 41^{\circ}29'24'')$ with an extension of $0.14 \pm 0.05_{\text{stat}}$ and a TS of extension of 10.6.

It is noted that an analysis of the *Fermi*-LAT data from the Cygnus Cocoon region is very complex, and in this analysis, a simplistic model of the cocoon emission was used (a single symmetric Gaussian as in the 3FGL). Further work with a more detailed morphology of the Cygnus Cocoon has the potential to provide significantly more insight here but is beyond the scope of this work. In particular, there are significant challenges associated with disentangling the emission from the various objects and identifying whether an observed region of emission is associated with a peak in the emission from the Cygnus Cocoon or another source. At present, VHE emission is detected from either a significantly extended region (Milagro and ARGO-YBJ) associated with the Cygnus Cocoon or a smaller, moderately extended region (VERITAS, MAGIC, HEGRA, HAWC, and Whipple) associated with TeV J2032+4130. Understanding the relationship between these VHE

observations will significantly improve our ability to understand this region in other wavelengths. To do this will require further development of tools such as the “3D Maximum Likelihood Method” currently being developed (Weinstein 2014; Cardenzana 2017), which will allow for observations of significantly extended objects by VERITAS. This will then allow the superior PSF of VERITAS to be used to study the morphology of the Cygnus Cocoon, providing information that could be used to guide the HE analysis. Until then it is not possible to definitively claim the detection of an HE counterpart to VER J2031+415, nor to fully understand the relationship between the two objects. However, the presence of extended emission with similar morphology to those observed in VER J2031+415 is highly suggestive that there is HE emission associated with the source.

The spectra of VER J2031+415 and FGL J2032.2+4128e are shown in Figure 12. The VERITAS spectrum is given in Table 5, with the spectral points given in Table 8, and is consistent with the spectrum presented in Aliu et al. (2014a).

Table 4
Source Extension of the VERITAS Sources

Source	Centroid		$\sigma_{\text{semimajor}}$ (deg)	$\sigma_{\text{semiminor}}$ (deg)	Rotation Angle (deg)
	(l, b)	$(\alpha_{J2000}, \delta_{J2000})$			
VER J2031+415	$(80^{\circ}25 \pm 0^{\circ}01_{\text{stat}} \pm 0^{\circ}01_{\text{sys}}, 1^{\circ}20 \pm 0^{\circ}01_{\text{stat}} \pm 0^{\circ}01_{\text{sys}})$	$(20^{\text{h}}31^{\text{m}}33^{\text{s}}, 41^{\circ}34'48'')$	$0.19 \pm 0.02_{\text{stat}} \pm 0.01_{\text{sys}}$	$0.08 \pm 0.01_{\text{stat}} \pm 0.03_{\text{sys}}$	$13 \pm 4_{\text{stat}} \pm 1_{\text{sys}}$
VER J2019+407	$(78^{\circ}30 \pm 0^{\circ}02_{\text{stat}} \pm 0^{\circ}01_{\text{sys}}, 2^{\circ}55 \pm 0^{\circ}01_{\text{stat}} \pm 0^{\circ}01_{\text{sys}})$	$(20^{\text{h}}20^{\text{m}}05^{\text{s}}, 40^{\circ}45'36'')$	$0.29 \pm 0.02_{\text{stat}} \pm 0.02_{\text{sys}}$	$0.19 \pm 0.01_{\text{stat}} \pm 0.03_{\text{sys}}$	$176.7 \pm 0.1_{\text{stat}} \pm 2_{\text{sys}}$
VER J2019+368	$(74^{\circ}97 \pm 0^{\circ}02_{\text{stat}} \pm 0^{\circ}01_{\text{sys}}, 0^{\circ}35 \pm 0^{\circ}01_{\text{stat}} \pm 0^{\circ}01_{\text{sys}})$	$(20^{\text{h}}19^{\text{m}}23^{\text{s}}, 36^{\circ}46'44'')$	$0.34 \pm 0.02_{\text{stat}} \pm 0.01_{\text{sys}}$	$0.14 \pm 0.01_{\text{stat}} \pm 0.02_{\text{sys}}$	$127.0 \pm 2.6_{\text{stat}} \pm 0.1_{\text{sys}}$
VER J2018+367*	$(74^{\circ}87 \pm 0^{\circ}01_{\text{stat}} \pm 0^{\circ}01_{\text{sys}}, 0^{\circ}42 \pm 0^{\circ}01_{\text{stat}} \pm 0^{\circ}01_{\text{sys}})$	$(20^{\text{h}}18^{\text{m}}48^{\text{s}}, 36^{\circ}44'24'')$	$0.18 \pm 0.01_{\text{stat}} \pm 0.04_{\text{sys}}$	<i>Symmetric</i>	
VER J2020+368*	$(75^{\circ}13 \pm 0^{\circ}01_{\text{stat}} \pm 0^{\circ}01_{\text{sys}}, 0^{\circ}19 \pm 0^{\circ}01_{\text{stat}} \pm 0^{\circ}01_{\text{sys}})$	$(20^{\text{h}}20^{\text{m}}31^{\text{s}}, 36^{\circ}49'12'')$	$0.03 \pm 0.01_{\text{stat}} \pm 0.01_{\text{sys}}$	<i>Symmetric</i>	
VER J2016+371	$(74^{\circ}94 \pm 0^{\circ}01_{\text{stat}} \pm 0^{\circ}01_{\text{sys}}, 1^{\circ}16 \pm 0^{\circ}01_{\text{stat}} \pm 0^{\circ}01_{\text{sys}})$	$(20^{\text{h}}15^{\text{m}}57^{\text{s}}, 37^{\circ}12'31'')$	<i>Point Source</i>		

Note. The source extension was determined by fitting a sky map of the excess events with a 2D Gaussian distribution convolved with the VERITAS PSF. The rotation angle is given east of galactic north.

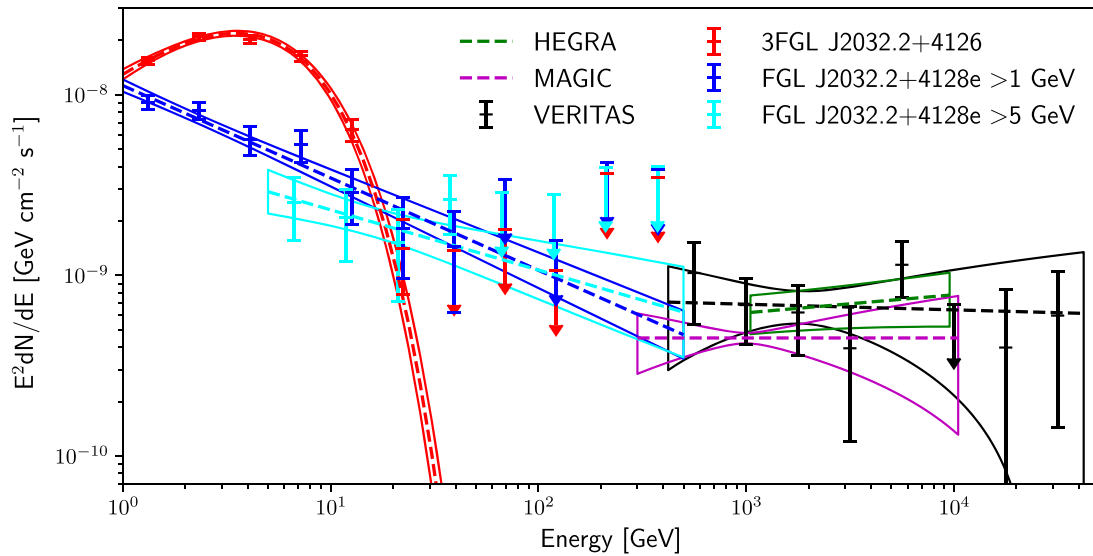


Figure 12. SEDs from sources in the VER J2031+415 region. Black is the VERITAS *Extended* analysis; blue is the FGL J2032.2+4128e fit above 1 GeV; cyan above 5 GeV, the *Fermi*-LAT source that is located at the same position as VER J2031+415 and is potentially the low-energy extension of this emission; red is 3FGL J2032.2+4126, the bright pulsar in the region. Also plotted are the TeV J2032+4130 results from HEGRA (Aharonian et al. 2005) and MAGIC (Albert et al. 2008). The butterflies show statistical errors only.

The spectrum of HE emission can be described by a power law with index $2.52 \pm 0.07_{\text{stat}}$ and a normalization of $(1.44 \pm 0.09_{\text{stat}}) \times 10^{-8} \text{ GeV}^{-1} \text{ cm}^{-2} \text{ s}^{-1}$ at 2.27 GeV. Comparing the spectra of FGL J2032.2+4128e and 3FGL J2032.2+4126 shows that, below 1 GeV, the extrapolated flux from FGL J2032.2+4128e would be stronger than that from 3FGL J2032.2+4126. This is clearly not the case, as it has not been detected in lower-energy analyses. It is likely, therefore, that at low energies some of the emission from 3FGL J2032.2+4126 and potentially the Cygnus Cocoon is being included in the measured flux from FGL J2032.2+4128e.

A joint fit to the VERITAS and *Fermi*-LAT data points for VER J2031+415/FGL J2032.2+4128e is well fit with a PL of index $2.39 \pm 0.03_{\text{stat}}$ and normalization $(3.61 \pm 0.21_{\text{stat}}) \times 10^{-10} \text{ GeV}^{-1} \text{ cm}^{-2} \text{ s}^{-1}$ at 4.04 GeV, with a χ^2 of 9.9 for 9 degrees of freedom (dof). However, it is clearly evident that the low-energy *Fermi*-LAT spectral points are contaminated with emission from 3FGL J2032.2+4126. To reduce the impact of this and better match the regions from which the VERITAS spectrum was extracted, the analysis above 5 GeV was used. This spectrum (index = $2.33 \pm 0.22_{\text{stat}}$, normalization = $(8.80 \pm 1.76_{\text{stat}}) \times 10^{-12} \text{ GeV}^{-1} \text{ cm}^{-2} \text{ s}^{-1}$ at 15.1 GeV, Figure 12) shows good agreement with the VERITAS spectrum for VER J2031+415, and together they are well fit with a PL of index $2.22 \pm 0.06_{\text{stat}}$ and normalization $(2.28 \pm 0.33_{\text{stat}}) \times 10^{-15} \text{ GeV}^{-1} \text{ cm}^{-2} \text{ s}^{-1}$ at 221 GeV with a χ^2 of 4.9 for 9 dof.

6.1.3. Discussion

VER J2031+415 has been detected by HAWC and is listed in the 2HWC catalog as 2HWC J2031+415. The VERITAS location lies just outside the HAWC 1σ uncertainty at a distance of $0^\circ.11$ (though the HAWC position lies within the 1σ extent of the VERITAS emission). HAWC sees evidence of extension with the source fit with both a point source and

uniform disk of radius $0^\circ.7$. This extension is larger than that measured by VERITAS and closer to the results from Milagro. Using both extensions, HAWC detects a higher flux $((3.24 \pm 0.32_{\text{stat}}) \times 10^{-17} \text{ GeV}^{-1} \text{ cm}^{-2} \text{ s}^{-1}$ and $(6.16 \pm 0.44_{\text{stat}}) \times 10^{-17} \text{ GeV}^{-1} \text{ cm}^{-2} \text{ s}^{-1}$ at 7000 GeV for the point and extended fit, respectively) and softer spectral index ($-2.57 \pm 0.07_{\text{stat}}$ and $-2.52 \pm 0.05_{\text{stat}}$) than reported in this work (and in previous observations by IACTs); this is likely due to contributions from the extended emission that is not detected by VERITAS.

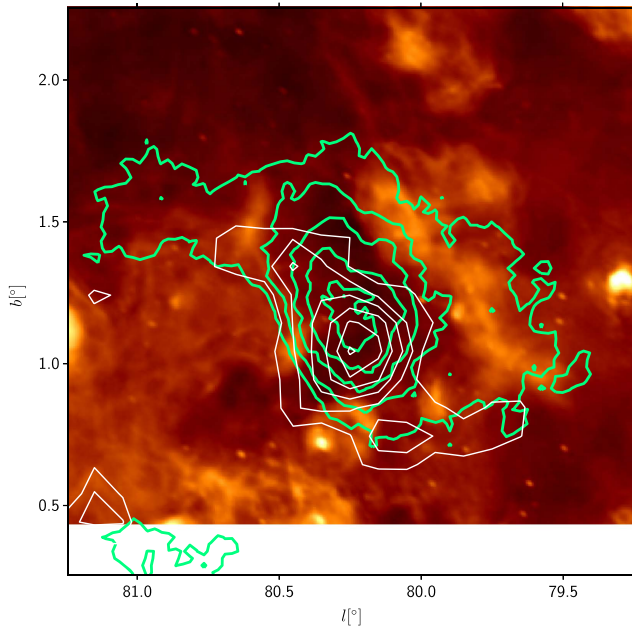
With similar morphologies and spectral properties, it is likely that both the HE and VHE emission share a common origin. Given the proximity of the emission from both sources to the pulsar PSR J2032+4127, a PWN origin of this emission is a strong possibility. However, Aliu et al. (2014a) comment that, taking into account the hard spectral index (~ -2) and due to the Klein-Nishina effect, a cutoff in the spectrum should be seen close to 10 TeV in order to be consistent with the PWN interpretation. Though it cannot be excluded using these data alone, there is no evidence of a spectral cutoff in these data, which would be expected with a PWN origin for the emission.

Multiwavelength images of TeV J2032+4130 and its vicinity are shown in Figure 13. The infrared images from *Spitzer* are dominated by bright diffuse emission exhibiting complex structure caused by star-forming activity taking place in the Cygnus X complex. In addition, as noted in Aliu et al. (2014a), nearly all the VHE γ -ray emission happens to be confined within a void. One possible explanation proposed by Butt et al. (2003) is that the large, mechanical power density from the stellar winds of the OB stars could be powering the emission. However, even though the energy required to power the VHE emission is a fraction of the estimated wind energy, almost all of the massive stars are located outside of the VHE emission region. It is also plausible that a supernova exploded within Cygnus OB2 and its remnant is expanding into the

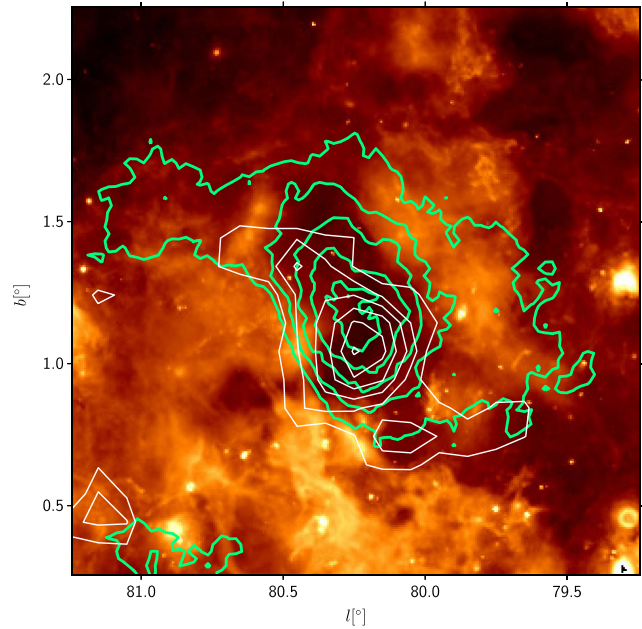
Table 5
Observation Results for the VERITAS Sources

Source	Integration Region	ON	OFF	α	Sig. (σ)	Fit Range (GeV)	N_0 ($\text{GeV}^{-1}\text{cm}^{-2}\text{s}^{-1}$)	E_0 (GeV)	γ	χ^2/dof
VER J2031+415	<i>Extended</i>	871	5181	0.114	10.1	422–42200	$(1.24 \pm 0.24_{\text{stat}} \pm 0.24_{\text{sys}})\text{E}-16$	2300	$2.00 \pm 0.19_{\text{stat}} \pm 0.20_{\text{sys}}$	3.02/5
VER J2019+407	<i>Extended</i>	598	2767	0.151	7.6	750–7500	$(5.01 \pm 0.93_{\text{stat}} \pm 1.00_{\text{sys}})\text{E}-16$	1500	$2.79 \pm 0.39_{\text{stat}} \pm 0.20_{\text{sys}}$	3.27/2
VER J2019+368	<i>Extended</i>	951	4230	0.153	10.3	422–42200	$(1.02 \pm 0.11_{\text{stat}} \pm 0.20_{\text{sys}})\text{E}-16$	3110	$1.98 \pm 0.09_{\text{stat}} \pm 0.20_{\text{sys}}$	8.73/6
VER J2018+367*	<i>Point</i>	196	3692	0.028	7.8	750–23700	$(5.12 \pm 0.94_{\text{stat}} \pm 1.48_{\text{sys}})\text{E}-17$	2710	$2.00 \pm 0.21_{\text{stat}} \pm 0.2_{\text{sys}}$	2.81/4
VER J2020+368*	<i>Point</i>	191	3456	0.030	7.5	750–23700	$(3.00 \pm 0.56_{\text{stat}} \pm 0.60_{\text{sys}})\text{E}-17$	3270	$1.71 \pm 0.26_{\text{stat}} \pm 0.2_{\text{sys}}$	4.71/4
VER J2016+371	<i>Point</i>	157	2370	0.038	6.3	680–14700	$(2.8 \pm 1.2_{\text{stat}} \pm 1.2_{\text{sys}})\text{E}-17$	2510	$2.1 \pm 0.8_{\text{stat}} \pm 0.4_{\text{sys}}$	0.38/2

Note. ON, OFF, and α are from the RBM analysis. The spectral analysis is conducted using the RR method (Section 2), and all sources were best fit with a power law (Equation (1)).



(a) 1420 MHz image from the Canadian Galactic Plane Survey. (Taylor et al. 2003)



(b) *Spitzer* MIPS 24 μ m image from the MIPS GAL survey.

Figure 13. Multiwavelength view of the region around VER J2031+415. Overlaid are VERITAS excess contours (green) produced using the *Extended* integration region at levels of 50, 100, 150, 200, and 250 counts and *Fermi*-LAT significance (\sqrt{TS} , white) at $1\sqrt{TS}$ levels above $4\sqrt{TS}$. Both the VERITAS emission and the *Fermi*-LAT emission are confined to a void in this multiwavelength emission.

surrounding medium, creating the void and powering the γ -ray emission.

6.2. VER J2019+407

6.2.1. Background

The γ -ray emission in the vicinity of the SNR G78.2+2.1, located in the region of Gamma Cygni, was first detected by the EGRET instrument on board the *Compton Gamma Ray Observatory* (CGRO; Thompson et al. 1995). There is a bright *Fermi*-LAT pulsar, PSR J2021+4026 (3FGL J2021.5+4026), at the center of the remnant (Abdo et al. 2010a, 2010b), as well as extended γ -ray emission above 10 GeV (3FGL J2021.0+4031e) with an extension consistent with that seen in radio observations of G78.2+2.1 (Lande et al. 2012). A VHE source, VER J2019+407, was detected by VERITAS at a level of 7.5σ on the northwestern rim of the radio shell of the SNR G78.2+2.1 (Aliu et al. 2013). HAWC has detected a source (2HWC J2020+403) that lies within G78.2+2.1, $0^\circ.43$ away from the location of VER J2019+407 and close to PSR J2021+4026. They do not report on any evidence of extension, and they report a power-law spectrum for flux $(1.85 \pm 0.26_{\text{stat}}) \times 10^{-17} \text{ GeV}^{-1} \text{ cm}^{-2} \text{ s}^{-1}$ at 7000 GeV and spectral index $(-2.95 \pm 0.10_{\text{stat}})$.

3FGL J2021.0+4031e is generally modeled as a uniform disk of radius $0^\circ.63$ (Acero et al. 2015), though Ackermann et al. (2011) found an improvement in their modeling of the region if, in addition to a disk source for the entire remnant, they included an elliptical source based on the morphology presented in Weinstein et al. (2009). Fraija & Araya (2016) conducted an analysis above 4 GeV that showed a region of enhanced emission in the GeV energy range over and above the uniform disk model that coincides with the VHE emission from VER J2019+407.

The radio emission is brightest at the opposite side of the SNR from VER J2019+407, on the southern edge of the remnant. Leahy et al. (2013) discuss the radio and X-ray emission in detail and note that there are several possible sources of radio emission in the same line of sight as the southern edge of the remnant, which could make the radio emission in that region appear higher than it actually is. In contrast, by examining *ROSAT* X-ray observations, they show that the diffuse emission is brightest at the northern and western edges. It is noted that the northern emission may, in part, be due to the presence of a large X-ray shell associated with the early-type star V1685 Cyg, which lies in the line of sight of G78.2+2.1 but at between one-half and one-third of the distance (980 pc, versus 1.7–2.6 kpc for G78.2+2.1; Green 2014). G78.2+2.1 lies within the Cygnus Cocoon and could power at least some of the high-energy emission seen from the region.

6.2.2. Results

In this analysis, VER J2019+407 was observed by VERITAS at a peak (local) significance of 7.6σ using the *Extended* integration region. The source was found to be extended and asymmetric, unlike the morphology reported in Aliu et al. (2013), where a symmetric fit was favored. It was fit with an asymmetric Gaussian with the results given in Table 4. This difference in morphology likely reflects the improved PSF in this analysis in comparison to the discovery paper (Aliu et al. 2013) resulting from the requirement of three telescopes in the reconstruction and a higher image intensity requirement, as well as the larger data set.

The morphology of 3FGL J2021.0+4031e was examined by producing a TS map of the region with 3FGL J2021.0+4031e removed from the model of the region (Figure 14). The *Fermi*-LAT emission showed a disk-like structure, of similar size to

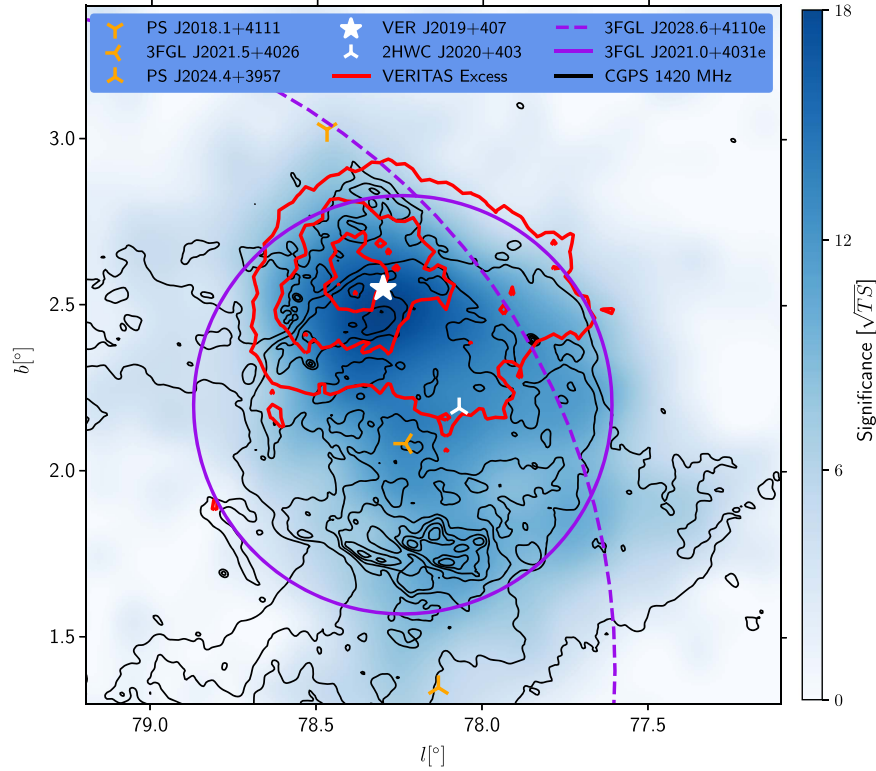


Figure 14. *Fermi*-LAT \sqrt{TS} map of 3FGL J2021.0+4031e (SNR G78.2+2.1). Overlaid are VERITAS excess contours at levels of 50, 100, 150, 200, and 250 (red) and CGPS 1420 MHz (black) contours in eight logarithmically spaced levels between brightness temperatures 20 and 150 K (Taylor et al. 2003). The locations of 2HWC J2020+403 (white three-pointed star) and the *Fermi*-LAT sources in the region (orange three-pointed stars for point sources, purple circles showing the extent for extended sources) are indicated as well.

the remnant detected in the CGPS 1420 MHz survey (Taylor et al. 2003). However, the HE γ -ray emission was not uniform across the disk; rather, it was enhanced at the northern rim, where the VERITAS emission is detected.

The spectral fit to the VERITAS data is given in Table 5, with the spectral points given in Table 9. The updated analysis has a spectrum that is softer, but within the statistical errors of the earlier spectrum reported in Aliu et al. (2013), with a normalization at 1000 GeV that is in agreement with the value in that work.

Two *Fermi*-LAT SEDs were produced for 3FGL J2021.0+4031e. The first uses the full disk of radius $0^\circ.63$ as in the 3FGL catalog. For the second, 3FGL J2021.0+4031e was broken up into two sources: the region inside the VERITAS *Extended* integration region (a disk of radius $0^\circ.23$ centered on $(l, b) = (78.38, 2.56)$, 3FGL J2021.0+4031eA) and the region from which the VERITAS spectrum presented in Table 5 is extracted, as well as the remainder of the $0^\circ.63$ radius disk outside of the VERITAS integration region, 3FGL J2021.0+4031eB. This was done to investigate whether the emission seen by VERITAS has a common origin with that observed with the *Fermi*-LAT. Also, it was used to test whether the level of enhancement seen in the *Fermi*-LAT TS map of the remnant is reflected in a change in the spectral properties. In both cases, the favored fit is a PL. When treated as a single disk, 3FGL J2021.0+4031e is detected at a TS of 910, with spectral parameters of $\gamma = 2.02 \pm 0.03_{\text{stat}}$, $N_0 = (2.50 \pm 0.10_{\text{stat}}) \times 10^{-13} \text{ GeV}^{-1} \text{ cm}^{-2} \text{ s}^{-1}$ at $E_0 = 6.78 \text{ GeV}$. When divided into two sources, they are detected at test statistics of 186 and 474 for 3FGL J2021.0+4031eA and 3FGL J2021.0+4031eB, respectively. 3FGL J2021.0+4031eA is fit with the parameters $\gamma = 2.00 \pm 0.07_{\text{stat}}$, $N_0 = (5.77 \pm 0.52_{\text{stat}}) \times$

$10^{-14} \text{ GeV}^{-1} \text{ cm}^{-2} \text{ s}^{-1}$ at $E_0 = 6.78 \text{ GeV}$, whereas 3FGL J2021.0+4031eB is fit by $\gamma = 2.02 \pm 0.04_{\text{stat}}$, $N_0 = (1.84 \pm 0.10_{\text{stat}}) \times 10^{-13} \text{ GeV}^{-1} \text{ cm}^{-2} \text{ s}^{-1}$ at $E_0 = 6.78 \text{ GeV}$. Figure 15 shows the SEDs for 3FGL J2021.0+4031e and 3FGL J2021.0+4031eA. 3FGL J2021.0+4031eB is not shown for clarity. All have the same spectral indices within statistical errors, which suggests that they share a common origin of their emission. A joint fit was conducted using the VERITAS and the *Fermi*-LAT spectral points for 3FGL J2021.0+4031eA with the PL, BPL, and LP spectral models. The best fit is with a BPL with parameters $N_0 = (1.93 \pm 0.50_{\text{stat}}) \times 10^{-14} \text{ GeV}^{-1} \text{ cm}^{-2} \text{ s}^{-1}$, $E_b = 405 \text{ GeV}$, $\gamma_1 = 1.97 \pm 0.07_{\text{stat}}$ and $\gamma_2 = 2.79 \pm 0.22_{\text{stat}}$, and p -value = 0.55 versus 0.33 for the LP and 0.11 for the PL.

6.2.3. Discussion

With a morphology that matches G78.2+2.1, the HE emission from 3FGL J2021.0+4031e is associated with the SNR. The agreement in the fluxes from 3FGL J2021.0+4031eA and VER J2019+407 suggests that these two objects are associated and thus that the VERITAS emission is also associated with G78.2+2.1, with the current VERITAS observations only able to detect the brightest part of the remnant. The peak of this emission is located $0^\circ.5$ away from the pulsar (PSR J2021+4026), with no evidence of VHE emission from the region between VER J2019+407 and the pulsar. Though the pulsar is often offset from the center of the VHE emission, it generally lies within the emission region and/or is associated with another region of VHE emission as discussed in Aliu et al. (2013) and references therein. The level of separation we have observed here,

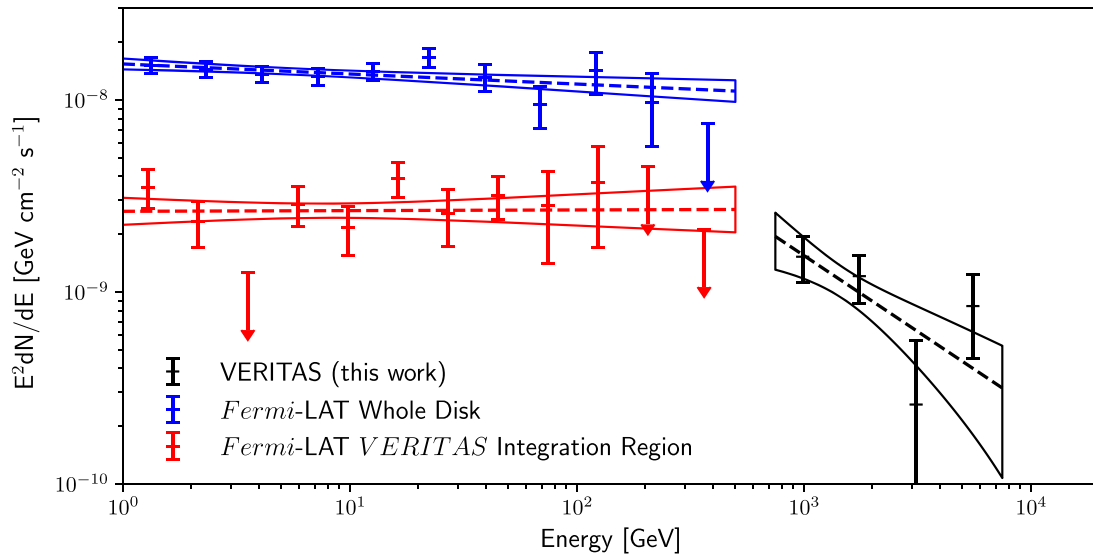


Figure 15. SEDs from sources in the region of the G78.2+2.1. Black is the VER J2019+407 spectrum from the VERITAS *Extended* analysis. Also plotted are the *Fermi*-LAT SEDs from 3FGL J2021.0+4031e (blue) and 3FGL J2021.0+4031eA, and the region of 3FGL J2021.0+4031e that lies within the VERITAS *Extended* integration region (red; 3FGL J2021.0+4031eB was also included in the analysis as an additional source whose spectrum is not shown for clarity). The butterflies show statistical errors only.

significantly more than the angular extent of the VHE emission, makes it unlikely that the emission is due to a PWN associated with PSR J2021+4026.

Comparing the joint spectral fit conducted in this work with that presented in Fraija & Araya (2016) shows a softer spectral index above and below the break (though within statistical errors), with a higher break energy. The softer spectral index in this work is in agreement with that predicted by standard test-particle shock acceleration, reducing the requirements for nonlinear effects as discussed in that work.

The source detected by HAWC is offset from the VERITAS emission and has a higher flux and a softer spectral index. The origin of these differences is uncertain; it may be due to the higher energy threshold of the HAWC observations, although there is no evidence of this in the VERITAS data. The other possibility is that the significant diffuse emission in the region is affecting the analyses. Further work is required to understand the emission in this region across all wave bands. Deeper VERITAS observations, in particular with the lower energy threshold following the 2012 camera upgrade, may enable the detection of emission from more of the remnant and the exploration of any energy-dependent morphology that could explain the differences between the three instruments.

6.3. VER J2019+368

6.3.1. Background

MGRO J2019+37, one of the brightest sources observed in VHE γ -rays, is located within the vicinity of the OB star association Cygnus OB1. This source was observed by the Milagro Collaboration to have a flux level of 80% of the Crab Nebula where it was fit with an exponentially cutoff power law (Equation (3)) of parameters $N_0 = (7^{+5}_{-2}) \times 10^{-17} \text{ GeV}^{-1} \text{ cm}^{-2} \text{ s}^{-1}$ at 10,000 GeV, $\gamma = 2.0^{+0.5}_{-1.0}$, and $E_c = 29000^{+50000}_{-16000} \text{ GeV}$ (Abdo et al. 2012), with no identified multiwavelength counterpart(s).

VERITAS has resolved MGRO J2019+37 into two components: an extended source VER J2019+368, which constitutes the bulk of the emission, and a point source VER J2016+371, which is coincident with the SNR CTB 87 (Aliu et al. 2014b) and discussed in Section 6.4.

VER J2019+368, with an extent of over 1° along the major axis, is spatially close to several sources that could potentially power (at least part of) the VHE emission. These include the H II region Sh 2-104, Wolf-Rayet stars, the pulsars PSR J2021+3651 and PSR J2017+3625, (which are both detected in HE γ -rays by the *Fermi*-LAT), the PWN G75.1+0.2 (powered by PSR J2021+3651), and the hard X-ray transient IGR J20188+3657 (Aliu et al. 2014b).

PSR J2021+3651 (3FGL J2021.1+3651) lies to the east of the VER J2019+368 region and is associated with the X-ray PWN G75.2+0.1, which stretches back toward the VHE emission region. The possibility of these objects being linked to MGRO J2019+37 is discussed in detail in Hou et al. (2014).

Gottlieb et al. (2016) report on *NuSTAR* observations of the western edge of the VER J2019+368 region. They identified a number of hard X-ray sources in the region; three sources of particular interest were identified: 3XMM J201744.7+365045 (a bright point source that is most likely an active galactic nucleus behind the Galactic plane, though it could be a pulsar), *NuSTAR* J201744.3+364812 (a nebula, most likely a galaxy cluster hidden behind the Galactic plane), and emission associated with a young massive stellar cluster enclosed by a radio spur at the eastern edge of Sh 2-104. Further observations, for example, with *Chandra*, are required to determine whether these sources are related to the observed emission.

3FGL J2017.9+3627 lies to the southwest of VER J2019+368 and was recently identified as a γ -ray pulsar (PSR J2017+3625) by the Einstein@Home distributed computing project (Pletsch & Clark 2014; Clark et al. 2017). The pulsar has a spin frequency of 6.00 Hz with a first frequency derivative of $-4.89 \times 10^{-14} \text{ Hz s}^{-1}$, giving a characteristic age of 1943 kyr and a spin-down power of $1.2 \times 10^{34} \text{ erg s}^{-1}$ (Clark et al. 2017).

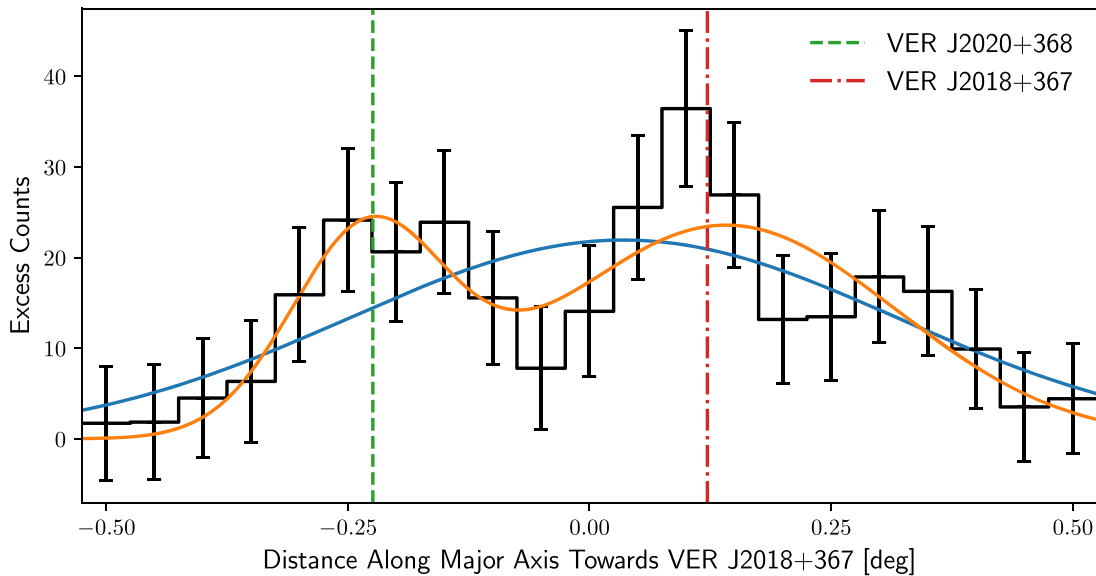


Figure 16. Section along the major axis of VER J2019+368 toward VER J2018+367* through the excess map using the *Point* integration radius (black steps). Each bin was produced using an aperture of width $0^{\circ}05$ and height $0^{\circ}2$. The data are fit with a single Gaussian (blue) and the sum of two Gaussians (orange). The locations of VER J2018+367* (red dot-dashed) and VER J2020+368* (green dashed) are also shown.

3FGL J2017.9+3627 is coincident with a region of low-energy VHE γ -ray emission ($E < 1$ TeV; Aliu et al. 2014b). Gotthelf et al. (2016) concluded that this pulsar could power the observed emission with an observed efficiency (L_{TeV}/\dot{E}) ~ 0.03 , which is plausible for a $>10^5$ yr old pulsar.

6.3.2. Results

In this analysis, VER J2019+368 was observed at a peak (local) significance of 10.3σ using the *Extended* integration region. Significantly extended and asymmetrical, the source is best fit with an asymmetric Gaussian (Table 4) as in Aliu et al. (2014b), with the fit parameters in agreement with the results presented there.

In addition, a sky map produced using the *Point* integration region shows that the emission appears to be strongest in two regions, each of which is detected at a level greater than $7\sigma_{\text{local}}$. Between the two sources lies a valley in the significance where the significance drops below $4\sigma_{\text{local}}$, giving a change in the significance that is greater than $3\sigma_{\text{local}}$. This suggests that the emission may be the result of two sources that were previously unresolved (though whether these are two independent sources, two enhancements of a single, extended source, or the result of statistical fluctuations is, as yet, uncertain).

To examine the extension of these two regions, a joint fit was conducted using two symmetric Gaussian sources (Table 4). This did not produce a significant improvement in the fit in comparison to a single, asymmetric Gaussian model ($\chi^2/\text{dof} = 6511/5992$ for the two sources versus $6600/5994$ for the single, asymmetric Gaussian). We also produced a section through the excess map along the major axis of the fit to VER J2019+368 (Figure 16). The data were binned using rectangles of width $0^{\circ}05$ and height $0^{\circ}2$ along a length of $1^{\circ}0$. This was fit with two models: a single Gaussian function and the sum of two Gaussian functions. The single Gaussian function fits the data well, with a χ^2/dof of $15.1/17$, and the sum of two Gaussian functions mildly overfits the data, with a χ^2/dof of $8.2/14$. Neither of these tests provides statistically significant evidence that the emission is due to two independent sources; therefore, we name the potential sources VER J2018+367* and VER J2020+368*, where the * indicates that the two sources are still

candidates and may be related. Further observations are required to understand this morphology.

Aliu et al. (2014b) reported evidence of energy-dependent morphology with a low-significance (3σ) region of lower-energy ($E < 1000$ GeV) emission to the southwest of the main emission region around $(\alpha_{J2000}, \delta_{J2000}) = (20^{\text{h}}18^{\text{m}}, +36^{\circ}26')$. This is not visible in this analysis with either the *Point* or *Extended* integration regions (Figure 17). The reason for this is due to either the higher energy threshold used in this analysis or the fact that the original apparent energy dependence was a statistical fluctuation that has disappeared with additional data. Further observations with a lower energy threshold following the 2012 camera upgrade may clarify this. Interestingly, both VER J2018+367* and VER J2020+368* are also regions that show low-energy emission in Figure 17. However, at the moment, it is not possible to say whether this is the cause of these excesses (regions of lower-energy emission over a background of higher-energy emission) or whether this is just an effect of having brighter emission from these regions across both energy ranges.

We reconstructed spectra for all three sources, with the fit parameters given in Table 5, the spectral points given in Tables 10–12, and both shown in Figure 18. In the case of VER J2019+368 there is some evidence of curvature. When fit with an LP spectrum, the fit improved in comparison to the PL spectrum that we report in Table 5, but not significantly (F -test = 1.75σ). In comparison with the result presented in Aliu et al. (2014b), the spectrum has a significantly lower flux. This is due to the smaller integration region used in this analysis ($0^{\circ}23$ radius rather than $0^{\circ}5$).

6.3.3. Discussion

2HWC J2019+367 lies between VER J2018+367* and VER J2020+368*, $0^{\circ}07$ away from VER J2019+368 (within the $0^{\circ}09$ statistical uncertainty of the HAWC location). As a point source (it was also detected with an extension of $0^{\circ}7$), it is fit with a softer spectral index ($-2.29 \pm 0.06_{\text{stat}}$) and a higher normalization $((3.02 \pm 0.31_{\text{stat}}) \times 10^{-17} \text{ GeV}^{-1} \text{ cm}^{-2} \text{ s}^{-1}$ at 7000 GeV) than observed for VER J2019+368 in this work ($\gamma = 1.98 \pm 0.09_{\text{stat}} \pm 0.20_{\text{sys}}$, $N_0 = (1.03 \pm 0.11_{\text{stat}} \pm 0.2_{\text{sys}})$

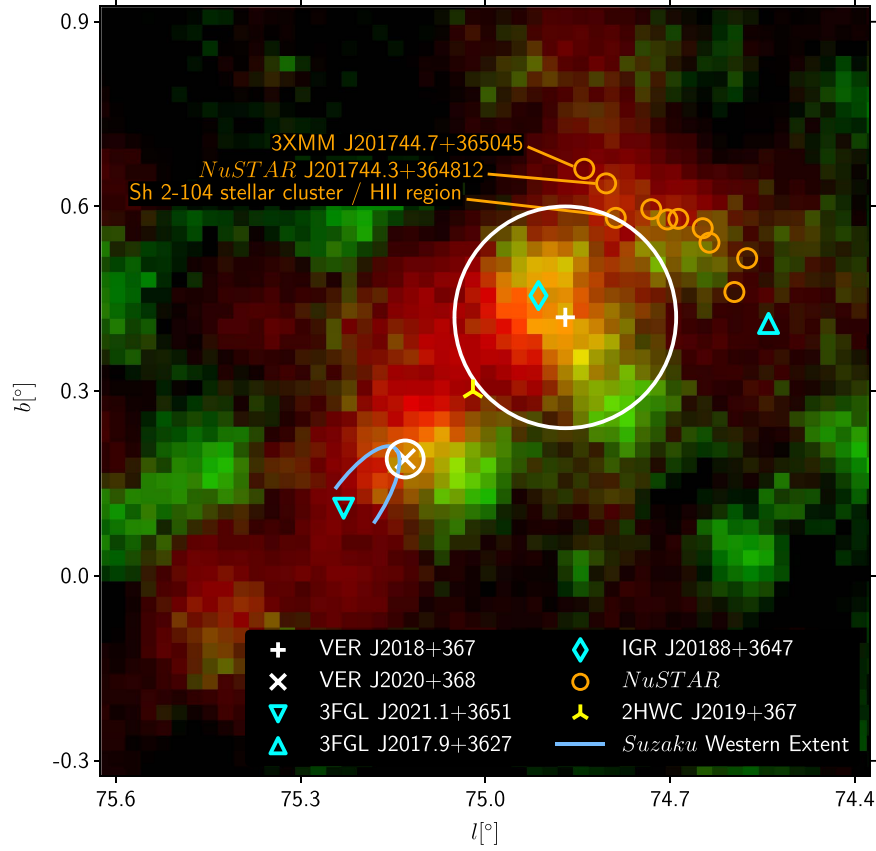


Figure 17. Energy-dependent excess map at >1000 GeV (red) and <1000 GeV (green) for the region around VER J2019+368 produced using the *Point* integration region; the transition from black to color is an excess ≥ 0 with a maximum excess >1000 GeV of 70 counts and a maximum excess <1000 GeV of 30 counts. Unlike in Aliu et al. (2014b), there is no evidence of a region of lower-energy emission to the south of the extended emission from VER J2019+368. Either this is due to the higher energy threshold employed in this analysis, reducing the sensitivity to low-energy emission in this region, or the earlier result was a statistical fluctuation that has diminished with the increased data. VER J2018+367* and VER J2020+368* are shown with the 1σ extents (solid white lines) and are located at regions that show enhanced emission below 1000 GeV. Also shown are the locations of 2HWC J2019+367 (yellow), IGR J20188+3647 (cyan diamond), the two *Fermi*-LAT pulsars (3FGL J2021.1+3651 and 3FGL J2017.9+3627; cyan triangles), and the *NuSTAR* sources from Gotthelf et al. (2016). The sky-blue arc approximately traces the region with >50 photons $\text{s}^{-1} \text{cm}^{-2} \text{sr}^{-1}$ in the 2–10 keV energy range from Mizuno et al. (2017).

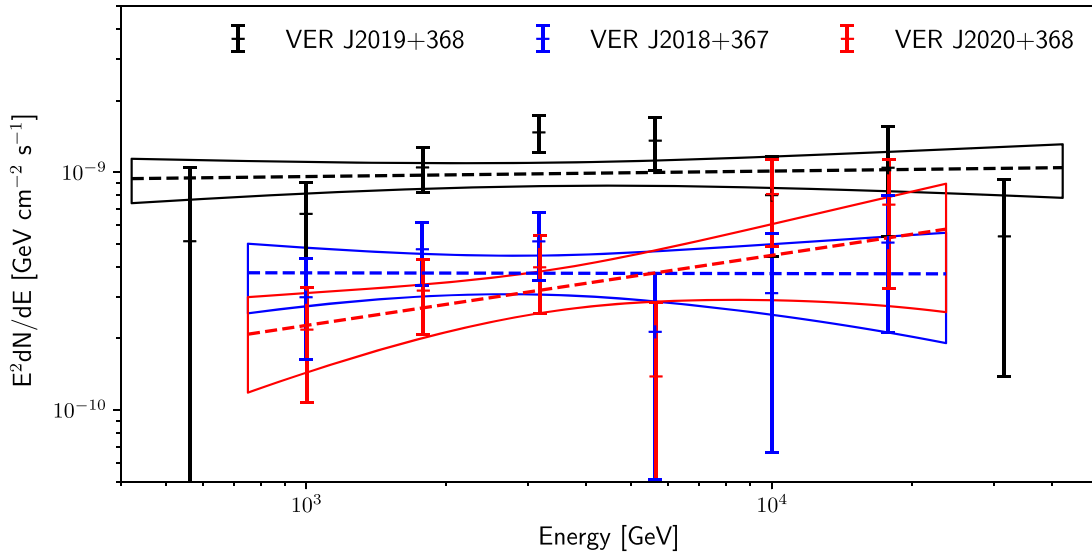


Figure 18. Spectra of VERITAS sources in the MGRO J2019+37 region. The spectrum for VER J2019+368 was produced using the *Extended* integration region and is shown in black, along with the spectra for VER J2018+367* (blue) and VER J2020+368* (red), which were produced using the *Point* integration region. The butterflies show statistical errors only.

$\times 10^{-16} \text{ GeV}^{-1} \text{ cm}^{-2} \text{ s}^{-1}$ at 3110 GeV). It is noted that VER J2016+371 is not resolved in the 2HWC catalog, though there is evidence of excess emission in that direction in the maps presented in the associated paper. Examining a *Fermi*-LAT TS map, there is no evidence of emission coming from either of the two sources.

6.3.4. Potential VER J2018+367* Multiwavelength Counterparts

3FGL J2017.9+3627 has recently been identified as a γ -ray pulsar (PSR J2017+3625) by the Einstein@Home distributed computing project (Clark et al. 2017) and lies to the southwest of VER J2018+367* at a distance of $0^\circ.34$. As pulsations have only recently been detected, no publicly available ephemeris is available. This prevented us from using either of the analysis methods presented in Section 3 for determining whether a PWN is present but hidden by the strength of the pulsed emission. Instead, we performed an analysis above 10 GeV to test for any emission potentially associated with a PWN; none was detected, and we place a 95% integral flux upper limit on the point-source emission of $6.2 \times 10^{-11} \text{ cm}^{-2} \text{ s}^{-1}$ between 10 and 500 GeV. We can compare the observed separation of PSR J2017+3625 divided by the extension of VER J2018+367* with the values reported in H.E.S.S. Collaboration et al. (2018b). The observed value of 1.9 is approximately a factor of 2 higher than all of the firm associations reported and above the rating criterion of 1.5 they applied to post-select associations. However, with a characteristic age of 1943 kyr, this is significantly older than all of the firm identification that they report and could explain the larger ratio. Assuming a distance of 450 pc (from Gotthelf et al. 2016 based on the gamma-ray efficiency of the pulsar), the TeV efficiency is 0.003, right at the lower edge of the scatter predicted by their varied model. In contrast, assuming a larger distance (Gotthelf et al. 2016 place a lower limit on the distance using an empirical relationship between pulsars and their spin-down power at 1 kpc) gives a TeV efficiency of greater than 0.01, well within the expected range. Given the large separation and lack of evidence of an extended PWN in multiwavelength observations, we are not able to associate the two objects. However, based on the observed properties of younger systems, it is possible that VER J2018+367* is a PWN associated with PSR J2017+3625.

In addition to PSR J2017+3625, other nonthermal sources are detected in the area that may power the observed VHE emission. Gotthelf et al. (2016) discuss the potential for a number of hard X-ray sources identified using *NuSTAR* data to power at least the western part of the emission from VER J2019+368, the emission that is now associated with VER J2018+367*. We note that all of the identified sources lie to the west of VER J2018+367* and thus are unlikely to be the sole contributor to the emission.

Observations with *Suzaku* presented in Mizuno et al. (2017) showed no evidence of X-ray emission in the 0.7–10 keV energy range in the region around VER J2018+367*. The closest source, a point source that they suspect is a background active galactic nucleus, lies in the gap between VER J2018+367* and VER J2020+368* and is unlikely to be the dominant contributor to the observed, extended VHE emission.

VER J2018+367* is spatially coincident with IGR J20188+3647, which remains a possible source for the emission from this region. Based on the fast rise time of the emission from IGR J20188+3647 (~ 10 minutes), followed by the slower decay (~ 50 minutes) and the spectral parameters,

Sguera (2009) consider this to be a candidate supergiant fast X-ray transient. They concluded that though it is spatially coincident with MGRO J2019+37, due to the extended and diffuse nature of the VHE emission region, it is unlikely to be associated with it. However, the resolution of VER J2019+368 into two sources has significantly reduced this constraint.

6.3.5. Potential VER J2020+368* Multiwavelength Counterparts

3FGL J2021.1+3651 (PSR J2021+3651) is a γ -ray pulsar that lies $0^\circ.11$ away from VER J2020+368*. The spectrum cuts off sharply at a few tens of GeV ($E_c = 5.14 \pm 0.36 \text{ GeV}$), and thus it is not expected to contribute to the observed VHE emission, but it could be masking emission associated with a PWN. Using the methods outlined in Section 3, an examination was conducted for a possible counterpart using an OFF-pulse phase of 0.7 to 1. The BRIDGE pulse phase from 0.2 to 0.4 was included in the ON-pulse phase. No evidence of a source was present in either of the analyses. The lack of detection of a *Fermi*-LAT PWN does not rule out the presence of such an object given the analysis challenges associated with such a bright pulsar, nor does it prevent the known PWN visible in other wavelengths from being responsible at least in part for the VHE emission.

XMM-Newton clearly shows a bright point source spatially coincident with the *Fermi*-LAT detected pulsar PSR J2021.1+3651, with associated extended emission likely from a PWN (G75.2+0.1) powered by the pulsar. The PWN is also visible in VLA 20 cm data. Aliu et al. (2014b) discuss the potential for G75.2+0.1 to contribute to the VHE emission in detail. The authors note that the bulk of VERITAS emission lies to the west of these objects, though the pulsar is moving in an eastward direction with G75.2+0.1 stretching back toward VER J2020+368*. Mizuno et al. (2017) reported on *Suzaku* observations that have allowed for a more detailed study of this westerly emission from G75.2+0.1 in the 0.7–2 and 2–10 keV bands. They show significant emission that extends to the west of PSR J2021+3651 back toward VER J2020+368*, though, as in the earlier observations, the X-ray emission they observe does not cover the region of highest VHE emission. Comparing the X-ray and VHE emission, they explore the relationship between the earlier results on VER J2019+368 presented by VERITAS in Aliu et al. (2014b) and the X-ray data they studied. The results presented here show a similar spectral index for VER J2020+368* as for the results reported for VER J2019+368 in Aliu et al. (2014b) ($-1.71 \pm 0.26_{\text{stat}} \pm 0.2_{\text{sys}}$ versus $-1.75 \pm 0.08_{\text{stat}} \pm 0.2_{\text{sys}}$), though the 1–10 TeV flux is approximately a factor of six lower ($7.3 \times 10^{-10} \text{ GeV cm}^{-2} \text{ s}^{-1}$ rather than $4.2 \times 10^{-9} \text{ GeV cm}^{-2} \text{ s}^{-1}$). This is due to the smaller integration region size used ($0^\circ.1$ versus $0^\circ.5$), but with an area that is 25 times smaller, the flux per unit solid angle is higher. The significant decrease in the TeV flux results in an increase in the ratio $U_{\text{mag}}/U_{\text{ph}}$ from about 1, as presented in Mizuno et al. (2017), to about 6, with the smaller integration region better matching the size of the region from which the X-ray flux was extracted. This change results in a larger average magnetic B field of about 18 μG . This implies a lower energy population of electrons powering the observed X-ray emission (by a factor of about $\sqrt{6}$), bringing them down to about the same energy as those powering the VERITAS emission. Thus, the difference in the spectral indices between the X-ray and γ -ray observations cannot be explained by a break in the electron spectrum. The similarities between the populations also make it difficult to explain the

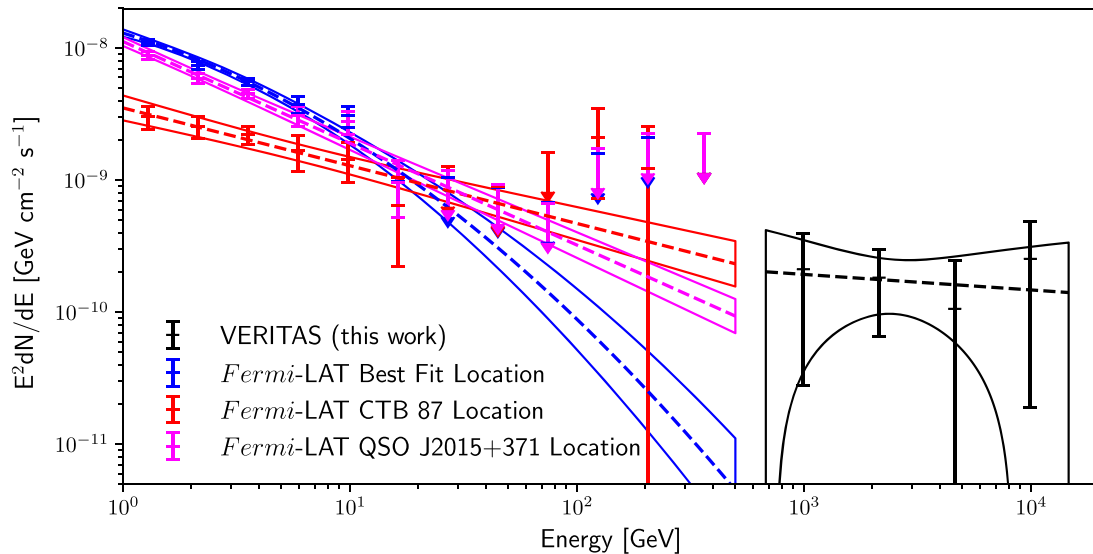


Figure 19. Spectra of sources in the CTB 87 region. The VERITAS spectrum for VER J2016+371 (black) is plotted along with the *Fermi*-LAT spectra derived from a single source located at the position of 3FGL J2015.6+3709 (blue). The spectra from an analysis where this was replaced with two sources, one located at the radio position of CTB 87 (red) and one located at the radio position of QSO J2015+371 (magenta), are also shown. The butterflies show statistical errors only.

origins of the observed morphology differences between the two wave bands. This higher magnetic field is closer to that detected in HESS J1825-137 (Uchiyama et al. 2009), though VER J2020+368* has a much smaller difference between the X-ray and γ -ray spectral indices. In summary, it is likely that VER J2020+368* is associated with G75.2+0.1 (the PWN of PSR J2021+3651), though more detailed observations are required to fully understand the system, in particular to understand the relationship between the observed properties of the X-ray and γ -ray emission and the high inferred magnetic field.

6.4. VER J2016+371

6.4.1. Background

In addition to the extended emission from VER J2019+368, Aliu et al. (2014b) resolved from MGRO J2019+37 a point source of emission coincident with the SNR CTB 87 (VER J2016+371). There is a bright source detected by *Fermi*-LAT that lies close to the position of VER J2016+371 in the 1FGL, 2FGL, and 3FGL catalogs (1FGL J2015.7+3708, 2FGL J2015.6+3709, and 3FGL J2015.6+3709, respectively) and also in the higher-energy 1FHL, 2FHL, and 3FHL catalogs (1FHL J2015.8+3710, 2FHL J2016.2+3713, 3FHL J2015.9+3712) and in the 1st *Fermi*-LAT Supernova Remnant Catalog (1SC; Acero et al. 2016). The location of this source is slightly different in each of the three energy ranges. In the 1FGL/2FGL/3FGL catalogs the source is located close to QSO J2015+371, a BL Lacertae object at $z = 0.859$ (Shaw et al. 2013), whereas in the 1FHL/2FHL/3FHL catalogs it lies closer to CTB 87. At the lower energies of the 1/2/3 FGL catalog analysis, there is evidence of flux variability, which has, along with the location, led to the source being associated with the blazar QSO J2015+371. The higher energies see reduced evidence of variability and also see a hardening of the spectral index from -2.53 ± 0.04 in the 3FGL to -1.74 ± 0.46 in the 2FHL. Combined with the change in the source location, this has led to it being associated with CTB 87 in those catalogs. This suggests that there could be two HE γ -ray sources that lie close together and are not being resolved in the *Fermi*-LAT data.

6.4.2. Results

In this analysis, VER J2016+371 was observed using the ring background technique and the *Point* integration region at a level of $6.3\sigma_{\text{local}}$. Previously reported as a point source (Aliu et al. 2014b), we found no improvement when fitting with a single symmetric Gaussian. Thus, we still consider it to be a point source. To identify its best-fit location, we modeled it as a point source, and the best-fit location is given in Table 4.

A spectral fit was conducted using all of the data taken with four telescopes operational and with a pointing offset of less than two degrees (a looser cut on pointing than used for the other sources, since the majority of the observations that had the source in the FOV were targeted at VER J2019+368 and thus have a larger pointing offset). A SED was produced using three logarithmically spaced bins per decade in energy and the *Point* integration region (Figure 19, Tables 5 and 13). The updated spectrum is consistent (within statistical errors) with that reported in Aliu et al. (2014b).

In the *Fermi*-LAT analysis, when the source is fit at the location of 3FGL J2015.6+3709 ($(l, b) = (74^\circ 87', 1^\circ 186'')$), an additional source is detected at $(l, b) = (74^\circ 99', 1^\circ 16'')$ (see Table 6 for details). The location of the *Fermi*-LAT source is known to vary depending on the energy threshold, so this additional source is likely due to a change in the source location associated with the higher energy threshold in this analysis in comparison to the 3FGL. The *fermipy* method *localize* was run on 3FGL J2015.6+3709 without the additional point source included in the model. This resulted in an updated source position of $(l, b) = (74.893^\circ \pm 0.006^\circ_{\text{stat}}, 1.200^\circ \pm 0.004^\circ_{\text{stat}})$. This position lies $0^\circ 03'$ from the catalog location of 3FGL J2015.6+3709 and is shown relative to the *Fermi*-LAT catalog positions and overlaid on an *XMM-Newton* counts map with VERITAS excess and CGPS 1420 MHz contours in Figure 20. With the updated source location, no second source is detected. For the updated location, the *fermipy* method *extension* was run to determine whether there was any evidence of spatial extension; none was detected, and a 95% confidence level upper limit of extension was found of $0^\circ 07'$ with a 2D symmetrical Gaussian as the source template. Given

Table 6
Results of an Examination of the HE Emission in the Region of VER J2016+371

Model	TS	α_{J2000} (deg)	δ_{J2000} (deg)	l (deg)	b (deg)	N_0 (GeV $^{-1}$ cm $^{-2}$ s $^{-1}$)	E_0/E_b (GeV)	γ	β
Single source	3FGL location	1888	303.91	37.16	74.86	$(4.43 \pm 0.18)\text{E-12}$	1520	2.62 ± 0.09	0.12 ± 0.06
Single source	Best-fit location	1964	303.91	37.19	74.893 ± 0.006	$(4.86 \pm 0.17)\text{E-12}$	1520	2.63 ± 0.07	0.02 ± 0.04
Two sources	3FGL J2015.6+3709	1363	303.91	37.16	74.86	$(4.43 \pm 0.18)\text{E-12}$	1520	2.62 ± 0.09	0.12 ± 0.06
	New source	59.8	304.02	37.25	74.99	$(1.19 \pm 0.34)\text{E-12}$	1000	2.11 ± 0.12	N/A
Two sources	CTB 87	102	304.01	37.21	74.95	$(3.53 \pm 0.86)\text{E-12}$	1000	2.44 ± 0.10	N/A
	QSO	1087	303.87	37.18	74.87	$(1.13 \pm 0.09)\text{E-11}$	1000	2.77 ± 0.06	N/A
	J2015+371								

Note. All errors are statistical only.

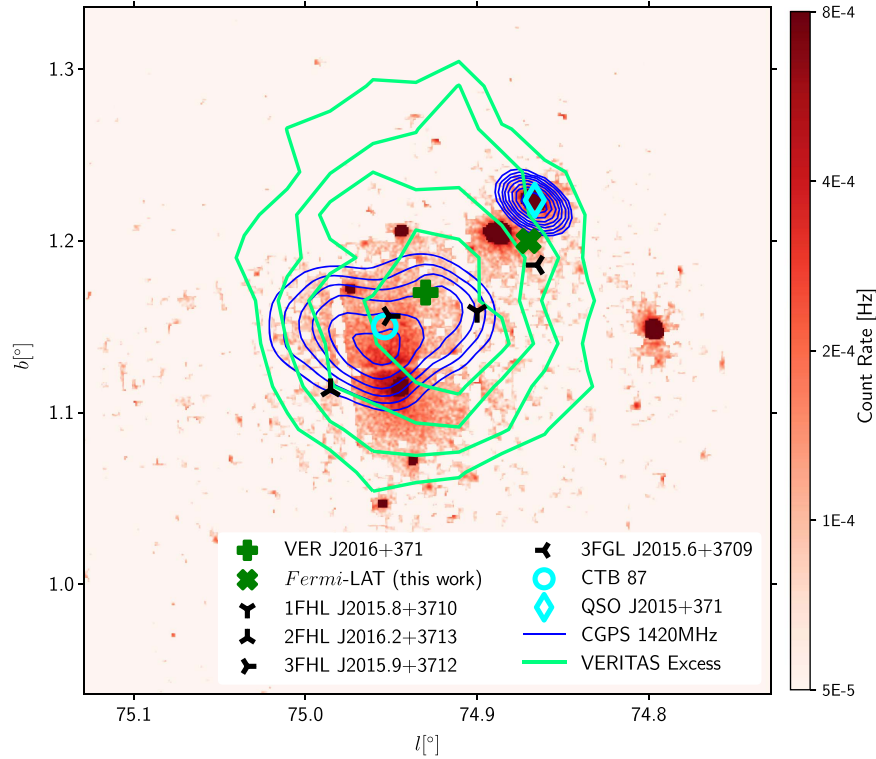


Figure 20. *XMM-Newton* counts (red color scale, Obs. ID 0744640101, no background subtraction or correction for variation in exposure across the FOV has been applied). VERITAS excess with the *Point* integration region is shown in levels of 10 counts starting at 30 (bright green) along with CGPS 1420 MHz contours (eight logarithmically spaced levels between brightness temperatures 20 and 150 K [Taylor et al. 2003], dark blue). The locations of VER J2016+371 (green plus sign), the *Fermi*-LAT position from this work (green cross), and the positions from the different catalogs (black three-pointed stars) and the radio locations of CTB 87 (cyan circle) and QSO J2015+371 (cyan diamond) are shown for comparison.

the location of the source, it is likely dominated by emission from QSO J2015+371, and the SED (Figure 19) is consistent with that from 3FGL J2015.6+3709 as presented in the 3FGL (shown in Figure 7).

To test the relative contributions of the two associations, instead of using a single source to model the emission, two power-law sources were used and placed at the radio locations of CTB 87 and QSO J2015+371, respectively (the positions are given in Table 6). When this model was fit to the data, the two sources had test statistics of 102 and 1087 for CTB 87 and QSO J2015+371, respectively. It is not possible to definitively state that the *Fermi*-LAT data support the presence of two sources that are currently unresolved, but there is evidence to suggest that this is the case.

The spectra of the two sources are noticeably different, with the source located at the site of CTB 87 being weaker and harder. Plotting these spectra with the spectrum from the updated 3FGL location and with the VERITAS spectrum of VER J2016+371 (Figure 19) shows good agreement between the spectrum of the *Fermi*-LAT source located at CTB 87 and the spectrum of VER J2016+371, whereas the source located at the location of QSO J2015+371 would require a spectral hardening to fit the VERITAS results. Conducting a joint fit to both the spectral points from the *Fermi*-LAT emission at the CTB 87 position and VERITAS emission from VER J2016+371 with a PL gives the parameters $N_0 = (6.67 \pm 0.60_{\text{stat}}) \times 10^{-11}$ GeV $^{-1}$ cm $^{-2}$ s $^{-1}$ at $E_0 = 5.2$ GeV and spectral index $-2.39 \pm 0.05_{\text{stat}}$ with a χ^2 of 4.4 and 9 dof.

Table 7
Catalog Values for the 3FGL Sources in the Survey Region ($(83^\circ 5' > l > 65^\circ 5')$ and $(5^\circ 5' > b > -2^\circ 5')$) that Were Not Significantly Detected in This Analysis ($TS < 25$) and Removed

Name	Spectrum Type	3FGL Sig. (σ)	N_0 ($\text{GeV}^{-1}\text{cm}^{-2}\text{s}^{-1}$)	E_0/E_b (GeV)	γ	β
3FGL J1958.6+3844	Power law	4.84	$(1.63 \pm 0.31_{\text{stat}})\text{E}-9$	0.8	$2.64 \pm 0.13_{\text{stat}}$	N/A
3FGL J2011.1+4203	Power law	4.31	$(1.23 \pm 0.25_{\text{stat}})\text{E}-9$	0.95	$2.54 \pm 0.12_{\text{stat}}$	N/A
3FGL J2014.4+3606	Power law	4.48	$(4.49 \pm 0.94_{\text{stat}})\text{E}-10$	1.69	$2.40 \pm 0.11_{\text{stat}}$	N/A
3FGL J2024.6+3747	Log parabola	7.04	$(6.30 \pm 0.87_{\text{stat}})\text{E}-9$	0.87	$2.39 \pm 0.58_{\text{stat}}$	$0.49 \pm 0.22_{\text{stat}}$
3FGL J2026.8+4003	Log parabola	9.03	$(2.00 \pm 0.21_{\text{stat}})\text{E}-8$	0.7	$2.61 \pm 0.19_{\text{stat}}$	1
3FGL J2033.3+4348*	Power law	4.39	$(6.57 \pm 1.52_{\text{stat}})\text{E}-11$	3.84	$2.24 \pm 0.14_{\text{stat}}$	N/A
3FGL J2036.8+4234*	Power law	5.38	$(1.52 \pm 0.29_{\text{stat}})\text{E}-10$	3.21	$2.25 \pm 0.10_{\text{stat}}$	N/A
3FGL J2037.4+4132*	Power law	6.45	$(9.67 \pm 1.66_{\text{stat}})\text{E}-11$	4.17	$2.18 \pm 0.11_{\text{stat}}$	N/A
3FGL J2043.1+4350	Log parabola	8.41	$(3.32 \pm 0.38_{\text{stat}})\text{E}-8$	0.47	$2.46 \pm 0.19_{\text{stat}}$	1

Note. The asterisk denotes that the source lies in the field of the Cygnus Cocoon.

Table 8
VERITAS Spectral Points for VER J2031+415 Fit with a Power Law (Equation (1))

Energy Low (GeV)	Energy High (GeV)	Flux ($\text{GeV}^{-1}\text{cm}^{-2}\text{s}^{-1}$)	Flux Error ($\text{GeV}^{-1}\text{cm}^{-2}\text{s}^{-1}$)
422	750	$3.26\text{E}-15$	$1.57\text{E}-15$
750	1330	$6.85\text{E}-16$	$2.73\text{E}-16$
1330	2370	$1.97\text{E}-16$	$8.26\text{E}-17$
2370	4220	$3.95\text{E}-17$	$2.75\text{E}-17$
4220	7500	$3.62\text{E}-17$	$1.24\text{E}-17$
7500	13,300	$6.92\text{E}-18$	<i>Upper limit</i>
13,300	23,700	$1.26\text{E}-18$	$1.38\text{E}-18$
23,700	42,200	$5.99\text{E}-19$	$4.55\text{E}-19$

Table 9
VERITAS Spectral Points for VER J2019+407 Fit with a Power Law (Equation (1))

Energy Low (GeV)	Energy High (GeV)	Flux ($\text{GeV}^{-1}\text{cm}^{-2}\text{s}^{-1}$)	Flux Error ($\text{GeV}^{-1}\text{cm}^{-2}\text{s}^{-1}$)
750	1330	$1.56\text{E}-15$	$4.17\text{E}-16$
1330	2370	$3.91\text{E}-16$	$1.09\text{E}-16$
2370	4220	$2.65\text{E}-17$	$3.03\text{E}-17$
4220	7500	$2.73\text{E}-17$	$1.27\text{E}-17$

Table 10
VERITAS Spectral Points for VER J2019+368 Fit with a Power Law (Equation (1))

Energy Low (GeV)	Energy High (GeV)	Flux ($\text{GeV}^{-1}\text{cm}^{-2}\text{s}^{-1}$)	Flux Error ($\text{GeV}^{-1}\text{cm}^{-2}\text{s}^{-1}$)
422	750	$1.62\text{E}-15$	$1.68\text{E}-15$
750	1330	$6.68\text{E}-16$	$2.34\text{E}-16$
1330	2370	$3.31\text{E}-16$	$7.2\text{E}-17$
2370	4220	$1.47\text{E}-16$	$2.64\text{E}-17$
4220	7500	$4.29\text{E}-17$	$1.09\text{E}-17$
7500	13,300	$8.01\text{E}-18$	$3.59\text{E}-18$
13,300	23,700	$3.3\text{E}-18$	$1.6\text{E}-18$
23,700	42,200	$5.37\text{E}-19$	$3.99\text{E}-19$

6.4.3. Discussion

Combined, the location of VER J2016+371 and the spectrum of the *Fermi*-LAT emission, when fit as two sources, suggest that the *Fermi* emission from the direction of CTB 87

Table 11
VERITAS Spectral Points for VER J2018+367* Fit with a Power Law (Equation (1))

Energy Low (GeV)	Energy High (GeV)	Flux ($\text{GeV}^{-1}\text{cm}^{-2}\text{s}^{-1}$)	Flux Error ($\text{GeV}^{-1}\text{cm}^{-2}\text{s}^{-1}$)
750	1330	$2.98\text{E}-16$	$1.35\text{E}-16$
1330	2370	$1.5\text{E}-16$	$4.41\text{E}-17$
2370	4220	$5.12\text{E}-17$	$1.63\text{E}-17$
4220	7500	$6.74\text{E}-18$	$5.12\text{E}-18$
7500	13,300	$3.1\text{E}-18$	$2.44\text{E}-18$
13,300	23,700	$1.6\text{E}-18$	$9.33\text{E}-19$

Table 12
VERITAS Spectral Points for VER J2020+368* Fit with a Power Law (Equation (1))

Energy Low (GeV)	Energy High (GeV)	Flux ($\text{GeV}^{-1}\text{cm}^{-2}\text{s}^{-1}$)	Flux Error ($\text{GeV}^{-1}\text{cm}^{-2}\text{s}^{-1}$)
750	1330	$2.16\text{E}-16$	$1.09\text{E}-16$
1330	2370	$9.96\text{E}-17$	$3.48\text{E}-17$
2370	4220	$3.95\text{E}-17$	$1.43\text{E}-17$
4220	7500	$4.34\text{E}-18$	$4.53\text{E}-18$
7500	13,300	$8.03\text{E}-18$	$3.22\text{E}-18$
13,300	23,700	$2.29\text{E}-18$	$1.27\text{E}-18$

Table 13
VERITAS Spectral Points for VER J2016+371 Fit with a Power Law (Equation (1))

Energy Low (GeV)	Energy High (GeV)	Flux ($\text{GeV}^{-1}\text{cm}^{-2}\text{s}^{-1}$)	Flux Error ($\text{GeV}^{-1}\text{cm}^{-2}\text{s}^{-1}$)
681	1470	$2.13\text{E}-16$	$1.85\text{E}-16$
1470	3160	$3.96\text{E}-17$	$2.53\text{E}-17$
3160	6810	$4.95\text{E}-18$	$6.48\text{E}-18$
6810	14,700	$2.55\text{E}-18$	$2.36\text{E}-18$

and VER J2016+371 are the same source and that they are associated with the SNR CTB 87. However, a contribution from QSO J2015+371 to the VHE emission cannot be ruled out.

Examining the region in other wavelengths highlights the two sources identified above, along with a number of other, weaker, nonthermal sources. Figure 20 shows an

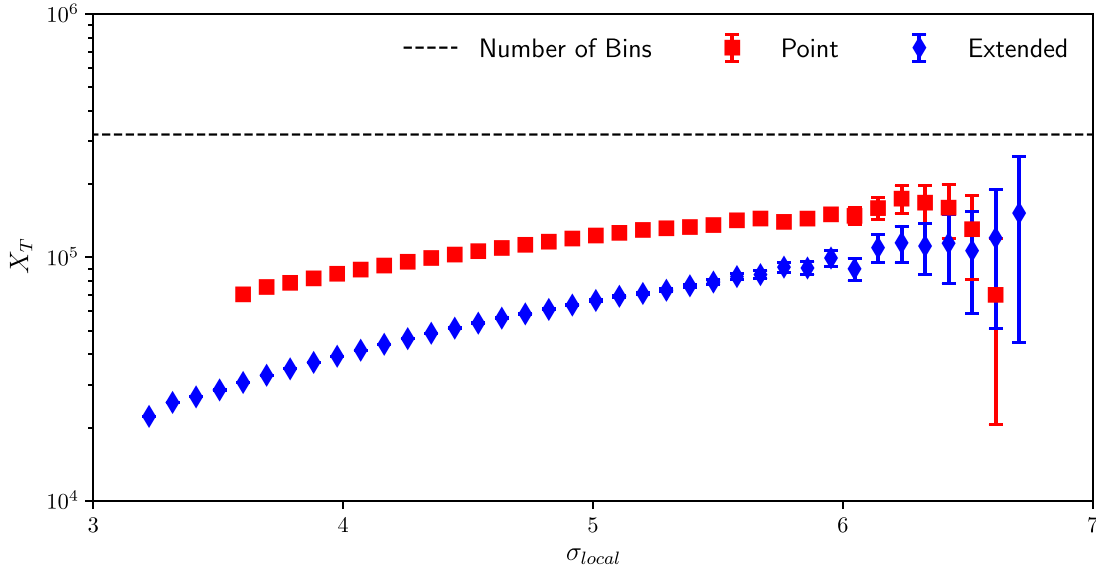


Figure 21. Trial factor, X_T , as a function of local significance, σ_{local} . The black dashed line presents the total number of bins in the sky map of the whole Cygnus region observed with VERITAS. At low σ , $P(\sigma_{\text{global}} > \sigma)$ approaches 1; thus, Equation (12) has no solution.

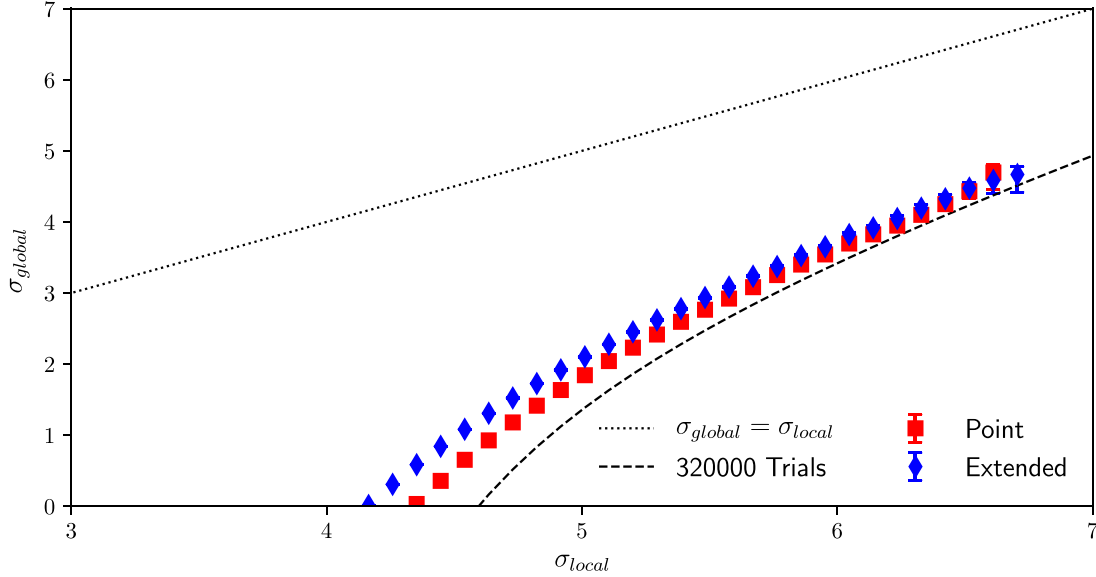


Figure 22. Global (σ_{global}) vs. local (σ_{local}) significance for the sky survey region. Below $\sigma_{\text{local}} \approx 4.5$ the global significance is zero, i.e., a fluctuation of this magnitude is expected every observation.

XMM-Newton counts map of the region (Obs. ID 0744640101) overlaid with contours from the CGPS 1420 MHz survey. In both of these observations, CTB 87 and the blazar QSO J2015+371 are clearly visible, with the VERITAS emission centered on a location that lies within the radio shell of CTB 87, supporting the theory that the VHE γ -ray emission is from that source. In contrast, the lower-energy *Fermi*-LAT emission is located between the two sources and outside of any of the X-ray emission regions. *Chandra* observations of the region clearly show a bright point source (CXOU J201609.2+371110) that lies within the X-ray emission from CTB 87 at $(l, b) = (74.9438, +01.1140)$; though pulsations have yet to be detected, it has been suggested that this is the location of the pulsar powering the PWN. The implications of this, as well as the location and

morphology of the X-ray emission, are discussed in detail in Matheson et al. (2013), concluding that CTB 87 is an evolved (~ 5 – 28 kyr), crushed PWN with the extended radio emission and likely a “relic” PWN, as in Vela-X and G327.1–1.1, both of which are detected in VHE γ -rays. Saha (2016) conducted a multiwavelength study of the object, where they attributed excess emission in the MeV–GeV range to an additional Maxwellian component. In contrast, the single power-law fit presented here does not require this component. However, the emission above 1 TeV still requires the BPL electron distribution as presented in Figure 4 of that work. This BPL electron population can be understood in the context of the multiwavelength data with the electron distribution before the break responsible for the radio emission and the population after the break responsible for the X-ray emission. Due to the

relatively poor angular resolution of VERITAS in comparison to the radio and X-ray observations, it is not possible to observe any differences in the VHE spectrum from these two locations.

7. Source Population In Comparison to H.E.S.S. Galactic Plane Survey

It is interesting to compare the populations of HE and VHE sources in the Cygnus region to the region covered by the H.E.S.S. Galactic plane survey. In the region surveyed by H. E.S.S. ($250^\circ < l < 65^\circ$, $-3.5^\circ < b < 3.5^\circ$, 2700 hr of quality-selected data), they detected 78 sources (H.E.S.S. Collaboration et al. 2018a). The average sensitivity for their survey was approximately 1.5% Crab Nebula flux for point sources, though it varied across the region. In comparison, the average sensitivity in this work is about 3% of the Crab, two times higher, though again it shows significant variation with position. In the *Fermi*-LAT 3FGL catalog there are 339 total sources in the region covered by H.E.S.S. and 37 in the region covered by this work. We would therefore expect to detect $37/339 \times 78 = 8$ VHE sources in the VERITAS survey region, roughly twice the number that we detect (depending on whether VER J2018+367* and VER J2020+368* are considered as independent sources or as hot spots in VER J2019+368). Performing similar calculations with the 2FHL and 3FHL catalogs gives $3/40 \times 78 = 6$ and $13/119 \times 78 = 9$ VHE sources within the VERITAS region, respectively. All three predictions agree well with the number of sources observed given the difference in sensitivity between the two surveys and suggest that there is likely a correlation between the numbers of HE and VHE sources in a region. It should, however, be noted that this is a very simplistic calculation and does not take into account the distances to the sources, the possibility of source confusion, the differences in the diffuse Galactic background, or the relative depth of the surveys.

8. Conclusions

The results of the VERITAS survey of the Cygnus region covering a 15° by 5° area centered at $(l, b) = (74.5, 1.5)$ conducted between 2007 April and 2008 December with a total observing time of 135 hr (120 hr live time) were presented. We also included targeted and follow-up observations of 174 hr (151 hr live time) made by VERITAS between 2008 November and 2012 June, for a total observing time of about 309 hr (271 hr live time). A Pass 8 *Fermi*-LAT analysis of the same region using over 7 yr (2008 August–2016 January) of data above 1 GeV was also conducted.

No new sources were detected in the VERITAS analysis, and the updated results of the four previously detected VERITAS sources show the following:

VER J2019+407: The morphology of the HE γ -ray emission from 3FGL J2021.0+4031e is not a uniform disk as in the 3FGL and peaks at the northeastern rim of the SNR, in the same region as the VERITAS emission from VER J2019+407. A *Fermi*-LAT spectrum extracted from the region coincident with the region from which the VERITAS spectrum is extracted was found to agree well with the VERITAS data, and a joint fit is well

described by a broken power law showing a common origin.

VER J2031+415: An extended (68% containment radius = $0.15^{+0.02}_{-0.03}$) *Fermi*-LAT potential counterpart to VER J2031+415 (TeV J2032+4130) is detected at a test statistic of 321. The spectral points for VER J2031+415 and the *Fermi*-LAT counterpart are jointly fit by a single power law.

VER J2019+368: Two source candidates were identified in VER J2019+368, VER J2018+367* and VER J2020+368*. Both sources are detected at a level greater than $7\sigma_{\text{local}}$, and the spectra are fit with a single power law.

VER J2016+371: When the *Fermi*-LAT emission is fit as two point sources, one located at the radio location of CTB 87 and the other at the radio location of QSO J2015+371, a single power law fits the data from the CTB 87 located *Fermi*-LAT source and the emission detected by VERITAS.

In addition to the detected sources, VERITAS upper limits have been produced for 71 locations at an average level of 2.25% (2.87%) of the Crab Nebula flux for a 0.1° (0.23°) integration region. These locations have, on average, a positive significance of 0.33 (0.18), a 2.9σ (1.7σ) deviation from the expected average significance.

The Cygnus region has significant potential for follow-up observations by VERITAS (especially following the summer 2012 camera upgrade and the development of advanced analysis methods aimed at extended sources) and for future work with CTA (Dubus et al. 2013) and HAWC.

This research is supported by grants from the U.S. Department of Energy Office of Science, the U.S. National Science Foundation, and the Smithsonian Institution and by NSERC in Canada. We acknowledge the excellent work of the technical support staff at the Fred Lawrence Whipple Observatory and at the collaborating institutions in the construction and operation of the instrument. The VERITAS Collaboration is grateful to Trevor Weekes for his seminal contributions and leadership in the field of VHE γ -ray astrophysics, which made this study possible.

This research made use of NASA's Astrophysics Data System; data and/or software provided by the High Energy Astrophysics Science Archive Research Center (HEASARC), which is a service of the Astrophysics Science Division at NASA/GSFC and the High Energy Astrophysics Division of the Smithsonian Astrophysical Observatory; data from the Canadian Galactic Plane Survey, a Canadian project with international partners, supported by the Natural Sciences and Engineering Research Council; and the SIMBAD database, operated at CDS, Strasbourg, France. This research is based on observations obtained with *XMM-Newton*, an ESA science mission with instruments and contributions directly funded by ESA Member States and NASA and observations made with the *Spitzer Space Telescope*, which is operated by the Jet Propulsion Laboratory, California Institute of Technology, under a contract with NASA.

We wish to thank the anonymous referee for their constructive comments on this paper.

Facilities: VERITAS, *Fermi*.

Software: Astropy (Robitaille et al. 2013), Fermipy (Wood et al. 2017), matplotlib (Hunter 2007), SciPy (Jones et al. 2001), ROOT (Brun & Rademakers 1997).

Appendix A Calculation of VERITAS Spectral Errors

For the VERITAS spectra presented in this work, statistical errors on the spectra were computed and plotted to indicate the 1σ confidence range of the fitted models (a “butterfly” plot). For a power law with parameters $N_0 \pm \Delta N_0$, spectral index $-\gamma \pm \Delta\gamma$, and covariance $\text{cov}(N_0, \gamma)$, the contour is defined by

$$\frac{\Delta F^2}{F^2} = \left(\frac{\Delta N_0}{N_0} \right)^2 + \Delta\gamma^2 \ln^2 \left(\frac{E}{E_0} \right) - 2 \frac{\text{cov}(N_0, \gamma)}{N_0} \ln \left(\frac{E}{E_0} \right), \quad (5)$$

where the narrowest point in the butterfly occurs at the decorrelation energy (E_d)

$$E_d = E_0 \exp \left(\frac{\text{cov}(N_0, \gamma)}{(N_0 \Delta\gamma^2)} \right). \quad (6)$$

The normalization (N_0) is quoted at E_d to minimize the covariance between the errors.

The butterfly for the log parabola is defined by

$$\begin{aligned} \frac{\Delta F^2}{F^2} = & \left(\frac{\Delta N_0}{N_0} \right)^2 + \Delta\gamma^2 \ln^2 \left(\frac{E}{E_0} \right) + \Delta\beta^2 \ln^4 \left(\frac{E}{E_0} \right) \\ & - 2 \frac{\text{cov}(N_0, \gamma)}{N_0} \ln \left(\frac{E}{E_0} \right) \\ & - 2 \frac{\text{cov}(N_0, \beta)}{N_0} \ln^2 \left(\frac{E}{E_0} \right) \\ & + 2 \text{cov}(\gamma, \beta) \ln^3 \left(\frac{E}{E_0} \right). \end{aligned} \quad (7)$$

For LP spectral fits E_0 was fixed to E_d calculated in the PL fit (which was calculated prior to the LP fit).

When fitting the BPL, there was a large correlation between E_b and N_0 , which severely limited the quality of the fit, especially when $\delta\gamma (=|\gamma_1 - \gamma_2|)$ was small. To overcome this, a preliminary fit was conducted with E_b free (along with N_0 , γ_1 , and γ_2). E_b was then fixed to this value and the fit was conducted again, which results in a much better constrained fit. The butterfly is given by

$$\frac{\Delta F^2}{F^2} = \begin{cases} \left(\frac{\Delta N_0}{N_0} \right)^2 + \Delta\gamma_1^2 \ln^2 \left(\frac{E}{E_b} \right) - 2 \frac{\text{cov}(N_0, \gamma_1)}{N_0} \ln \left(\frac{E}{E_b} \right) & \text{if } E \leq E_b \\ \left(\frac{\Delta N_0}{N_0} \right)^2 + \Delta\gamma_2^2 \ln^2 \left(\frac{E}{E_b} \right) - 2 \frac{\text{cov}(N_0, \gamma_2)}{N_0} \ln \left(\frac{E}{E_b} \right) & \text{if } E > E_b. \end{cases} \quad (8)$$

For the ECPL the butterfly is given by

$$\begin{aligned} \frac{\Delta F^2}{F^2} = & \left(\frac{\Delta N_0}{N_0} \right)^2 + \Delta\gamma^2 \ln^2 \left(\frac{E}{E_0} \right) + \left(\frac{E \Delta E_c}{E_c^2} \right)^2 \\ & - 2 \frac{\text{cov}(N_0, \gamma)}{N_0} \ln \left(\frac{E}{E_0} \right) + 2 \frac{\text{cov}(N_0, E_c) E}{N_0 E_c^2} \\ & - 2 \frac{\text{cov}(\gamma, E_c) E}{E_c^2} \ln \left(\frac{E}{E_0} \right). \end{aligned} \quad (9)$$

As for the LP fit, an initial PL fit was conducted to determine E_0 .

Appendix B Trials Factor Estimation

A significant number of statistical trials (X_T) are associated with blind searches for γ -ray sources of unknown location in a survey such as this. These trials increase the chance of an observed positive significance at any location being the result of statistical fluctuations of the background and need to be accounted for when determining the significance of any observed deviation from the null hypothesis (no γ -ray sources in the region, assuming only a uniform cosmic-ray background). Since the grid points are correlated, in both the ON-region and the OFF-region, the number of trials will be less than the number of grid points. To estimate the number of trials in this analysis, Monte Carlo simulations were conducted to estimate the chance of measuring a given significance in the absence of a signal. Background-only sky maps were generated by throwing the expected number of background “events” with a probability distribution constructed from the acceptance map shown in Figure 1. An RBM analysis was then conducted for each simulated sky map, and the significance for each point was calculated. The significance of an a priori chosen random point (σ_{local}) and the maximum significance of any point (σ_{global}) were recorded. In total, about 1.5×10^6 simulated sky maps were produced.

The trials factor (X_T) was found by considering that searching the significance sky map for a signal constitutes a simple success/failure test at each location on the sky with a probability distribution described by the Binomial probability function. In this case, a “success” was classed as the measured signal being due to a random statistical fluctuation of the background. When dealing with the probability of observing more than n successes in N attempts, the binomial expression given above was summed and expanded:

$$P_{(n \geq 1)} = \sum_{n=1}^N \frac{N!}{n!(N-n)!} p^n (1-p)^{(N-n)} \quad (10)$$

$$= 1 - (1-p)^N. \quad (11)$$

Here $P_{(n \geq 1)}$ is the probability of observing one or more values with individual probabilities p . Hence, for larger and larger values of N (i.e., more trials), the likeliness of observing this success increases. This equation was then rearranged to get an expression for the X_T ($\equiv N$), which relates the local ($P_{\text{local}} \equiv p$), which was calculated using the distribution of σ_{local}) and global ($P_{\text{global}} \equiv P_{(n \geq 1)}$), which was calculated using the

distribution of σ_{global}) probabilities:

$$X_T = \frac{\ln(1 - P_{\text{global}})}{\ln(1 - P_{\text{local}})}. \quad (12)$$

Figure 21 shows the dependence of X_T on σ_{local} . X_T increases with increasing σ_{local} , but it is always significantly smaller than the number of bins in the sky map, reflecting the correlation in both the signal (due to the size of the ON-region relative to the grid spacing) and background (due to the size of the OFF-region). The *Extended* integration region has a smaller X_T than the *Point* integration region, reflecting the higher level of correlation between the ON-regions. Figure 22 shows how the global significance varies as a function of local significance. Below a σ_{local} of about 4.5 the σ_{global} is 0 since a fluctuation of this magnitude is expected in every observation. Achieving a σ_{global} that is greater than 5 requires a σ_{local} that is greater than 7.

ORCID iDs

T. Aune  <https://orcid.org/0000-0003-3998-0854>
W. Benbow  <https://orcid.org/0000-0003-2098-170X>
R. Bird  <https://orcid.org/0000-0002-4596-8563>
W. Cui  <https://orcid.org/0000-0002-6324-5772>
Q. Feng  <https://orcid.org/0000-0001-6674-4238>
J. P. Finley  <https://orcid.org/0000-0002-8925-1046>
A. Furniss  <https://orcid.org/0000-0003-1614-1273>
E. V. Gotthelf  <https://orcid.org/0000-0003-3847-3957>
D. Hanna  <https://orcid.org/0000-0002-8513-5603>
C. A. Johnson  <https://orcid.org/0000-0002-0641-7320>
P. Kaaret  <https://orcid.org/0000-0002-3638-0637>
D. Kieda  <https://orcid.org/0000-0003-4785-0101>
M. Krause  <https://orcid.org/0000-0001-7595-0914>
M. J. Lang  <https://orcid.org/0000-0003-4641-4201>
G. Maier  <https://orcid.org/0000-0001-9868-4700>
R. Mukherjee  <https://orcid.org/0000-0002-3223-0754>
A. N. Otte  <https://orcid.org/0000-0002-5955-6383>
D. Pandel  <https://orcid.org/0000-0003-2085-5586>
N. Park  <https://orcid.org/0000-0002-4282-736X>
M. Pohl  <https://orcid.org/0000-0001-7861-1707>
A. Popkow  <https://orcid.org/0000-0002-3157-8839>
E. Pueschel  <https://orcid.org/0000-0002-0529-1973>
G. T. Richards  <https://orcid.org/0000-0002-1408-807X>
K. Shahinyan  <https://orcid.org/0000-0001-5128-4160>
D. A. Williams  <https://orcid.org/0000-0003-2740-9714>

References

- Abdo, A., Ackermann, M., Ajello, M., et al. 2009, *Sci*, **326**, 1512
Abdo, A., Allen, B., Berley, D., et al. 2007, *ApJL*, **664**, L91
Abdo, A. A., Ackermann, M., Ajello, M., et al. 2009, *ApJS*, **183**, 46
Abdo, A. A., Ackermann, M., Ajello, M., et al. 2010a, *ApJS*, **188**, 405
Abdo, A. A., Ackermann, M., Ajello, M., et al. 2010b, *A&AS*, **187**, 460
Abdo, A. A., Ajello, M., Allafort, A., et al. 2013, *ApJS*, **208**, 17
Abdo, A. A., Allen, B. T., Aune, T., et al. 2012, *ApJ*, **753**, 159
Abeysekara, A. U., Albert, A., Alfaro, R., et al. 2017, *ApJ*, **843**, 40
Acero, F., Ackermann, M., Ajello, M., et al. 2015, *ApJS*, **218**, 41
Acero, F., Ackermann, M., Ajello, M., et al. 2016, *ApJS*, **224**, 8
Ackermann, M., Ajello, M., Allafort, A., et al. 2011, *Sci*, **334**, 1103
Ackermann, M., Ajello, M., Allafort, A., et al. 2013, *ApJS*, **209**, 34
Ackermann, M., Ajello, M., Atwood, W. B., et al. 2016, *ApJS*, **222**, 5
Aharonian, F., Akhperjanian, A., Beilicke, M., et al. 2002, *A&A*, **393**, L37
Aharonian, F., Akhperjanian, A., Beilicke, M., et al. 2004, *ApJ*, **614**, 897
Aharonian, F., Akhperjanian, A., Beilicke, M., et al. 2005, *A&A*, **431**, 197
Ahnen, M. L., Ansoldi, S., Antonelli, L. A., et al. 2017, *MNRAS*, **472**, 3474
Ajello, M., Atwood, W. B., Baldini, L., et al. 2017, *ApJS*, **232**, 18
Albert, J., Aliu, E., Anderhub, H., et al. 2007, *ApJL*, **665**, L51
Albert, J., Aliu, E., Anderhub, H., et al. 2008, *ApJL*, **675**, L25
Aleksić, J., Antonelli, L. A., Antoranz, P., et al. 2010, *ApJ*, **721**, 843
Aliu, E., Anderhub, H., Antonelli, L. A., et al. 2008, *ApJL*, **685**, L71
Aliu, E., Archambault, S., Arlen, T., et al. 2013, *ApJ*, **770**, 93
Aliu, E., Aune, T., Behera, B., et al. 2014a, *ApJ*, **783**, 16
Aliu, E., Aune, T., Behera, B., et al. 2014b, *ApJ*, **788**, 78
Allafort, A., Baldini, L., Ballet, J., et al. 2013, *ApJL*, **777**, L2
Archambault, S., Beilicke, M., Benbow, W., et al. 2013, *ApJ*, **779**, 150
Atwood, W., Albert, A., Baldini, L., et al. 2013, in *Proc. Fourth Int. Fermi Symp.* (arXiv:1303.3514)
Atwood, W. B., Abdo, A. A., Ackermann, M., et al. 2009, *ApJ*, **697**, 1071
Bartoli, B., Bernardini, P., Bi, X. J., et al. 2012, *ApJL*, **745**, L22
Benjamin, R. A., Churchwell, E., Babler, B. L., et al. 2003, *PASP*, **115**, 953
Berge, D., Funk, S., & Hinton, J. 2007, *A&A*, **466**, 1219
Brun, R., & Rademakers, F. 1997, *NIMPA*, **389**, 81
Butt, Y., Benaglia, P., Combi, J. A., et al. 2003, *ApJ*, **597**, 494
Butt, Y. M., Drake, J., Benaglia, P., et al. 2006, *ApJ*, **643**, 238
Camilo, F., Ray, P. S., Ransom, S. M., et al. 2009, *ApJ*, **705**, 1
Cardenzana, J. 2017, PhD thesis, Iowa State Univ., <https://lib.dr.iastate.edu/etd/15272>
Churchwell, E., Babler, B. L., Meade, M. R., et al. 2009, *PASP*, **121**, 213
Clark, C. J., Wu, J., Pletsch, H. J., et al. 2017, *ApJ*, **834**, 106
Corbel, S., Dubus, G., Tomsick, J. A., et al. 2012, *MNRAS*, **421**, 2947
Daniel, M. K. 2007, *Proc. ICRC*, **30**, 1325
De Becker, M., & Raucq, F. 2013, *A&A*, **558**, A28
Dubus, G., Contreras, J. L., & Funk, S. o. 2013, *Aph*, **43**, 317
Ferrand, G., & Safi-Harb, S. 2012, *AdSpR*, **49**, 1313
Fomin, V. P., et al. 1991, *Proc. ICRC*, **22**, 468
Fraija, N., & Araya, M. 2016, *ApJ*, **826**, 31
Gotthelf, E. V., Mori, K., Aliu, E., et al. 2016, *ApJ*, **826**, 25
Green, D. 2014, *A Catalogue of Galactic Supernova Remnants*, Cavendish Laboratory (Cambridge: Cambridge Univ. Press)
Green, D. A. 2014, *BASI*, **42**, 47
Guenette, R. 2009, arXiv:0908.0714
H.E.S.S. Collaboration, Abdalla, H., Abramowski, A., et al. 2018a, *A&A*, **612**, A1
H.E.S.S. Collaboration, Abdalla, H., Abramowski, A., et al. 2018b, *A&A*, **612**, A2
Hillas, A. M. 1985, *Proc. ICRC*, **19**, 445
Hobbs, G. B., Edwards, R. T., & Manchester, R. N. 2006, *MNRAS*, **369**, 655
Holder, J., Atkins, R. W., Badran, H. M., et al. 2006, *Aph*, **25**, 391
Holder, J. & the VERITAS Collaboration 2016, in *Proc. AIP Conf.* 1792, *High-Energy Gamma-Ray Astronomy*, ed. F. A. Aharonian, W. Hofmann, & F. M. Rieger (Melville, NY: AIP), 020013
Horns, D., Hoffmann, A. I. D., Santangelo, A., Aharonian, F. A., & Rowell, G. P. 2007, *A&A*, **469**, L17
Hou, C., Chen, S.-Z., Yuan, Q., et al. 2014, *ChPhC*, **38**, 085001
Hunter, J. D. 2007, *CSE*, **9**, 90
Jones, E., Oliphant, T., Peterson, P., et al. 2001, *SciPy: Open Source Scientific Tools for Python*, www.scipy.org
Kerr, M., Ray, P., Johnston, S., et al. 2015, *ApJ*, **814**, 128
Konopelko, A., Atkins, R. W., Blaylock, G., et al. 2007, *ApJ*, **658**, 1062
Lande, J., Ackermann, M., Allafort, A., et al. 2012, *ApJ*, **756**, 5
Leahy, D. A., Green, K., & Ranasinghe, S. 2013, *MNRAS*, **436**, 968
Li, T.-P., & Ma, Y.-Q. 1983, *ApJ*, **272**, 317
Liu, Q. Z., van Paradijs, J., & van den Heuvel, E. P. J. 2006, *A&A*, **455**, 1165
Liu, Q. Z., van Paradijs, J., & van den Heuvel, E. P. J. 2007, *A&A*, **469**, 807
Lozinskaya, T. A., Pravdikova, V. V., & Finoguenov, A. 2002, *AstL*, **28**, 223
Lyne, A., Stappers, B., Keith, M., et al. 2015, *MNRAS*, **451**, 581
Malyshev, D., Zdziarski, A. A., & Chernyakova, M. 2013, *MNRAS*, **434**, 2380
Manchester, R. N., Hobbs, G. B., Teoh, A., & Hobbs, M. 2005, *AJ*, **129**, 1993
Matheson, H., Safi-Harb, S., & Kothes, R. 2013, *ApJ*, **774**, 33
Mizuno, T., Tanaka, N., Takahashi, H., et al. 2017, *ApJ*, **841**, 104
Murakami, H., Kitamoto, S., Kawachi, A., & Nakamori, T. 2011, *PASJ*, **63**, S873
Otte, A. N. 2009, *Proc. ICRC*, **31**, 1408
Paredes, J. M., Marti, J., Chandra, C. H. I., & Bosch-Ramon, V. 2007, *ApJL*, **654**, L135
Park, N. 2015, *Proc. ICRC*, **34**, 771
Piano, G., Tavani, M., Vittorini, V., et al. 2012, *A&A*, **545**, A110
Pletsch, H., & Clark, C. 2014, *Einstein@Home Gamma-ray Pulsar Discoveries in Fermi-LAT Data*, https://einsteinathome.org/gammaraypulsar/FGRPI_discoveries.html
Ray, P. S., Kerr, M., Parent, D., et al. 2011, *ApJS*, **194**, 17
Reid, M. J., McClintock, J. E., Narayan, R., et al. 2011, *ApJ*, **742**, 83

- Reipurth, B., & Schneider, N. 2008, in *Handbook of Star-forming Regions* 4, ed. B. Reipurth (San Francisco, CA: ASP), [36](#)
- Rieke, G., Young, E. T., Engelbracht, C. W., et al. 2004, [ApJS](#), **154**, 25
- Robitaille, T. P., Tollerud, E. J., Greenfield, P., et al. 2013, [A&A](#), **558**, [A33](#)
- Rolke, W. A., López, A. M., & Conrad, J. 2005, [NIMPA](#), **551**, 493
- Saha, L. 2016, [MNRAS](#), **460**, [3563](#)
- Sguera, V. 2009, [arXiv:0902.0245](#)
- Shaw, M. S., Romani, R. W., Cotter, G., et al. 2013, [ApJ](#), **764**, [135](#)
- Tavani, M., Bulgarelli, A., Piano, G., et al. 2009, [Natur](#), **462**, 620
- Taylor, A. R., Gibson, S. J., Peracaula, M., et al. 2003, [AJ](#), **125**, [3145](#)
- Thompson, D. J., Bertsch, D. L., Dingus, B. L., et al. 1995, [ApJS](#), **101**, [259](#)
- Uchiyama, H., Matsumoto, H., Tsuru, T. G., et al. 2009, [PASJ](#), **61**, [S189](#)
- van Kerkwijk, M. H., Charles, P. A., Geballe, T. R., et al. 1992, [Natur](#), **355**, [703](#)
- VERITAS & MAGIC Collaborations 2017, *ATel*, [10810](#)
- Verschuur, G., & Kellermann, K. (ed.) 1988, *Galactic and Extragalactic Radio Astronomy* (1st ed.; New York: Springer)
- Weinstein, A. 2014, [NuPhS](#), **256**, [136](#)
- Weinstein, A., et al. 2009, [arXiv:0912.4492](#)
- Wood, M., Caputo, R., Charles, E., et al. 2017, *Proc. ICRC*, **35**, 824
- Xiang, J., Lee, J. C., Nowak, M. A., & Wilms, J. 2011, [ApJ](#), **738**, [78](#)
- Zanin, R., Fernández-Barral, A., de Oña Wilhelmi, E., et al. 2016, [A&A](#), **596**, [55](#)
- Zdziarski, A. A., Malyshev, D., Chernyakova, M., & Pooley, G. G. 2017, [MNRAS](#), **471**, [3657](#)
- Zdziarski, A. A., Malyshev, D., de Oña Wilhelmi, E., et al. 2016, [MNRAS](#), **455**, [1451](#)